Effective quantum spin models for graphene nanoribbons

Von der Fakultät für Mathematik, Informatik und Naturwissenschaften der RWTH Aachen University zur Erlangung des akademischen Grades einer Doktorin der Naturwissenschaften genehmigte Dissertation

vorgelegt von

M.Sc. Anne Cornelie Gergs, geb. Koop

aus Oldenburg i.O.

Berichter: Universitätsprofessor Stefan Weßel Ph.D.

Universitätsprofessor Dr. rer. nat. Riccardo Mazzarello

Tag der mündlichen Prüfung: 12. April 2018

Diese Dissertation ist auf den Internetseiten der Universitätsbibliothek verfügbar.

List of Publications

A large part of this thesis has been published in the following two journal articles:

- Parts of Section 2 are published in
  Cornelie Koop and Manuel J. Schmidt, "Effective spin theories for edge magnetism in graphene zigzag ribbons", Physical Review B **92**, 125416 (2015)
- Parts of Section 3 are presented in
  Cornelie Koop and Stefan Wessel, "Quantum phase transitions in effective spin-ladder models for graphene zigzag nanoribbons", Physical Review B **96**, 165114 (2017)

The calculations in Section 2 extend the ones done in the author's Master's thesis: "Correlations at graphene edges", RWTH Aachen University 2012

The author has also contributed to the following publication, which is not part of the thesis:

- Xiao-Dong Tan, Cornelie Koop, Xiao-Ping Liao, and Litao Sun: "Quantum correlations in chiral graphene nanoribbons", Journal of Physics: Condensed Matter **28**, 435601 (2016)

Abstract/ Zusammenfassung

Since its first controlled fabrication in the laboratory in 2004, graphene has been raising much interest in the solid state physics community and high hopes for industrial applications. The two-dimensional layer of carbon atoms features a high electron mobility, a low spin-orbit interaction, and a relativistic electron dispersion relation near the Fermi surface. The zigzag edges of finite graphene sheets host special localized electronic states, which leads to a locally enhanced density of states near the edge, where interaction effects become important. In particular, the edge electrons interact magnetically via their spin. These rather stable magnetic moments might be a basis for future spintronics applications. A particularly useful shape for the analysis of edge magnetism are zigzag graphene nanoribbons (ZGNRs), i.e. few nanometer wide stripes of graphene which can be arbitrarily long in the lateral direction. Pure zigzag nanoribbons have two extended zigzag edges, which—due to the bipartite nature of the honeycomb lattice structure—have their outermost sites at different sublattices. Mean-field calculations regarding the Hubbard model on a honeycomb lattice as well as ab-initio studies have found before a ferromagnetic coupling between electrons on the same side and sublattice and an antiferromagnetic interaction between opposite sides.

In the first part of this work, we investigate the interactions of the edge magnetic moments within an effective model for the Hubbard model on the honeycomb lattice, taking into account quantum fluctuations, which are beyond mean-field approximation. For this purpose, the interaction with the bulk states of graphene is regarded as a perturbation to the edge-edge interactions, using as a small parameter the ratio between the overlap of edge and bulk states and the overlap of edge states with themselves. We treat the interactions up to second order perturbation theory by means of a Schrieffer-Wolff transformation. Already in first order, this gives a good approximation of the coupling strengths, and second order terms are only needed if in wide graphene nanoribbons a high accuracy is requested. In first order, the intraedge interactions are essentially long-ranged and behave as $\propto 1/r^2$ with distance along the ribbon, while the interedge couplings decline as $\propto 1/r^4$. Some of the second order contributions act analogous to an RKKY interaction, an effect which generally describes the interaction between magnetic impurities via conduction electrons.

In the second part of the thesis, these results are generalized to more abstract spin ladder models and their thermodynamic limit behavior is analyzed. For this, a quantum Monte Carlo code based on the stochastic series expansion is used. We set up two models: The first one uses the original short-range coupling strengths and a long-range tail that declines with power-law, while the second model effectively consists of two Haldane-Shastry chains that are coupled with an antiferromagnetic rung interaction. Both models are scalable, and for both we find two different phases in the thermodynamic limit extrapolation: For realistic coupling strengths in wide nanoribbons, there is a weak ferromagnetic order for $T = 0$, and the system is gapless. In contrast to this, for artificially enhanced rung couplings, the system is in a quantum disordered spin-singlet state with a spin excitation gap. There is indication that this is also the ground state of realistic, very narrow ZGNRs. With finite-size scaling we analyze the quantum phase transition, determine the scaling exponents and compare them to known field theoretical findings.

Seitdem es 2004 erstmalig im Labor kontrolliert hergestellt wurde, hat Graphen viel Interesse in der Festkörperphysik und große Hoffnungen auf industrielle Anwendungen geweckt. Die zweidimensionale Schicht von Kohlenstoffatomen weist eine hohe Elektronen-Mobilität auf, eine niedrige Spin-Bahn Wechselwirkung und eine relativistische Dispersionsrelation der Elektronen nahe der Fermi-Oberfläche. Zickzackränder von endlichen Graphenschichten beherbergen spezielle lokalisierte elektronische Zustände, was zu einer lokal erhöhten Zustandsdichte nahe des Randes führt, wo dann Wechselwirkungseffekte wichtig werden. Insbesondere wechselwirken die Randelektronenspins miteinander. Diese relativ stabilen magnetischen Momente könnten eine Basis für zukünftige Spintronik-Anwendungen sein. Eine besonders nützliche Form für die Analyse von Randmagnetismus sind Zickzackgraphennanobänder, d.h. wenige Nanometer breite Streifen von Graphen, die in seitliche Richtung beliebig lang sein können. Reine Zickzacknanobänder haben zwei ausgedehnte Zickzackränder, welche — aufgrund der zweiteiligen Natur der Honigwabengitters— ihre äußersten Plätze auf verschiedenen Subgittern haben. Molekularfeldtheorie Rechnungen, die das Hubbard-Modell auf dem Honigwabengitter betrachten, ebenso wie ab-initio Studien haben zuvor eine ferromagnetische Kopplung zwischen Elektronen vom selben Rand und Untergitter sowie eine antiferromagnetische Wechselwirkung zwischen gegenüberliegenden Rändern gefunden.

Im ersten Teil dieser Arbeit untersuchen wir die Wechselwirkungen der magnetischen Momente am Rand innerhalb eines effektiven Modells für das Hubbard-Modell auf dem Honigwabengitter, wobei wir Quantenfluktuationen berücksichtigen, die jenseits von Molekularfeldnäherungen liegen. Dafür wird die Wechselwirkung mit den "Bulk"-Zuständen als eine Störung der Rand-Rand-Wechselwirkung betrachtet, wobei als kleiner Parameter das Verhältnis zwischen dem Überlapp von Rand und "Bulk"-Zuständen und dem Überlapp von Randzuständen mit sich selbst benutzt wird. Wir behandeln die Wechselwirkungen bis in zweite Ordnung Störungstheorie mithilfe einer Schrieffer-Wolff-Transformation. Bereits in erster Ordnung ergibt sich eine gute Näherung der Kopplungsstärken, und Terme zweiter Ordnung werden nur gebraucht, wenn in breiten Graphennanobändern eine hohe Genauigkeit erforderlich ist. In erster Ordnung sind die Wechselwirkungen innerhalb eines Randes im Wesentlichen langreichweitig und verhalten sich wie $\propto 1/r^2$ mit dem Abstand entlang des Bandes, während die Kopplungen zum gegenüberliegenden Rand wie $\propto 1/r^4$ abfallen. Einige der Beiträge zweiter Ordnung verhalten sich analog zur RKKY-Wechselwirkung, einem Effekt, der allgemein die Wechselwirkung zwischen magnetischen Verunreinigungen über Leitungselektronen beschriebt.

Im zweiten Teil der Arbeit werden diese Ergebnisse verallgemeinert auf abstraktere Spinleitermodelle und deren Verhalten im thermodynamischen Limes wird analysiert. Dafür wird ein Quanten-Monte-Carlo-Verfahren benutzt, das auf einer stochastischen Reihenentwicklung ("stochastic series expansion") basiert. Wir setzen zwei Modelle ein: Das erste benutzt die ursprünglichen kurzreichweitigen Kopplungsstärken und einen langreichweitigen Anteil, der entsprechend einer Potenz abfällt, während das zweite Modell im Wesentlichen aus zwei Haldane-Shastry Ketten besteht, die mit einer antiferromagnetischen Sprossen-Wechselwirkung gekoppelt sind. Beide Modelle sind skalierbar, und für beide finden wir zwei verschiedene Phasen im extrapolierten thermodynamischen Limes: Für realistische Kopplungsstärken bei breiten Bändern gibt es eine schwache ferromagnetische Ordnung bei T=0, und das System hat keine Anregungslücke. Im Gegensatz dazu ist für künstlich erhöhte Sprossenkopplungen das System in einem quantenmechanisch ungeordneten Spin-Singulett-Zustand mit Spinanregungslücke. Es gibt Hinweise, dass dies auch der Grundzustand realistischer, sehr schmaler Zickzacknanobänder ist. Durch Untersuchen des Skalierungsverhaltens analysieren wir den Quantenphasenübergang, bestimmten die Skalierungsexponenten und vergleichen sie mit bekannten feldtheoretischen Resultaten.

Inhaltsverzeichnis

1. Introduction

Graphene is a two-dimensional layer of carbon atoms, which was one of the first two-dimensional materials ever to be synthesized in the laboratory[1, 2]. Even before its actual experimental realization, it was clear that it features many outstanding properties, with respect to mechanical aspects as well as concerning its electro-magnetic behavior. Theoretical works about this material date back to as early as 1947[3], and a larger number of studies has been made in the 80s and 90s (e.g. Refs. [4–8]), but it had remained unclear if it can be produced in reality[9], when graphene was finally synthesized in the laboratory by Novoselov, Geim et al. (Ref. [1, 2]) in 2004, using the famous Scotch tape method. This actual discovery lead to the Nobel Prize in 2010 and caused great interest and hopes among physicists, material scientists, and industry (e.g. Ref. [10]). What followed were intensive research in many related areas and an avalanche of publications on the topic. It was found for example that once formed, graphene layers feature an extremely high mechanical stability against bending and external pressure. On the electronic side, the interdiction of electronic backscattering[9] allows charge carriers to go for long distances without scattering and leads to a very high electronic conductance. The quantum Hall effect—where an electric current in a perpendicular magnetic field causes a voltage orthogonal to both, which grows in steps when the magnetic field is increased linearly—can be observed at room temperature[10]in graphene. Additionally, graphene features Klein tunneling, where electrons can surpass classically forbidden areas[9].

The material is basically a single slice of the much longer known graphite, which is found in everyday life as the inner part of a pencil, and it consists purely of carbon atoms, connected by sp^2 hybridized σ-bonds of the outer carbon electrons. They are arranged in a honeycomb lattice structure, and each carbon atom has one free p_z orbital perpendicular to the extension of the graphene sheet and filled with one electron at charge neutrality. In graphite, the different layers are helt together by relatively weak van-der-Waals forces. In single layer graphene p_z orbitals form the π bands that lie at energies near the Fermi surface, compare e.g. Ref. [9]. The lattice is bipartite, which means that it consists of two sublattices with each atom of type A directly connected only to atoms of type B.

The electronic properties of graphene can be well described by a tight-binding model on the honeycomb lattice. A very common approximation is to assume that the Coulonb interaction is screened and to apply the usual Hubbard model with only nearest-neighbor hopping t and onsite repulsion U, for example in Refs. [6, 11–13] . Another possible approach is to take into consideration next-nearest neighbor hopping t'. For $U = 0$ and $t' \neq 0$ one gets the dispersion relation[9]

$$\varepsilon = \pm t\sqrt{3 + f\left(\vec{k}\right)} - t' f\left(\vec{k}\right) \qquad \text{with } f\left(\vec{k}\right) = 2\cos\left(\sqrt{3}k_y a\right) + 4\cos\left(\frac{\sqrt{3}}{2}k_y a\right)\cos\left(\frac{3}{2}k_x a\right) \ ,$$

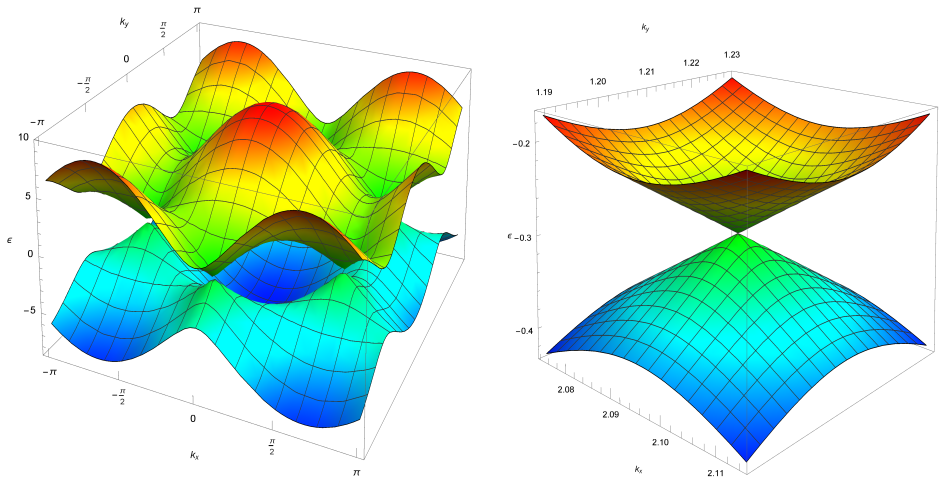

Figure 1.1.: The bandstructure of free bulk graphene, showing only the two π bands for $t' = 0.1t$ and $U = 0$, with $a = 1$. The right hand side shows a zoom to the region near one of the Dirac points.

where a is the lattice spacing. For actual graphene $a \approx 1.42$Å. Realistic values for the coupling constants are much harder to determine; ab initio calculations find $t \approx 2.8$eV and $t' \in [\sim 0.02t, \sim 0.2t]$ (Ref [9]). As shown in Fig. 1.1 for the non-interacting model with weak next nearest-neighbor hopping $t' = 0.1t$, the π bands exhibit a vanishing density of states at the Fermi surface and follow a nearly linear dispersion relation near $\varepsilon = -3t'$. These are the so called Dirac points located at

$$\vec{K} = \left(\frac{2\pi}{3a}, \frac{2\pi}{3\sqrt{3}a}\right), \qquad \vec{K}' = \left(\frac{2\pi}{3a}, -\frac{2\pi}{3\sqrt{3}a}\right).$$

This nearly linear dispersion relation near the Fermi surface is a key feature of graphene and leads to a quasi-relativistic behavior of the electrons[9]as a function of the momentum $\vec{q}$ relative to the Dirac points:

$$\varepsilon(\vec{q}) = v_F |\vec{q}| + \mathcal{O}\left(\left(\frac{q}{k}\right)^2\right)$$

with a Fermi velocity of roughly $v_F \approx c/300$. This dispersion relation is fundamentally different from usual semiconductors and makes the electrons effectively massless. Furthermore, due to the existence of two different such Dirac cones, a free electron in graphene can be attributed an additional degree of freedom, the so-called "valley-spin".

These peculiarities are associated with several special features of electrons in graphene. However, also more than ten years after its first experimental realization, there is still a long way to go for many of the actual large-scale applications. It remains challenging to produce pristine and defect-free graphene sheets on a large industrial scale. Many of the effects of freestanding bulk graphene are moreover altered as soon as the sheet is deposited on a substrate that is made up of another material.

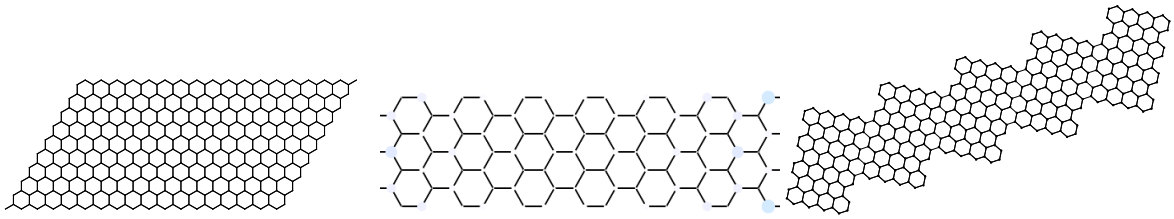

Figure 1.2.: The sketches show possible edge shapes for graphene: The left flake has zigzag edges on all sides (left), while the flake in the middle has extended armchair edges on the top and bottom edge (The figure for armchair edges was taken from Ref. [19]). The right ribbon features chiral edges in the extended direction: zigzag sections interrupted by armchair steps.

Despite the arising difficulties and the fact that it might after all not be the "wonder material" it has been called in the beginning, also a more realistic look at graphene still shows many promising possible applications, and it is for certain worthwhile to follow investigations in these directions. One of them are the magnetic properties of graphene. An area which has already long been believed to profit especially from the magnetism in graphene is the spintronics research, compare e.g. Refs. [14–16]. The basic definition of this technique is that in addition to the electronic degree of freedom used in conventional electronic devices, the spin degree of freedom will be used as a further variable.

Spintronics might yield a valuable contribution also to the development of a quantum computer, which has been one of the most promising, but also challenging fields of research in solid state physics in the last decade. It has been a great challenge to realize a quantum computer in the laboratory which features both sufficiently stable qubits that can be easily accessed and manipulated and also a scalability which allows for the combination of large enough numbers of qubits. On a basic level, the electron spin could serve as one realization of a qubit. The electron can be transported along a usual wire, and spin-entangled electrons could also be utilized for quantum communication, compare Ref. [17]. Graphene in general and its localized edge electrons in particular could constitute one possible candidate for the realization of the aforementioned stable qubit states. Graphene is an advantageous material, e.g. because it has long spin-diffusion lengths at room temperature (Ref. [16]) and it is possible to design various shapes and sizes on the nanoscale experimentally[16]. Freestanding graphene has an extremely low intrinsic spin-orbit coupling of only $\sim 10^{-5}$eV (compare Ref. [9]). On the one hand, this makes it difficult to realize certain related effects, such as the quantum spin Hall effect (QSHE) in freestanding samples. On the other hand, this can contribute to long spin coherence times[15], since one possible source of spin relaxation is nearly missing. This may make graphene a good candidate for spin based storage devices[18]. In addition to this, the nearly missing hyperfine interaction of the carbon cores is considered advantageous.

Defect-free bulk graphene is a non-magnetic semiconductor, but magnetic moments, which constitute the basis of many spintronic applications, are predicted to form at vacancy defects as well as in the vicinity of adatoms. Probably the most intrinsic and natural source of magnetism in graphene are its zigzag edges. If the edge is smooth and parallel to one of the lattice vec-

tors in graphene, then there are two types of possible edge shapes, namely zigzag and armchair edges, compare Fig. 1.2 (left and middle). It has been discovered theoretically already in the 1990s—compare Refs. [6, 7]—that the zigzag edges host special edge states, whose wave functions are localized near the zigzag edges, which in the bandstructure leads to a flat band near the Fermi surface. Plain armchair edges do not lead to localized electrons. In zigzag ribbons, the high density of states near the Fermi surface promotes a magnetic instability, which is described for the Hubbard model by the Stoner criterion.One can observe magnetic effects very well in thin stripes of graphene, denoted as graphene nanoribbons (GNRs): If the ribbons are terminated by zigzag edges, magnetic correlations between the edge states become an important effect[7, 8]. Following the Mermin-Wagner theorem[20], genuine magnetic long-range order in one-dimensional systems is prohibited—nevertheless in finite graphene samples significantly long spin correlation lengths are believed to be achievable. In order to be a useful material for spintronics, of course it has to fulfill several more prerequisites: One of them is the possibility to generate tunable magnetic moments that could be influenced by gating or doping[15]. Ref. [13], using first-principles calculations, demonstrates that by applying an external electric field to zigzag GNRs, the energy gap for one spin direction can be narrowed and closed, while it is increased for the other spin direction. The critical external field strength for half-metallicity decreases with increasing ribbon width. Using this setup it would be possible to generate an electric current that consists only of a definite spin direction. Also using first-principles calculations, the authors of Ref. [21] present a possible spin switch for such channels along the edges of two narrow GNRs, namely tetragonally shaped graphene islands between these GNRs. The edge magnetism in zigzag GNRs may also be used to selectively inject one spin direction into a larger sheet of graphene (Ref. [22]).

It has furthermore been demonstrated that the edge states in chiral GNRs show no entanglement along the ribbons direction, but a strong entanglement across the ribbon. The latter is even expected to be robust up to room temperature if the Coulomb interaction is weak enough, compare Ref. [23]. Such effects could be highly useful in quantum information technology

The determination of edge magnetism in experiment remains challenging, and the findings naturally depend on the substrate that is used. There have been several promising approaches in the recent years: Ref. [11] examines GNRs with different chiralities, which have been obtained from unzipping graphene nanotubes and depositing them on a gold substrate at cold temperatures. The local density of states is accessed via scanning tunneling spectroscopy (STS), and indication for double-peak structure near the edges is found, yielding an estimate for an excitation gap Δ as the distance between the two peaks. A setup at room temperature is presented in Ref. [24], where GNRs are fabricated by a scanning tunneling microscopy (STM) nanolithographic technique, also on a gold substrate. For zigzag GNRs at these temperatures, the authors predict a transition between two states depending on the ribbon width: For nanoribbons, an antiferromagnetic coupling between opposite edges is expected, while for broader ribbons, a ferromagnetic configuration is predicted. STM measurements of the bandgap as a function of ribbons width give a sudden drop and therewith support this assumption. Both previously mentioned experiments hence rely on charge based measurements and do not access the spin directly. A rather different approach, examining the interface between graphene and fluorine nanoridges, is taken in Ref. [25]. The system used is a multilayer of graphene with intermediate flourene chains, so that these chains separate the material into nanosegments of pure graphene with $C-sp^2/C-sp^3$

interfaces at the borders. The resulting effective graphene stripes are modeled as spin ladder with two collective spins on each rung and checked with Density Functional Theory (DFT) calculations; the results for the magnetic susceptibility χ are compared to measurements at various temperatures, which yields a good accordance. The authors draw the conclusion that their model GNRs have an increased Coulomb interaction, and long range magnetic order is suppressed by the effective one-dimensionality of the system. Finally, in Ref. [26] atomically precise zigzag GNRs with hybridized edges are produced by a bottom-up approach of "surface-assisted polymerization and subsequent cyclization of suitably designed molecular precursors" [26] and deposited on insulating NaCl islands on a gold surface. Their conductance is then accessed by an STM measurement and exhibits a peak structure in accordance with both DFT and *GW* calculations on the corresponding zigzag GNR models. This peak structure is a sign of a spin gap related to the assumed magnetic edge states. After all, however, a fully conclusive experimental proof is still not unanimously agreed upon.

In contrast to this, on the theoretical side there is more evidence, and several publications (for example Refs. [6, 8]) reveal to first order a ferromagnetic correlation between states on the same edge and an antiferromagnetic coupling between states on opposite edges, whose outermost sites are naturally located on opposite sublattices. In addition to this, edge states also occur in corrugated surfaces that include at least partially zigzag-type edges as well as in chiral edges, i.e., edges not parallel to one of the lattice vectors and consisting of alternating zigzag and armchair portions, as displayed in Fig. 1.2, right. The plain zigzag graphene nanoribbons have often successfully been regarded by means of ab-initio methods (Refs. [13, 14, 27]) as well as mean-field approximation (Refs. [6, 8]), both of which find the same qualitative first order results as stated above. It is however desirable to investigate the magnetic effects in GNRs with a method that takes also quantum fluctuations into account. For practical applications with GNRs deposited on a substrate, ab-initio methods can yield precise results for larger systems where e.g. spin-orbit coupling plays an important role in stabilizing the edge magnetism, compare Ref. [28]: If a GNR is deposited on the topological insulator Sb_2Te_3, it causes a twisting of the edge states due to the high spin-orbit coupling of the insulator's surface states. Another important substrate material is hexagonal Boron Nitride, which is also a honeycomb- shaped two dimensional material. It is an insulator and is currently believed to be a promising substrate for the deposition of graphene, also with respect to the visibility of edge states[29].

The goal of this work is to further analyze the edge magnetism in freestanding zigzag GNRs beyond mean-field approximation. The starting point of all calculations is the effective model for graphene in the Hubbard model, which drastically reduces the numerical effort by separating the edge and bulk degrees of freedom and treating the latter ones with a perturbative approach, where the overlap between edge and bulk states serves as the small parameter. Within this model, the magnetic interactions on the honeycomb lattice are reduced to an effective spin model, also taking into account quantum fluctuations. The model was previously developed and published in Refs. [30–32], but until now it had not been applied to extended plain zigzag ribbons. Instead, it was used to analyze the border between graphene and graphane[30], where the second one is a two-dimensional carbon sheet with honeycomb structure, but in contrast to graphene, half of the carbon atom feature a hybridization and the carbon bonds are of the sp^3 type. In a preceding work, the effective model was used to analyze chiral ribbons[31]. The latter exhibit alternating

zigzag and armchair edge segments, so that each zigzag part hosts exactly one localized edge electron, a special geometry that reduces perturbations deviating from the effective spin model. In the first part of this thesis, we broaden the usage of the effective model to the most natural case of extended zigzag edges. In the same step, we further refine the application by taking into account also interactions in the second order of the edge-bulk overlap, and we investigate to what extend the second-order terms are necessary in our geometry. In the second part of the present work, we study the finite temperature magnetic behavior of the effective spin models derived before, using the numerical quantum Monte Carlo approach. Graphene edge magnetism has been analyzed on the lattice basis by this technique before, yielding promising results[12]. But due to the large number of sites considered, only rather small system sizes were available. We can already regard significantly larger systems from the direct results of the effective model, and will further introduce scalability by going over to two more abstract ladder models. The finite temperature magnetic properties of these ladder models is then further analyzed, in a parameter regime close to the GNRs, as well as for artificially enhanced scaling parameters. Like this, we can make predictions about the behavior of zigzag GNRs with a width of $W \geq 6$ at small, but finite temperatures, as well as about the scaling properties of special spin ladders with long-range interactions.

The thesis is in detail structured as follows: In Chapter 2 we analyze the edge magnetism in plain zigzag graphene nanoribbons by means of an effective model that separates edge and bulk degrees of freedom in the Hubbard model on the honeycomb lattice. We first briefly introduce said effective model, which has been previously known[30–32], as well as its application to plain zigzag GNRs and the resulting first order spin couplings (Sec.2.1). We can confirm the expected ferromagnetic coupling along and antiferromagnetic coupling across the edges. Then we expand these calculations to second order using a Schrieffer-Wolff transformation, Sec.2.2, which at first yields an effective fermionic description of the edge state interactions. We describe in detail how the expressions can be transferred to momentum space and a quantitative calculation made possible. The rather abstract result is transferred to a spin basis afterwards (Sec.2.3) and we analyze to what extent the results from first order are altered by these corrections. We will find that in many cases already the first order results are sufficiently precise. To round up the picture, we then check—compare Sec.2.4—how the first-order findings change if next-nearest neighbor hopping t' on the honeycomb lattice is included into the effective model. We find the results to be rather robust as long as the magnitude of t' remains realistically small and half-filling of the lattice is maintained. Finally, we take a brief look at the related two-dimensional material phosphorene, which consists of a honeycomb structure of black phosphorus, but in contrast to graphene has a puckered structure and therefore highly different hopping amplitudes towards the neighboring sites. The band structure of phosphorene is already quite different, and we find that as a result the ferromagnetic couplings are quantitatively enhanced, while the antiferromagnetic ones are severely suppressed as compared to graphene. However, the overall long-distance behavior is not altered.

In Chapter 3 we analyze the finite-temperature behavior of the edge magnetism in zigzag GNRs, derive a more generic spin ladder model for this and extrapolate its properties in the thermodynamic limit. To do so, the first-order results from Chapter 2 are plugged into finite temperature quantum Monte Carlo calculations, based on the stochastic series expansion method[33, 34]. We

begin the chapter (Sec.3.1) by an explanation of the numerical method, including the update and measurement procedures, and a brief comparison to known results for the typical Heisenberg ladder model. In the next Section 3.3, it is explained how we transfer the outcomes from the effective model to two different spin ladder models, one of them more closely reflecting the actual zigzag GNRs, the other one more general and abstract. Both incorporate a long-range ferromagnetic interaction along the legs and an antiferromagnetic inter-leg interaction. The more general model can also be understood as two ferromagnetic Haldane-Shastry chains[35–37] with additional antiferromagnetic rung couplings. We show a brief comparison to exact diagonalization results, confirming the accuracy of the numerics. In the following, we then present the numerical results first for the more detailed (Sec.3.4) and then for the more generic model (Sec.3.5), both with coupling values realistic for medium width GNRs as well as with artificially enhanced antiferromagnetic coupling values. We obtain mostly quantitative differences between the two models, and find for both of them a quantum phase transition driven by an overall artificial prefactor for the rung couplings. Broad ribbons with weak rung couplings in the thermodynamic limit exhibit a weak ferromagnetic order along the legs for $T = 0$, whereas for artificially large antiferromagnetic interactions, the ribbons are tuned into a gapped rung singlet phase. In Sec.3.6, for the more generic model we then scrutinize this phase transition using finite-size scaling to deduce the critical exponents from finite-temperature numerical data. An estimate for the gap size as a function of the scaling parameter is also obtained. The chapter closes by a short analytical consideration (Sec.3.7), as we perform conventional perturbation theory for the case of weak leg coupling, with the rung singlet state as unperturbed starting point.

We finish with a conclusion (Sec.4) where the results are summed up and related to each other, and a brief outlook is given what might be interesting for future analysis.

2. Second-order edge interactions from the effective model

The results presented in this chapter were partially published in the Ref. [38]: Cornelie Koop and Manuel J. Schmidt, Phys. Rev. B **92**, 125416 (2015) [a]. Some figures, notation and formulations from there have been used. Moreover, these results are based on and extend calculations done in the Master's Thesis Ref.[39].

2.1. Conventional edge state theory

2.1.1. The effective model

We start from the Hubbard model on the honeycomb lattice

$$H = H_0 + H_u = -t \sum_{\langle i,j\rangle\sigma} c^\dagger_{i\sigma} c_{j\sigma} + U \sum_i : \hat{n}_{i\uparrow} :: \hat{n}_{i\downarrow} : \tag{2.1}$$

with the usual operators $c^{(\dagger)}_{i\sigma}$, which annihilate (create) a particle with spin σ at site i and the normal ordering $: \hat{A} := \hat{A} - \langle A \rangle_0$ that is defined as the original operator minus the average in the non-interacting ground state. For the particle counting operators at half filling this means $: \hat{n}_{i\sigma} := \hat{n}_{i\sigma} - \frac{1}{2}$.

The precise model here is a pure zigzag graphene nanoribbon (GNR) with periodic boundary conditions (PBCs) as depicted in Fig. 2.1 (left side). When the site numbering is chosen as in the same figure on the right side, then the nearest-neighbor index $\langle i, j\rangle$ in Eq. (2.1) can be rendered more precisely, and the free hopping Hamiltonian becomes

$$H_0 = -t \sum_{n=1}^{N} \sum_{m=1}^{M} \sum_{\sigma} c^\dagger_{nmA\sigma} \left(c_{nmB\sigma} + c_{n(m-1)B\sigma} + c_{(n+1)(m-1)B\sigma} \right) + \text{h.c.}$$

[a] For this publication, C. Koop did the calculations and figures. Both authors worked together in the analysis of the results. M. J. Schmidt wrote the abstract and introduction, while both authors contributed equally to the rest of the text.

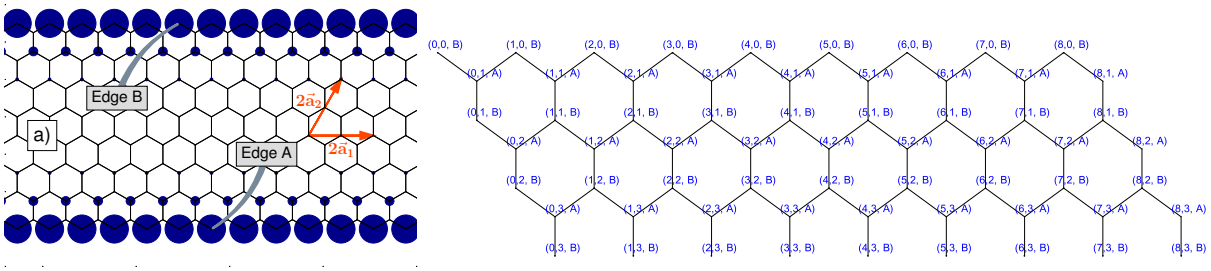

Figure 2.1.: The labeling of the graphene sites in the form (n, m, s). The maximal indices are called N and M. Periodic boundary conditions apply in x direction.

This is simplified with a Fourier transformation in the n direction, parallel to the zigzag edges, making use of the PBCs:

$$\begin{aligned} H_0 &= -t \sum_n \sum_m \sum_{k,k'} \frac{1}{\sqrt{K}} e^{-ikn} c^\dagger_{kmA\sigma} \left(\frac{1}{\sqrt{K}} e^{ik'n} c_{kmB\sigma} + \frac{1}{\sqrt{K}} e^{ik'n} c_{k(m-1)B\sigma} + \frac{1}{\sqrt{K}} e^{ik'(n+1)} c_{k(m-1)B\sigma} \right) + \text{h.c.} \\ &= -t \frac{1}{K} \sum_m \sum_{k,k'} K \delta_{k,k'} \cdot c^\dagger_{kmA\sigma} \left(c_{kmB\sigma} + c_{k(m-1)B\sigma} + e^{ik'} c_{k(m-1)B\sigma} \right) + \text{h.c.} \\ &= -t \sum_m \sum_k \cdot c^\dagger_{kmA\sigma} \left(c_{kmB\sigma} + \left(1 + e^{ik} \right) c_{k(m-1)B\sigma} \right) + \text{h.c.} \end{aligned}$$

To get real entries in the Hamiltonian, we perform a gauge transformation

$$c^{\{\dagger\}}_{kms} \to e^{\{-\}ikm/2} c^{\{\dagger\}}_{kms}$$

Physically, this transformation describes a tilt of the y- direction, orthogonal to the ribbon zigzag edge. Following this, we carry out a shift in the momenta [a]:

$$k \to k + \pi$$

which leads to a first Brillouin zone in $k \in [-\pi, \pi]$ instead of the usual values starting at zero. These two transformations yield:

$$H_0 = -t \sum_{n,k,\sigma} \left(c^\dagger_{kmA\sigma} c_{kmB\sigma} + 2 \sin\left(\frac{k}{2} \right) c^\dagger_{kmA\sigma} c_{k(m-1)B\sigma} \right) + \text{h.c.} \tag{2.2}$$

Since the aim of this work is to analyze the magnetic interactions at the zigzag edges of graphene, we are mostly interested in the edge states of the Hamiltonian. The band structure of our system is displayed in Fig. 2.2: The edge states are clearly separated from the bulk states and exist in the region $k \in \left[-\frac{\pi}{3}, \frac{\pi}{3} \right]$. In the graphene bulk, the density of states vanishes at the Fermi surface, whereas the edge states lead to a peak in the DOS near the Fermi surface. Therefore, they are subject to much stronger interaction effects.

[a] There is a typo in Ref.[38], claiming a shift of $\pi/2$. The correct value is however π, as given here.

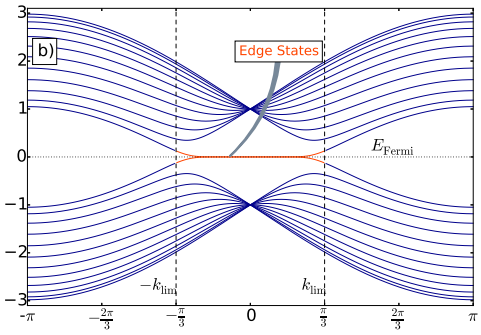

Figure 2.2.: The band structure of a plain zigzag graphene nanoribbon with only nearest-neighbor hopping (Hamiltonian Eq. (2.2)) has two degenerate flat bands near the Fermi surface. These are the edge states.

The goal of this chapter is to go over to the effective model that describes the interaction with the bulk states as a perturbation to the edges state interaction. The precise idea of this transformation was first presented by Schmidt, Golor, Lang and Wessel (Ref.[31]). Such an effective model has been introduced before by Karimi and Affleck (Ref.[32]), Schmidt and Loss (Ref.[30]), as well as Luitz, Assaad and Schmidt (Ref.[40]).

Going over to the eigenbasis of the non-interacting part of the Hamiltonian, a decoupling of the edge and bulk states in this part is achieved, and we can write

$$H_0 = \sum_{\mu\in\mathcal{E},\tau} \varepsilon^e_\mu e^\dagger_{\mu\tau} e_{\mu\tau} + \sum_{\mu\in\mathcal{B},\tau} \varepsilon^b_\mu b^\dagger_{\mu\tau} b_{\mu\tau} = H_{0,\mathrm{edge}} + H_{0,\mathrm{bulk}} \ , \tag{2.3}$$

with the abbreviations $\mathcal{E}$ for the set of edge states and $\mathcal{B}$ for the bulk states and a collective index μ that contains momentum and subband information. The index $\tau \in \{\uparrow,\downarrow\}$ stands for the spin. The edge and bulk creation operators are defined as sums over all lattice sites from the wave functions $\phi_\mu(i)$ of the H_0 eigenstates, namely $e^\dagger_{\mu\tau} = \sum_j c^\dagger_{j\tau}\varphi_\mu(j)$ and $b^\dagger_{\mu\tau} = \sum_j c^\dagger_{j\tau}\phi_\mu(j)$, respectively. With this convention, the interacting part of the Hamiltonian becomes:

$$H_U = U \sum_{\lambda\mu\nu\pi} \Gamma_{\lambda\mu\nu\pi} : d^\dagger_{\lambda\uparrow} d_{\mu\uparrow} d^\dagger_{\nu\downarrow} d_{\pi\downarrow} : \ , \tag{2.4}$$

where the operators $d^{(\dagger)}$ can be either edge or bulk operators. The interaction vertex $\Gamma_{\lambda\mu\nu\pi}$ is given by:

$$\Gamma_{\lambda\mu\nu\pi} = \sum_i \phi^*_\lambda(i)\phi_\mu(i)\phi^*_\nu(i)\phi_\pi(i). \tag{2.5}$$

For the sake of better readability we will use integers $1, 2, 3, \ldots$ as state indices, instead of the Greek letters $\lambda, \mu, \nu, \ldots$ used above. Also, we will sometimes add upper indices b,e to Γ. These indicate whether the lower indices correspond to bulk or edge state operators (e.g. $\Gamma^{\{\mathrm{ebeb}\}}_{1234}$ means that indices 1 and 3 correspond to edge states). For the edge states, the collective index $\mu = (k, \pm)$ is composed of the momentum and a band index, which is named $+$ or $-$ according

to the sign of the state energy. As visible in Fig. 2.1 (left), these edge states have equal weight on both edges each. For the following calculations and for an intuitive understanding of the processes, it will however be more useful to work in a basis with the edge states localized at one side of the ribbons, each.

This can be accomplished by a second basis transformation within the edge state subspace $\phi_{k,\{\mathrm{A/B}\}} = (\phi_{k+} \pm \phi_{k-})/\sqrt{2}$ or, equivalently, $e_{k,\mathrm{A/B},\tau} = (e_{k+,\tau} \pm e_{k-,\tau})/\sqrt{2}$. These new states are not eigenstates of H_0 (Eq. (2.3)), but their amplitudes have non-vanishing values only in the vicinity of one edge A or B. In addition, the amplitudes are non-zero only on the sublattice the edge terminates on, so that the label A/B indicates edge and sublattice simultaneously. The edge-state part of H_0 thus reads

$$H_{0,\mathrm{edge}} = \sum_{\tau,k} t(k) e^\dagger_{kA} e_{kB} + \mathrm{H.c.} \ , \tag{2.6}$$

where the k-dependent inter-edge hybridization

$$t(k) = \epsilon^e_{k+} \tag{2.7}$$

is equal to the edge state energy in Eq. (2.3).

The interacting part of the Hamiltonian Eq. (2.4) can contain any combination of edge and bulk states and hence generates the edge-bulk coupling whose contributions to the edge state interaction we will further investigate in this chapter. We define the interaction Hamiltonian H_{int}, which contains all summands of H_U except those with all four edge state operators or all four bulk state operators. It has been found before (e.g. Ref. [30]) that H_{int} is generally small, so that a projection of H_U onto the pure edge state subspace already constitutes a rather good approximation for the edge state physics. The corrections due to H_{int} can thus be treated by perturbation theory. To keep track of the order to which the interaction is taken into account, we introduce a small parameter λ with

$$H_{\mathrm{int}} \propto \lambda, \tag{2.8}$$

Physically, this parameter is small, because the overlap of delocalized bulk states with localized edge states is smaller than the overlap of the edge states with themselves: $\lambda \propto \Gamma^{bebb}, \Gamma^{eebb}, \Gamma^{eebe} \ll \Gamma^{eeee}$.

Contributions with four bulk state operators will be neglected in all following considerations, because they would enter the edge physics only in higher orders of λ.

Wannier Basis Until now, due to translation symmetry the real space edge states are still plane waves in the direction parallel to the zigzag edge, in detail:

$$\psi_{k\nu}(n,m,s) = \frac{1}{\sqrt{N}} \phi_{k\nu}(m,s)\, e^{ikn} \ .$$

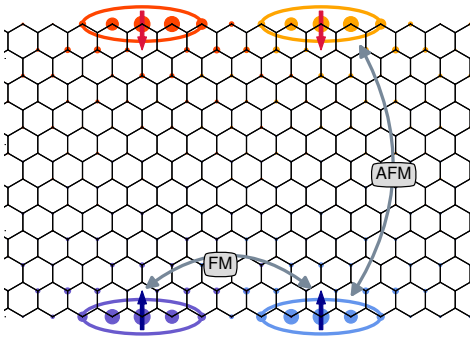

Figure 2.3.: Wannier edge states are localized at one of the ribbon edges, as well as in x-direction. In this sketch, the filled circles represent the absolute value of the actual Wannier wavefunctions, while the ellipses are guides to the eye. For better visibility we have displayed only next-neighboring states, i.e., we have left out one state in between the displayed wave functions at an edge. Due to the strong effective onsite repulsion $U\Gamma^{eeee}_{xxxx}$, each of the displayed Wannier edge states will essentially be occupied by one electron.

Since the interaction in this system is strong compared to the kinetic energy, it turns out more convenient to use a basis that is also localized along the edges. Therefore, we transform the edge states to a highly localized Wannier basis

$$e^{\dagger}_{xs\tau} = \sqrt{\frac{1}{K}} \sum_{|k|\leq k_{\mathrm{lim}}} e^{ikax} e^{\dagger}_{ks\tau} \qquad \text{with } a = \frac{\pi}{k_{\mathrm{lim}}}$$

where K is the number of momenta in the sum, i.e., the number of momenta that fulfill $|k| \leq k_{\mathrm{lim}}$. The scaling factor a must be used to keep the transformation unitary despite the fact that it only covers roughly one third of the Brillouin zone. In Fig. 2.3 one sees the spreading of these Wannier states in real space.

Now that the Wannier basis has been introduced, it becomes apparent that by far the largest term in H_U is the effective onsite repulsion

$$H_{\mathrm{onsite}}(\mu) = \Gamma^{eeee}_{\mu\mu\mu\mu} : \hat{n}_{\mu\uparrow} :: \hat{n}_{\mu\downarrow} : \tag{2.9}$$

of any one localized Wannier state μ. Therefore, considering also the normal ordering of the terms, it is energetically extremely favorable to have each such Wannier edge state occupied by exactly one electron. The onsite repulsion is independent from the Wannier index μ, and numerical calculations reveal that $\Gamma_{xxxx} \approx 0.1$ only very weakly depends on the ribbon width and length. The second major step in the effective description will therefore be a transformation to a Heisenberg spin basis, so that each edge state hosts effectively one spin.

2.1.2. First order calculation results

In this section, we review the previous results from treating the edge-bulk interaction to first order in λ. These have already been presented in Ref. [31], where the stress was on the investigation of interactions in chiral ribbons. Those ribbons have a specially tailored geometry, which allows for a very good separation of edge states along one edge and leads to a faster decaying intra-edge coupling. It has been shown in Ref. [38] that the calculation can also be applied to plain zigzag ribbons with slightly modified Wannier states.

At first, the fermionic edge couplings have to be derived. To do so, we restrict the Fock space to those states in which all bulk states with energies below the Fermi level (i.e. negative energies) are occupied, while those with positive energies are empty. As a consequence, all terms in Eq. (2.4) in which the bulk operators do not appear in creator-annihilator pairs are dropped, because they map a state out of the restricted Fock space.

Afterwards, the remaining bulk operators are averaged with respect to the Fermi sea:

$$b_{1\tau}^\dagger b_{2\tau'} \quad \rightarrow \quad \delta_{12}\delta_{\tau\tau'}\Theta\left(-\varepsilon_1^b\right). \tag{2.10}$$

With these approximations the effective edge state interactions can be written as

$$H_U \approx U \sum_{\lambda\mu\nu\pi} \Gamma_{\lambda\mu\nu\pi} : e_{\lambda\uparrow}^\dagger e_{\mu\uparrow} :: e_{\nu\downarrow}^\dagger e_{\pi\downarrow} : \ . \tag{2.11}$$

Note that in order to derive Eq. (2.11) it is not sufficient to just drop all terms with bulk operators from Eq. (2.4). It is essential to perform the bulk state average properly, as described above. Additionally employing particle-hole symmetry of H_0, however, the first order of H_{int} can be absorbed completely into the normal ordering of the edge state operators in Eq. (2.11). Note also that Eq. (2.11) is valid for any choice of basis in the edge state subspace. In Ref. [31], this approximate fermionic theory was solved with exact diagonalization for small systems, and it was shown that already at this level the reduced theory can compete with QMC calculations. However, the most useful and intuitive description can only be reached after going over to the Wannier states and the effective spin basis, as described above. The effective hopping occurs only between states on the same edge and sublattice; it is obtained from Eq. (2.7) and transformed to real space via

$$t_{xx'}^* = \frac{1}{K} \sum_{|k|\leq k_{\text{lim}}} t\left(k\right) e^{ia(x-x')k} \qquad a = \frac{\pi}{k_{\text{lim}}} \tag{2.12}$$

Please bear in mind that this is a different quantity than the original lattice hopping: $t_{xx'}^* \neq t$.

We can directly read the ferromagnetic intra-edge coupling between two Wannier sites

$$J^{\text{F}} = 2U\Gamma_{xxx'x'} \tag{2.13}$$

and a straight-forward second-order perturbation theory analysis (with $t_{xx'}^*/U \ll 1$) yields the anti-ferromagnetic intra-edge coupling

$$J^{\text{AF}} = -\frac{4\ \left(t_{xx'}^*\right)^2}{U\Gamma_{xxxx}} \tag{2.14}$$

These interactions are also sketched in Fig. 2.3.

2.2. Schrieffer-Wolff transformation and second-order corrections

2.2.1. Fermionic coupling terms

The effect of the bulk states on the edge state interaction is approximated up to second order by means of a Schrieffer-Wolff transformation. The details of this calculation were already published in the Masters's thesis, Ref. [39], but for the sake of coherence and better readability, the key steps will be briefly repeated here. We consider the single-particle bulk Hamiltonian $H_{0,\mathrm{bulk}}$ as the unperturbed Hamiltonian and the interaction between edge and bulk states H_{int} as its perturbation. The free part of the edge state Hamiltonian is kept separately, which means that we neglect the time-dependence of the edge state operators in the corrections. This constitutes a good approximation for sufficiently broad ribbons in which the inter-edge hybridization $t(k)$ is small compared to the typical bulk state energies $\epsilon_\mu^{(b)}$. Formally, the second-order Schrieffer-Wolff correction can be written as

$$H_{\mathrm{SW}} = -\lim_{\eta\to 0}\frac{i}{2}\int_0^\infty dt\; e^{-\eta t}\left[H_{\mathrm{int}}(t), H_{\mathrm{int}}\right], \tag{2.15}$$

where $H_{\mathrm{int}}(t) = \exp\left(itH_{0,\mathrm{bulk}}\right) H_{\mathrm{int}} \exp\left(-itH_{0,\mathrm{bulk}}\right)$. As before, the bulk operators are eliminated from H_{SW} by appropriate averaging [Eq. (2.10)].

After some tedious but straightforward calculations we obtain the complete fermionic expression of the second order Schrieffer-Wolff terms

$$H_{\mathrm{SW}} = H_{\mathrm{SW}}^{2p} + H_{\mathrm{SW}}^{1p} + H_{\mathrm{SW}}^{3p}, \tag{2.16}$$

where the individual constituents are effective two-particle, one-particle and three-particle interactions, respectively.

For a detailed derivation of the terms, compare Ref. [39]. In the beginning, the full expression looks somehow involved, but it can be brought in a systematic order, and some terms can be neglected right away. Moreover, calculations will reveal in the following that the contributions of some other terms are also small.

To rewrite the expression, we use the Pauli matrices $\sigma^{x,y,z}$ and the unit matrix σ^0, and we define:

$$\hat{\sigma}^\mu_{12,\mathrm{s}} = \sum_{\tau\tau'} \sigma^\mu_{\tau\tau'} e^\dagger_{1s\tau} e_{2s\tau'}$$

So that for example $\hat{\sigma}^z_{12}\hat{\sigma}^z_{34} = \left(e^\dagger_{1\uparrow}e_{2\uparrow} - e^\dagger_{1\downarrow}e_{2\downarrow}\right)\left(e^\dagger_{3\uparrow}e_{4\uparrow} - e^\dagger_{3\downarrow}e_{4\downarrow}\right)$. The index $s \in \{A, B\}$ corresponds to the sublattice, or equivalently the edge where the state is localized. s' can be the

same or the opposite edge as s, while $\bar{s}$ always refers to the opposite sublattice and ribbon edge. Using this, the intra-edge case simplifies to:

$$\begin{aligned} H_{\mathrm{SW}}^{\mathrm{intra}} &= -U^2 \sum_{\substack{1,2,3,4 \\ s}} \sum_{\sigma} \left(L_{\mathrm{ph}\ ss}^{1234} + M_{\mathrm{ph}\ s}^{1234}\right) \left(:e_{1s\sigma}^{\dagger} e_{2s\sigma} e_{3s\sigma}^{\dagger} e_{4s\sigma}: + 2\cdot: e_{1s\downarrow}^{\dagger} e_{2s\uparrow} e_{3s\uparrow}^{\dagger} e_{4s\downarrow}:\right) \\ &\quad - 2\left(L_{\mathrm{pp}\ ss}^{1234} + M_{\mathrm{pp}\ s}^{1234}\right) : e_{1s\downarrow}^{\dagger} e_{2s\uparrow} e_{3s\uparrow}^{\dagger} e_{4s\downarrow}: \\ &= \frac{U^2}{2} \sum_{1234} \left\{ \left(L_{\mathrm{ph}\ ss}^{1234} + M_{\mathrm{ph}\ s}^{1234}\right) \sum_{\nu=0,x,y,z} \hat{\sigma}_{12,\mathrm{s}}^{\mu} \hat{\sigma}_{34,\mathrm{s}}^{\mu} + \frac{1}{2}\left(L_{\mathrm{pp}\ ss}^{1234} + M_{\mathrm{pp}\ ss}^{1234}\right) \cdot \left\{ \hat{\sigma}_{12,\mathrm{s}}^{0} \hat{\sigma}_{34,\mathrm{s}}^{0} - \sum_{\mu=x,y,z} \hat{\sigma}_{12,\mathrm{s}}^{\nu} \hat{\sigma}_{34,\mathrm{s}}^{\nu} \right\} \right\} \\ &= \frac{U^2}{2} \sum_{1234} \left(A_{-}^{1234,s} \sum_{\mu=x,y,z} \hat{\sigma}_{12,\mathrm{s}}^{\mu} \hat{\sigma}_{34,\mathrm{s}}^{\mu} + A_{+}^{1234,s} \hat{\sigma}_{12,\mathrm{s}}^{0} \hat{\sigma}_{34,\mathrm{s}}^{0} \right) \end{aligned} \tag{2.17}$$

where we have defined

$$A_{\pm}^{1234,s} = L_{\mathrm{ph}\ ss}^{1432} + M_{\mathrm{ph}\ s}^{1432} \pm \frac{1}{2}\left(L_{\mathrm{pp}\ ss}^{1234} + M_{\mathrm{pp}\ s}^{1234}\right)$$

In the inter- edge couplings, one expression cannot be rewritten using spin operators, and the result is:

$$\begin{aligned} H_{\mathrm{SW}}^{\mathrm{inter}} &= U^2 \sum_{1234,s} \sum_{\sigma} \Big\{ -L_{\mathrm{ph}\ s\bar{s}}^{1234} \left(:e_{1s\sigma}^{\dagger} e_{2\bar{s}\sigma} e_{3\bar{s}\sigma}^{\dagger} e_{4s\sigma}: - :e_{1s\bar{\sigma}}^{\dagger} e_{2\bar{s}\bar{\sigma}} e_{3\bar{s}\sigma}^{\dagger} e_{4s\sigma}:\right) : \\ &\quad + L_{\mathrm{pp}\ s\bar{s}}^{1234} : e_{1s\bar{\sigma}}^{\dagger} e_{2\bar{s}\bar{\sigma}} e_{3s\sigma}^{\dagger} e_{4\bar{s}\sigma}: - \sum_{12,s} \sum_{\sigma} \left(B_{s\bar{s}}^{12} + T_{s\bar{s}}^{12}\right) : e_{1s\sigma}^{\dagger} e_{2\bar{s}\sigma}: \Big\} \\ &= \frac{U^2}{2} \sum_{1234,s} \left(\sum_{\mu=x,y,z} L_{\mathrm{ph}\ s\bar{s}}^{1234} \hat{\sigma}_{14,\mathrm{s}}^{\mu} \hat{\sigma}_{32,\bar{s}}^{\mu} + 2 L_{\mathrm{pp}\ s\bar{s}}^{1234} : e_{1s\bar{\sigma}}^{\dagger} e_{2\bar{s}\bar{\sigma}} e_{3s\sigma}^{\dagger} e_{4\bar{s}\sigma}: \right) - U^2 \sum_{12,s} \sum_{\sigma} \left(B_{s\bar{s}}^{12} + T_{s\bar{s}}^{12}\right) : e_{1s\sigma}^{\dagger} e_{2\bar{s}\sigma} \end{aligned} \tag{2.18}$$

The prefactors are given by the overlap of the eigenfunctions of the pure hopping Hamiltonian, divided by some energies and energy differences, in detail:

$$L_{\mathrm{ph}\ ss'}^{1234} = \sum_{\substack{5\ \mathrm{occ} \\ 6\ \mathrm{emp}}} \frac{1}{\varepsilon_5 - \varepsilon_6} \Gamma_{1456,\ \mathrm{s}}^{eebb} \Gamma_{6532,\ \mathrm{s'}}^{bbee} \qquad M_{\mathrm{ph}\ s}^{1234} = \sum_{5\ \mathrm{occ}} \sum_{6 \in \mathrm{edge}} \frac{1}{\varepsilon_5} \Gamma_{1564,\mathrm{s}}^{ebee} \Gamma_{3652,\ \mathrm{s}}^{eebe} \tag{2.19}$$

$$L_{\mathrm{pp}\ ss'}^{1234} = \sum_{\substack{5\ \mathrm{occ} \\ 6\ \mathrm{occ}}} \frac{1}{\varepsilon_5 + \varepsilon_6} \Gamma_{1536,\ \mathrm{s}}^{ebeb} \Gamma_{5462,\ \mathrm{s'}}^{bebe} \qquad M_{\mathrm{pp}\ s}^{1234} = \sum_{5\ \mathrm{occ}} \sum_{6 \in \mathrm{edge}} \frac{1}{\varepsilon_5} \Gamma_{1635,\ \mathrm{s}}^{eeeb} \Gamma_{5462\ \mathrm{s}}^{beee} \tag{2.20}$$

and the prefactors of the effective hopping are given by:

$$B_{s\bar{s}}^{12} = \sum_{\substack{3,4\ \mathrm{emp} \\ 5\ \mathrm{occ}}} \frac{\Gamma_{5314\ \mathrm{s}}^{bbeb} \Gamma_{3245\ \bar{s}}^{bebb}}{\varepsilon_3 + \varepsilon_4 - \varepsilon_5} \qquad T_{s\bar{s}}^{12} = \sum_{\substack{3,4\ \mathrm{emp} \\ 5\ \mathrm{occ}}} \frac{1}{\varepsilon_5} \Gamma_{3352\ \bar{s}}^{bbeb} \Gamma_{1544\ \mathrm{s}}^{ebbb} \tag{2.21}$$

The summations run over all bulk states with $\varepsilon_b > \varepsilon_{\mathrm{Fermi}}$ for those marked as "occ" (=occupied), or over all bulk states with $\varepsilon_b < \varepsilon_{\mathrm{Fermi}}$ for those marked as "emp"(=empty). The expressions

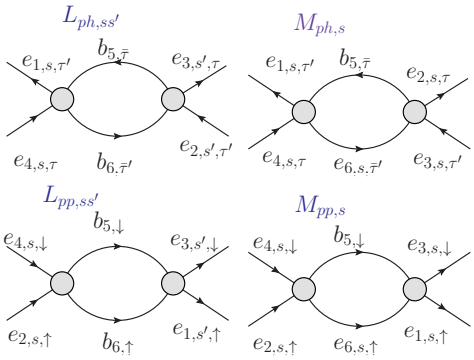

Figure 2.4.: Diagrammatic representation of the processes yielding an effective two-particle interaction. The particle-hole diagrams (index ph) are composed of a direct and a crossed particle-hole channel, where the latter is only available for equal sublattice indices. This graphic has been published before in [38], a typo in M_{ph} was corrected here.

L_{ph}, M_{ph} and M_{pp}, L_{pp} are essentially particle-hole and particle-particle response functions, respectively. The direct particle-hole channel is available for inter-edge and intra-edge processes, whereas the crossed particle-hole channel only gives a contribution to interactions between states on the same edge. Although we do not use diagrammatic perturbation theory, these interactions can be visualized in Hugenholtz diagrams. For the effective two-particle interactions, compare Fig. 2.4.

Let us briefly notice that the term L^{1221}_{ph} has a special meaning: It can be interpreted as the bulk-mediated RKKY interaction between the electron spins of states 1 and 2. The Rudermann-Kittel-Kasuya-Yosida coupling[41–43] in general describes the interaction between two magnetic impurities via bulk conducting electrons. For half filled graphene it has been shown[44, 45] that the RKKY coupling is ferromagnetic for moments on the same sublattice and antiferromagnetic for opposite sublattices. We will see that here L^{1221}_{ph} follows the same rule when going over to the spin basis in Sec.2.3.

Three particle coupling term Despite the averaging over the Fermi surface, one is at first left with a single summand that leads to a three particle interaction:

$$H^{3p}_{\mathrm{SW}} = -U^2 \sum_{\substack{1,3,6\\2,4,5}} \sum_{s,\tau} 2W^{1,2,3}_{s,\bar{s}\,4,5,6} : e^{\dagger}_{1s\bar{\tau}} e_{2\bar{s}\bar{\tau}} e^{\dagger}_{3s\tau} e_{4\bar{s}\tau} e^{\dagger}_{5\bar{s}\tau} e_{6s\tau} : \tag{2.22}$$

where the prefactor describes the contraction

$$W^{1,2,3}_{s,\bar{s}\,4,5,6} = \sum_{7\ \mathrm{occ}} \frac{1}{\epsilon^b_7} \Gamma^{ebee}_{1736,s} \Gamma^{beee}_{7254,\bar{s}} \tag{2.23}$$

This term combines a hopping of one electron from one edge to the other (with spin $\bar{\tau}$) with a two-particle exchange interaction on different edges (with spin τ). It either couples more than

two sites, in which case is does not contribute due to the approximations described in Sec.2.3. Or, if indices $3 = 6$ and $4 = 5$, the term vanishes when going over to the spin basis in sec. 2.3, where it describes a single hopping multiplied with an expectation value in normal order:

$$W_{\bar{s}s}(x,y) = \sum_{2,3\in\mathcal{E}}^{x,y,3} W_{\bar{s}s}^{3,2,2} \langle : \hat{n}_{2\bar{\tau}} : \rangle \langle : \hat{n}_{3\bar{\tau}} : \rangle = 0 \tag{2.24}$$

2.2.2. Translation to momentum space

To perform an actual calculation of the expressions Eq. (2.19) and Eq. (2.20) possible within the range of computing capacity, they must be rewritten in momentum space. The basis transformation of the wave vectors is:

$$\psi_x(n,m) = \frac{1}{\sqrt{NK}} \sum_k e^{-iakx} \cdot e^{ik\left(n+\frac{m}{2}\right)} \cdot (-i)^{2n+m} \phi_k(m)$$

where $\phi_k(m)$ are the eigenvectors of the two dimensional Hamiltonian Eq. (2.2) in matrix form, $\exp(ikn)$ is the plain wave continuation of these eigenstates in the direction of the periodic boundary conditions, and $(-i)^{(2n+m)} \cdot \exp\left(ik\frac{m}{2}\right)$ is the gauge transformation used to get real eigenstates in the end. The last factor, e^{-ikax} describes the actual transformation to momentum space. Due to momentum conservation, each Γ-coefficient only depends on three different momenta, instead of four real space indices:

$$\begin{aligned}\Gamma_{1234} &= \frac{1}{N^2} \sum_{n,m} \psi_{x1}^*(n,m)\, \psi_{x2}(n,m)\, \psi_{x3}^*(n,m)\, \psi_{x4}(n,m) \\ &= \frac{1}{NK^2} \sum_m \sum_{k,k',q} \exp\left[-ia\left(kx_1 - (k+q)x_2 + k'x_3 - (k'-q)x_4\right)\right] \phi_k^*(m)\, \phi_{k+q}(m)\, \phi_{k'}^*(m) \cdot \phi_{k'-q}(m)\end{aligned}$$

Inserting this into the expressions for the effective couplings gives results that also only depend on three momenta instead of four different indices. This reflects the momentum conservation of the processes described in Fig. (2.4). The indices of bulk states split into a momentum and a band index, the edge states are uniquely characterized by their momentum and sublattice. One possible representation is:

$$L_{\text{ph } ss'}(k,k',q) = \sum_{\substack{b_2 \text{ occ} \\ b_3 \text{ emp}}} \sum_p \frac{\Gamma^{eebb,\text{s}}_{k,k+q,(p,b2),(p-q,b3)} \Gamma^{bbee,\text{ s'}}_{(p-q,b3),(p,b2),k',k'-q}}{\varepsilon_{b_2,p} - \varepsilon_{b_3,p-q}}$$

and

$$L_{\text{pp } ss'}(k,k',q) = \sum_{\substack{b_2 \text{ occ} \\ b_3 \text{ occ}}} \sum_p \frac{\Gamma^{ebeb,\text{ s}}_{k,(b2,k'+p),k',(b3,k-p)} \Gamma^{bebe,\text{ s'}}_{(b2,k'+p),k+q,(b3,k-p),k'-q}}{\varepsilon_{b2,k'+p} + \varepsilon_{b3,k-p}}$$

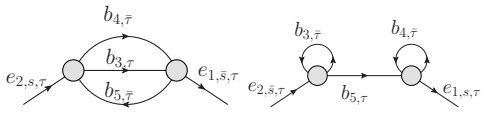

Figure 2.5.: There are two effective one-particle hopping processes.

and

$$M^{1234}_{\mathrm{ph}\ s}\left(k,k',q\right) = \sum_{b_2\ \mathrm{occ}} \sum_{p} \frac{\Gamma^{ebee}_{k,(b2,p-q),p,k+q}\Gamma^{eebe}_{k',p,(b2,p-q),k'-q}}{\varepsilon_{b2,p-q}}$$

$$M^{1234}_{\mathrm{pp}\ s}\left(k,k',q\right) = \sum_{b_2\ \mathrm{occ}} \sum_{p} \frac{\Gamma^{eeeb}_{k,p,k',(b2,k+k'-p)}\Gamma^{beee}_{(b2,k+k'-p),k+q,p,k'-q}}{\varepsilon_{b5,k+k'-q}}$$

In the following, we will only be interested in terms with two different indices, so out of the four external momenta, two have to be pairwise equal. This is a consequence of the averaging with respect to the Fermi sea, analogous to Sec. 2.1.2: In the Wannier basis, each state is effectively filled with one electron, and we will only regard second-order processes that return to this state of half-filling, because all others are severely suppressed by the effective onsite repulsion $U^* = U\Gamma^{eeee}_{xxxx}$. Double occupied or empty Wannier states are solely allowed as virtual intermediate states of the second-order processes.

For the effective one-particle interactions, the external momentum is fixed. For the second one, the index pairs within one overlap coefficient are fixed:

$$B_{\mathrm{s}}\left(k\right) = \sum_{\substack{b_3,b_4\ \mathrm{occ}\\ b_5\ \mathrm{emp}}} \sum_{p,q} \frac{\Gamma^{bbeb\ \mathrm{s}}_{(b5,p),(b3,p-q),k,(b4,k+q)}\Gamma^{bebb\ \mathrm{s}}_{(b3,p-q),k,(b4,k+q),(b5,p)}}{\varepsilon_{b3,p-q} + \varepsilon_{b4,k+q} - \varepsilon_{b5,p}}$$

$$T_{\mathrm{s}}\left(k\right) = \sum_{\substack{b_3,b_4\ \mathrm{emp}\\ b_5\ \mathrm{occ}}} \sum_{p,q} \frac{1}{\varepsilon_{b5,k}}\Gamma^{bbeb\ \mathrm{s}}_{(b3,p),(b3,p),k,(b5,k)}\Gamma^{ebbb\ \mathrm{s}}_{k,(b5,k),(b4,q),(b4,q)}$$

When transforming back to real space, we are explicitly interested in cases with only two different external indices. In general, the following transformation is used:

$$\begin{aligned} L^{1234}_{\mathrm{ph}} &= \frac{1}{K^2}\sum_{k,k',q} \exp\left[ia\cdot\left(kx_1 - \left(k'-q\right)x_2 + k'x_3 - \left(k+q\right)x_4\right)\right] L_{\mathrm{ph}}\left(k,k',q\right) \\ &= \frac{1}{K^2}\sum_{k,k',q} \exp\left[ia\cdot\left(kx_1 - \left(k'-q\right)x_2 + k'x_3 - \left(k+q\right)x_4\right)\right] L^{k,\left(k'-q\right),k',(k+q)}_{\mathrm{ph}} \end{aligned}$$

The particle-hole loop only gives two different cases of this, when we take into account that the eigenstates are purely real:

$$L_{\mathrm{ph}}^{\alpha\beta\alpha\beta} = \frac{1}{K^2} \sum_{k,k',q} \exp\left[ia\left\{\left(k+k'\right)\alpha - \left(k+k'\right)\beta\right\}\right] L_{\mathrm{ph}}\left(k,k',q\right)$$

and

$$L_{\mathrm{ph}}^{\alpha\alpha\beta\beta} = \frac{1}{K^2} \sum_{k,k',q} \exp\left[ia\left\{\left(k-k'+q\right)\alpha - \left(k-k'+q\right)\beta\right\}\right] L_{\mathrm{ph}}\left(k,k',q\right)$$

$$\text{with } \left[p=-k'+q\right] = \frac{1}{K^2} \sum_{k,p,q} \exp\left[ia\left\{\left(k+p\right)\alpha - \left(k+p\right)\beta\right\}\right] \sum_{\substack{b_2\ \mathrm{occ}\\ b_3\ \mathrm{emp}}} \sum_{\tilde{p}} \frac{\Gamma^{eebb}_{k,k+q,(b2,\tilde{p}),(b3,\tilde{p}-q)} \Gamma^{bbee}_{(b3,\tilde{p}-q),(b2,\tilde{p}),-p+q,-p}}{\varepsilon_{b2,\tilde{p}} - \varepsilon_{b3,\tilde{p}-q}}$$

Due to the eigenvectors being fully real, a further rewriting is possible:

$$\begin{aligned}
\ldots =& \frac{1}{K^2} \sum_{k,p,q} \exp\left[ia\left\{\left(k+p\right)\alpha - \left(k+p\right)\beta\right\}\right] \sum_{\substack{b_2\ \mathrm{occ}\\ b_3\ \mathrm{emp}}} \sum_{\tilde{p}} \frac{\Gamma^{eebb}_{k,k+q,(b2,\tilde{p}),(b3,\tilde{p}-q)} \Gamma^{bbee}_{(b3,\tilde{p}-q),(b2,\tilde{p}),-p,-p+q}}{\varepsilon_{b2,\tilde{p}} - \varepsilon_{b3,\tilde{p}-q}} \\
=& \frac{1}{K^2} \sum_{k,p,q} \exp\left[ia\left\{\left(k+p\right)\alpha - \left(k+p\right)\beta\right\}\right] \sum_{\substack{b_2\ \mathrm{occ}\\ b_3\ \mathrm{emp}}} \sum_{\tilde{p}} \frac{\Gamma^{eebb}_{k,k+q,(b2,\tilde{p}),(b3,\tilde{p}-q)} \Gamma^{bbee}_{(b3,\tilde{p}-q),(b2,\tilde{p}),p,(p-q)}}{\varepsilon_{b2,\tilde{p}} - \varepsilon_{b3,\tilde{p}-q}} \\
=& L_{\mathrm{ph}}^{\alpha\beta\alpha\beta}
\end{aligned}$$

In the second-last step we have used that the edge states obtained from Eq. (2.6) have a certain symmetry depending on their sublattice :

$$\begin{aligned}
\vec{\phi}_{kA} &= \left(a_1, 0, a_2, 0, a_3, 0, a_4, 0, \ldots\right)^T & \vec{\phi}_{-kA} &= \left(a_1, 0, -a_2, 0, a_3, 0, -a_4, 0, \ldots\right)^T \\
\vec{\phi}_{kB} &= \left(0, b_1, 0, b_2, 0, b_3, 0, b_4, 0, \ldots\right)^T & \vec{\phi}_{-kB} &= \left(0, -b_1, 0, b_2, 0, -b_3, 0, b_4, 0, \ldots\right)^T
\end{aligned}$$

Different from this is the third case:

$$L_{\mathrm{ph}}^{\alpha\beta\beta\alpha} = \frac{1}{K^2} \sum_{k,p,q} \exp\left[ia\left\{-q\alpha + q\beta\right\}\right] L_{\mathrm{ph}}\left(k,k',q\right)$$

For the parameter of the particle-particle interaction, it is also possible to unify two of the three different orders of index pairs using the fact that the eigenstates are real:

$$\begin{aligned}
L_{\mathrm{pp}}^{\alpha\alpha\beta\beta} &= \frac{1}{K^2}\sum_{k,k',q}\exp\left[ia\left\{k\alpha-\left(k'-q\right)\alpha+k'\beta-\left(k+q\right)\beta\right\}\right]L_{\mathrm{pp}}\left(k,k',q\right)\\
&= \frac{1}{K^2}\sum_{k,k',q}\exp\left[ia\left\{\left(k-k'-q\right)\alpha-\left(k-k'+q\right)\beta\right\}\right]\\
&\quad\cdot\sum_{\substack{b_2\ \mathrm{occ}\\ b_3\ \mathrm{occ}}}\sum_{\tilde{p}}\frac{\Gamma^{ebeb,\ \mathrm{s}}_{k,(b2,k'+\tilde{p}),k',(b3,k-\tilde{p})}\Gamma^{bebe,\ \mathrm{s'}}_{(b2,k'+\tilde{p}),k+q,(b3,k-\tilde{p}),k'-q}}{\varepsilon_{b2,k'+\tilde{p}}+\varepsilon_{b3,k-\tilde{p}}}\\
\overset{\text{with}}{\{p=-k+k'-q\}} &= \frac{1}{K^2}\sum_{k,k',p}\exp\left[ia\left\{-p\alpha+p\beta\right\}\right]\sum_{\substack{b_2\ \mathrm{occ}\\ b_3\ \mathrm{occ}}}\sum_{\tilde{p}}\frac{\Gamma^{ebeb,\ \mathrm{s}}_{k,(b2,k'+\tilde{p}),k',(b3,k-\tilde{p})}\Gamma^{bebe,\ \mathrm{s'}}_{(b2,k'+\tilde{p}),-p+k',(b3,k-\tilde{p}),p+k}}{\varepsilon_{b2,k'+\tilde{p}}+\varepsilon_{b3,k-\tilde{p}}}\\
\text{for real e.s.} &= \frac{1}{K^2}\sum_{k,k',p}\exp\left[ia\left\{-p\alpha+p\beta\right\}\right]\sum_{\substack{b_2\ \mathrm{occ}\\ b_3\ \mathrm{occ}}}\sum_{\tilde{p}}\frac{\Gamma^{ebeb,\ \mathrm{s}}_{k,(b2,k'+\tilde{p}),k',(b3,k-\tilde{p})}\Gamma^{bebe,\ \mathrm{s'}}_{(b2,k'+\tilde{p}),p+k,(b3,k-\tilde{p}),k'-p}}{\varepsilon_{b2,k'+\tilde{p}}+\varepsilon_{b3,k-\tilde{p}}}\\
&= \frac{1}{K^2}\sum_{k,k',q}\exp\left[ia\left\{-p\alpha+p\beta\right\}\right]\cdot L_{\mathrm{pp}}\left(k,k',q\right)\\
&= L_{\mathrm{pp}}^{\alpha\beta\beta\alpha}
\end{aligned}$$

and different from these two

$$L_{\mathrm{pp}}^{\alpha\beta\alpha\beta} = \frac{1}{K^2}\sum_{k,k',q}\exp\left[ia\left\{\left(k+k'\right)\alpha-\left(k+k'\right)\beta\right\}\right]\cdot L_{\mathrm{pp}}\left(k,k',q\right)$$

With analogous substitutions, the M-parameters can be transformed to real space and rearranged:

$$M_{\mathrm{ph}}^{\alpha\beta\alpha\beta} = M_{\mathrm{ph}}^{\alpha\alpha\beta\beta} = \frac{1}{K^2}\sum_{k,k',q}\exp\left[ia\left\{\left(k+k'\right)\alpha-\left(k+k'\right)\beta\right\}\right]M_{\mathrm{ph}}\left(k,k',q\right)$$

$$M_{\mathrm{ph}}^{\alpha\beta\beta\alpha} = \frac{1}{K^2}\sum_{k,p,q}\exp\left[ia\left\{-q\alpha+q\beta\right\}\right]M_{\mathrm{ph}}\left(k,k',q\right)$$

and

$$M_{\mathrm{pp}}^{\alpha\alpha\beta\beta} = M_{\mathrm{pp}}^{\alpha\beta\beta\alpha} = \frac{1}{K^2}\sum_{k,k',q}\exp\left[ia\left\{-p\alpha+p\beta\right\}\right]\cdot M_{\mathrm{pp}}\left(k,k',q\right)$$

$$M_{\mathrm{pp}}^{\alpha\beta\alpha\beta} = \frac{1}{K^2}\sum_{k,k',q}\exp\left[ia\left\{\left(k+k'\right)\alpha-\left(k+k'\right)\beta\right\}\right]\cdot M_{\mathrm{pp}}\left(k,k',q\right)$$

2.3. Heisenberg spin basis

In the localized Wannier basis described in Sec. 2.1.1, the term $U\Gamma_{xxxx}$ is larger than all other contributions. Due to this dominant effective Hubbard Hamiltonian, half filling is strongly

favored for the Wannier states, and all processes that map a homogeneous charge occupation in the edge state to a state with broken charge homogeneity will be suppressed, as states above. Half filling in the Wannier states is also associated with charge neutrality on each original lattice site. When gaining an overview over the large variety of interactions in Sec. 2.2.1, we therefore want to focus on those that create and annihilate maximally one doubly occupied or empty state, and will will discard all terms that lead to a stronger deviation from charge neutrality. When doing so, we are only left with two sorts of terms:

1. There are two-particle terms, which have two pairs of equal external indices. They can be written as spin-spin interactions in the fermionic basis, such as in Eqs. (2.17) and the first part of (2.18)
2. The second class of terms are those in the second part of Eq. (2.18), describing a single hopping between sites on different sublattices. In the final interaction this adds to the effective hopping $t^*_{xx'}$ (2.12), but both are suppressed by the onsite repulsion $U\Gamma_{xxxx}$.

All two-particle interactions with three different external indices vanish due to the previous approximations: They either contain contributions $\propto e^\dagger_{x,\tau} e_{z,\tau} e^\dagger_{y\tau'} e_{z\tau'}$ (or with two identical creation operator indices, respectively); this process has a double unbalanced hopping and couples to a double occupied (or empty) state. Or otherwise interactions of three edge states contain the expectation value of one particle-counting operator, which vanishes analogous to Eq. (2.24) due to normal ordering.

Since the Wannier edge states are essentially occupied by one electron, all further interaction terms only affect the remaining degree of freedom, which is the electron spin. When going over to a Heisenberg spin basis, terms of type (a) translate directly to a spin-spin interaction. Terms of type (b) are treated by second order perturbation theory analogous to the derivation of Eq. (2.14), where the small parameter in this case is the new effective hopping Eq. (2.21) divided by $U\Gamma_{xxxx}$.

In the following we will regard the interactions between pairs of Wannier states, either on the same or on opposite edges. The effective spin basis for each such pair of Wannier states in the half filled subspace is given by $\{|\uparrow\uparrow\rangle, |\downarrow\downarrow\rangle, |\uparrow\downarrow\rangle, |-\updownarrow\rangle, |\updownarrow -\rangle\}$. The last two entries denote the state with both electrons in one Wannier state, the formal order of the spins is however still important to keep track of the fermionic signs. In the double arrow symbol $\updownarrow$, we will always assume the upwards spin to count first.

With a shift in the total energy, all terms in the full fermionic Hamiltonian relevant for these two Wannier states can be written as a 6×6 matrix, consisting of 2×2 blocks

$$\begin{array}{c} \\ |\uparrow\uparrow\rangle \\ |\downarrow\downarrow\rangle \\ |\uparrow\downarrow\rangle \\ |\downarrow\uparrow\rangle \\ |\updownarrow -\rangle \\ |-\updownarrow\rangle \end{array} \begin{array}{c} \begin{array}{ccc} |\uparrow\uparrow\rangle\,|\downarrow\downarrow\rangle & |\uparrow\downarrow\rangle\,|\downarrow\uparrow\rangle & |\updownarrow -\rangle\,|-\updownarrow\rangle \end{array} \\ \begin{pmatrix} \mathbf{0} & \mathbf{0} & \mathbf{0} \\ \mathbf{0} & H_{\mathrm{le}} & H_{\mathrm{hop}} \\ \mathbf{0} & H^\dagger_{\mathrm{hop}} & H_{\mathrm{he}} \end{pmatrix} \end{array} \tag{2.25}$$

where H_{le} contains all terms of type (a), and H_{hop} all terms of type (b). The particular forms of these two blocks depend on the mutual positions of the two Wannier centers under consideration

and will be discussed in the following. The block H_{he} contains the effective Hubbard interaction Eq. (2.9). It separates the high-energy subspace with doubly occupied Wannier states from the low-energy subspace with single occupations. Due to SU(2) invariance, the states $|\uparrow\uparrow\rangle$ and $|\downarrow\downarrow\rangle$ are decoupled from the other states.

As usual, the residual spin dynamics in the low-energy subspace is then obtained by second order perturbation theory

$$H_{\mathrm{spin}} = H_{\mathrm{le}} - H_{\mathrm{hop}} H_{\mathrm{he}}^{-1} H_{\mathrm{hop}}^{\dagger}. \tag{2.26}$$

H_{spin} can be expressed in terms of spin operators. In the following we discuss the two different cases of inter-edge coupling (the Wannier sites are on different edges) and intra-edge coupling (the two Wannier sites are on the same edge $s = s'$).

2.3.1. Inter-edge coupling

We consider two Wannier states xA and $x'B$ on opposite edges. The low energy part of the inter-edge coupling reads

$$H_{\mathrm{le}}^{\mathrm{inter}} = \begin{array}{c} \\ |\uparrow\downarrow\rangle \\ |\downarrow\uparrow\rangle \end{array} \begin{array}{c} \begin{array}{cc} |\uparrow\downarrow\rangle & |\downarrow\uparrow\rangle \end{array} \\ \begin{pmatrix} -\chi_{xx'} & \chi_{xx'} \\ \chi_{xx'} & -\chi_{xx'} \end{pmatrix} \end{array}, \tag{2.27}$$

where

$$\chi_{xx'} = 2U^2 L_{\mathrm{ph}\ AB}^{xx'x'x} \tag{2.28}$$

stems from Eq. (2.18). The factor 2 occurs because there are two possibilities to assign the indices x and x' to the general indices 1,2,3,4. The edge states of opposite edges are restricted to different sublattices, so that the 'direct' two-particle terms from Eq. (2.11) vanish. Thus, there are only the bulk-mediated SW couplings in H_{le}. It should be noted that $\chi_{xx'}$ can be interpreted as the bulk-mediated RKKY interaction between the spins of the electrons in the two Wannier states. The Hamiltonian of the high energy subspace can be well approximated by the effective Hubbard interaction Eq. (2.9):

$$H_{\mathrm{he}}^{\mathrm{inter}} = U\Gamma_{xxxx}\mathbf{1}^{2\times 2} \ ,$$

where one should remember that Γ_{xxxx} is independent of the Wannier position x for zigzag ribbons.

The block connecting low- and high-energy sector reads

$$H_{\mathrm{hop}} = (t_{xx'}^{*} + \eta_{xx'}) \begin{pmatrix} 1 & 1 \\ -1 & -1 \end{pmatrix} \ ,$$

where $\eta_{xx'} = 2U^2 \left(B^{xx'} + T^{xx'} \right)$ is the bulk-mediated one-particle SW hopping Eq. (2.21) and $t_{xx'}^{*}$ is the direct hopping of the edge states Eq. (2.12). Please note that $t_{xx'}^{*}$ is an effective hopping and a different parameter than the original Hubbard hopping t.

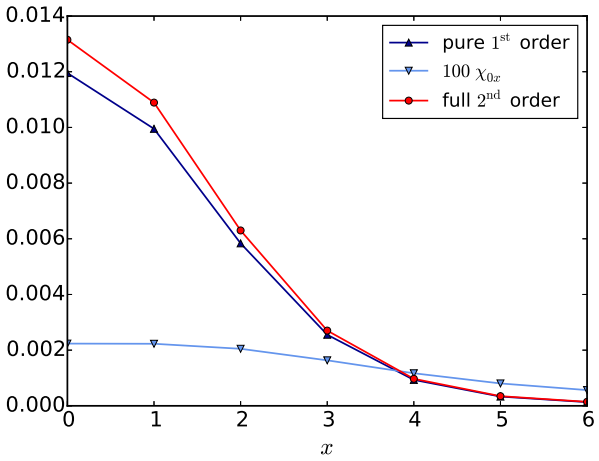

Figure 2.6.: The different parts of the inter-edge coupling as a function of Wannier index x along the ribbon. The ribbon dimensions are $N = 104$, $M = 12$ and the original Hamiltonian parameters $t = U = 1$. The major contribution to the second order correction steps from $\eta_{xx'}$, whereas the direct correction $\chi_{xx'}$ has to scaled for better visibility.

Since $t^*_{xx'}, \eta_{xx'} \ll \Gamma_{xxxx} U$ for reasonably wide ribbons, it is justified to apply perturbation theory as described above, which results (up to a constant) in a Heisenberg inter-edge spin coupling

$$H^{\text{inter}}_{\text{spin}} = \sum_{x,x'} \underbrace{\left\{ 2\chi_{xx'} + \frac{4\left(t^*_{xx'} + \eta_{xx'}\right)^2}{U\Gamma_{xxxx}} \right\}}_{=J^{\text{AF}}_{xx'}} \boldsymbol{S}_{xA} \boldsymbol{S}_{x'B}. \tag{2.29}$$

$\boldsymbol{S}_{xs} = (S^x_{xs}, S^y_{xs}, S^z_{xs})$ is the vector of Pauli matrices acting on the spin of the electron in the Wannier state at x, s. If the bulk states had been neglected, $\chi_{xx'}$ and $\eta_{xx'}$ would be absent. In this case we recover the inter-edge coupling from Eq. (2.14).

Fig. 2.6 provides an overview of the different contributions to $J^{\text{AF}}_{xx'}$ as a function of distance $|x - x'|$ between the Wannier states. Clearly, the direct coupling $\sim \left(t^*_{xx'}\right)^2 / U\Gamma_{xxxx}$ of the edges states is much larger than the bulk-state corrections, which again justifies the use of perturbation theory. Of the bulk state corrections, the bulk-mediated hopping $\eta_{xx'}$ is most relevant. The RKKY-like $\chi_{xx'}$ is only of minor importance.

Momentum range of the edge states However, $\chi_{xx'}$ displays another unique feature: Fig. 2.7 shows χ_{xx} between opposite sites Ax and Bx as a function of k_{lim}. This quantity is the limiting momentum, at which the lowest two bands in the bandstructure are separated in the edge states—with $k_0^{\text{edge}} \in (-k_{\text{lim}}, k_{\text{lim}})$—and the bulk states, whose momentum has a larger absolute value. A usual choice is $k_{\text{lim}} = \frac{\pi}{3}$, however this is not fully justified only by visual inspection of the band structure Fig. 2.2. The RKKY like interaction χ_{xx} now has a minimum near $k_{\text{lim}} = \frac{\pi}{3}$ and justifies this often used choice. It is plausible that the interaction strength

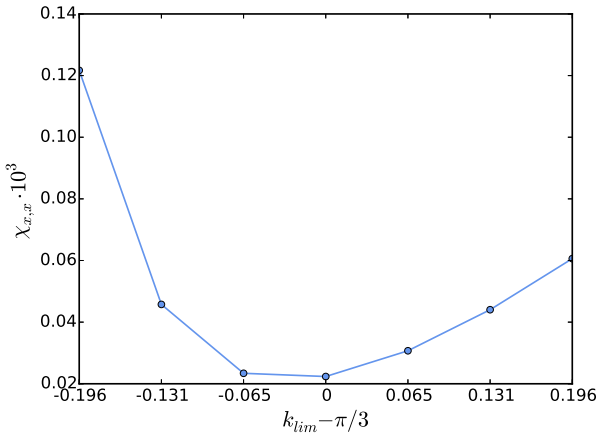

Figure 2.7.: The direct second-order correction term between opposite edges, which is also interpreted as an RKKY interaction, exhibits a minimum around $k_{\mathrm{lim}} = \frac{\pi}{3}$.The momentum has been changed in steps of $\delta(k) = \frac{\pi}{48}$. Ribbons parameters are again $N = 104,\ M = 12$, and $U = t = 1$.

grows when we include more bulk momenta into the edge states and therewith increase the number of states that contribute to this interaction. However, the coupling grows even stronger when part of the edge momenta are omitted and counted as bulk states. This is because these excess bulk states then also serve as mediating states.

The corrections in $\eta_{xx'}$ do not have any special features as functions of cutoff momentum. Their values increase monotonically when the momentum limit increases, because this leads to a higher degree of delocalization of the edge wavefunctions and thereby to a larger overlap and hopping.

Dependence on the ribbon dimensions Finally, we analyze the dependence of the inter-edge coupling on the width M of the ribbon. It is known[44, 45] that the RKKY coupling in graphene $H_{\mathrm{RKKY}} = J_{ij}\boldsymbol{S}_i \cdot \boldsymbol{S}_j$ decreases with the third power of distance

$$J_{ij} \propto \frac{1}{|\vec{x}_i - \vec{x}_j|^3} \ .$$

In Fig. 2.8, the first and second order of the correlation between opposite states are plotted as a function of the estimated power law. Both results fall off linearly, indicating that the estimated behavior is indeed met.

Consequently, the whole coupling between opposite edges will soon become extremely small for very broad ribbons. As will be also described in the next chapter (compare Sec. (3.4)), the antiferromagnetic interactions do not have a significant influence on the magnetic behavior of extremely broad ribbons ($M \gtrsim 20$) at all. Therefore, one can for any ribbon width safely take the first order results as a good approximations and will not necessarily need to include second order in $J^{\mathrm{AF}}_{(2)}$. Likewise, the behavior for constant width M, but growing length N must be checked. In Fig. 2.8, the relative error of the pure first order inter-edge terms with respect to the results up

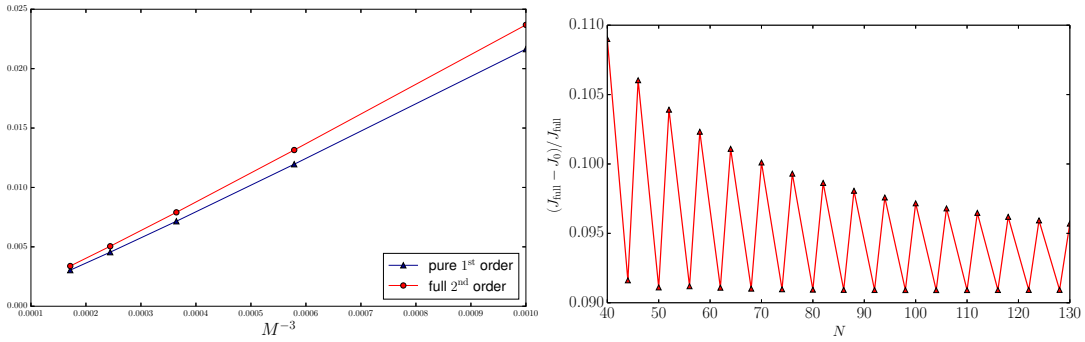

Figure 2.8.: Left: "When the ribbon width M is increased, the zeroth order contribution J_0 as well as the full term including second order effects decrease as M^{-3}. This is in accordance with the RKKY interaction in graphene. The ribbon length is $N = 104$. Right: The relative error pf the pure first order calculation $\left(J^{(1)}_{\text{AFM}} - J^{(2)}_{\text{AFM}}\right)/J^{(2)}_{\text{AFM}}$ decreases for increasing ribbon length. The zigzag features stem from the distributions of the k values in the center third of the Brillouin zone and are a finite size effect. The width is $M = 12$.
For both plots $k_{\text{lim}} = \pi/3$ and $U = t = 1$.

to second order is seen as a function of ribbon length N. For a fixed value of k_{lim} the results differ depending on the value of N mod 3, which is due to the varying choice of the discrete momenta in the Brillouin zone and vanishes in the limit of very large N. The important observation, however, is that the overall relative error becomes smaller as N is increased. Consequently, we can conclude for all system sizes that the first order calculation from Sec. 2.1.2 constitutes a good approximation of the antiferromagnetic coupling.

2.3.2. Intra-edge coupling

For the interaction between two states on the same edge—and thus on the same sublattice—first order spin couplings of the form $g_{xx'} = \Gamma^{eeee}_{xxx'x'}$ appear in the low-energy part of Eq. (2.25), which reads

$$H^{\text{intra}}_{\text{le}} = (g_{xx'} - \kappa_{xx'}) \begin{array}{c} \\ |\uparrow\downarrow\rangle \\ |\downarrow\uparrow\rangle \end{array} \begin{array}{c} \begin{array}{cc} |\uparrow\downarrow\rangle & |\downarrow\uparrow\rangle \end{array} \\ \begin{pmatrix} 1 & -1 \\ -1 & 1 \end{pmatrix} \end{array}, \tag{2.30}$$

with

$$\kappa_{xx'} = \chi_{xx'} - \theta_{xx'} + \tilde{\chi}_{xx'} - \tilde{\theta}_{xx'}, \tag{2.31}$$

where $\chi_{xx'}$ was defined in Eq. (2.28), and

$$\theta_{xx'} = 2U^2 L^{xxx'x'}_{\text{ph s,s}} = 2U^2 L^{xx'x'x}_{\text{pp s,s}} \tag{2.32}$$

and the parameters with a tilde contain the analogous contribution of the M loops

$$\tilde{\chi}_{xx'} = 2U^2 M^{xx'x'x}_{\text{ph}} = 2U^2 M^{xx'xx'}_{\text{pp}} \tag{2.33}$$

$$\tilde{\theta}_{xx'} = 2U^2 M^{xxx'x'}_{\text{ph}} = 2U^2 M^{xx'x'x}_{\text{pp}}. \tag{2.34}$$

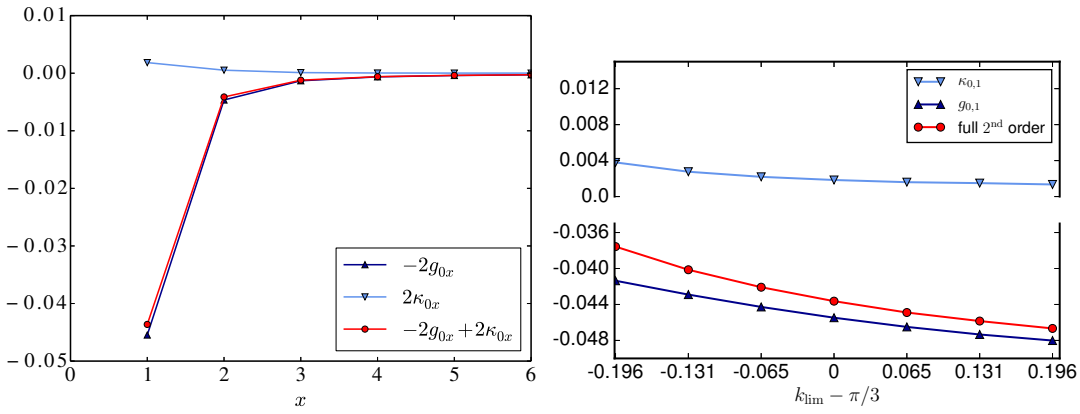

Figure 2.9.: Left: The intra-edge coupling as a function of distance along the ribbon, with $k_{\mathrm{lim}} = \pi/3$. The pure first order term (dark blue, $\triangle$) is ferromagnetic, as well as the full second order correlation (red, $\circ$). The latter is weaker due to the ferromagnetic correction term κ (Eq. (2.31)) (light blue, $\triangledown$). The correction is about one order of magnitude smaller than the first order. Right: The same coupling contributions for nearest neighbors each, as a function of momentum limit. The second order only weakly depends on the choice of k_{lim}. In the combination, we see no distinctive feature for $k_{\mathrm{lim}} = \pi/3$. Both plots are for dimensions $N = 200$ $M = 12$ and the Hamiltonian parameters are $U = t = 1$.

The Hamiltonian of the high energy subspace could again be well approximated by $H_{\mathrm{he}}^{\mathrm{intra}} = U\Gamma^{xxxx}\,\mathbf{1}^{2\times 2}$, but since there is no intra-edge hopping neither in first nor in second order, there is no need to perform further perturbation theory. Thus, the intra-edge spin coupling Hamiltonian including second order bulk corrections reads

$$H^{\mathrm{intra}} = \sum_{\substack{x,x' \\ x\neq x'}} -2\left(g_{xx'} - \kappa_{xx'}\right) \boldsymbol{S}_x \cdot \boldsymbol{S}_{x'} \tag{2.35}$$

In first order, we have a direct ferromagnetic coupling. Due to the structure of $\kappa_{xx'}$ with positive and negative signs, the effects of different interactions partially reduce each other. The term $\chi_{xx'}$, which represents a bulk-states-mediated RKKY coupling, is ferromagnetic, so $\chi_{xx'} < 0$, but the overall sum gives $\kappa_{xx'} > 0$, so that the full second order coupling weakens the direct ferromagnetic coupling. Figure 2.9 shows the different contributions as a function of the Wannier index x along the ribbon. One sees a rather small reduction of the ferromagnetic coupling when including the second order terms.

The dependence of the different order terms on the choice of the momentum limit is plotted in Fig. 2.9 on the right: The characteristics of both the first and the second order term are similar, and the overall dependence of the full term on the momentum limit is only weak. Figure 2.10 shows the dependence of $\tilde{\chi}_{x,x+1}$ on the momentum limit; this is the only intra-edge interaction that exhibits a feature near $k_{\mathrm{lim}} = \frac{\pi}{3}$. Even though it only yields a small absolute contribution compared to the other summands in $\kappa_{xx'}$, this dependence still gives an estimator for the correct

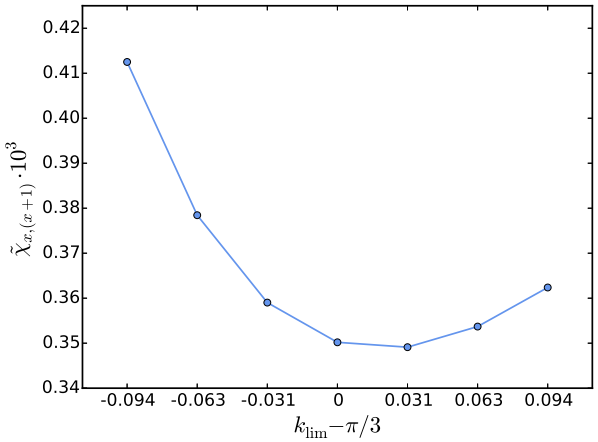

Figure 2.10.: The coupling $\tilde{\chi}_{x,x+1}$ (compare Eq. (2.33) above) between direct neighbors as is depends on the momentum limit k_{lim}, with step size $\delta(k_{\mathrm{lim}}) = \frac{\pi}{100}$. This is the only summand from Eq. (2.35) that has a specific feature around $k_{\mathrm{lim}} = \frac{\pi}{3}$. Since the other contributions however do not cancel with this effect, it can still serve as indicator for the correct choice of momentum limit. The other parameters are $N = 200$, $M = 12$ and $U = t = 1$.

choice of k_{lim}. The other contributions to $\kappa_{xx'}$ depend monotonically on the momentum limit, so that there cannot occur any compensation effects.

Bulk correction for wide ribbons In contrast to the above cases, the second order terms become numerically more important for the intra-edge coupling at growing ribbon width M. This is due to the fact that with increasing M the number of bulk bands increases, and therefore more bands are available for intermediate states in the M- processes from Eq. (2.19) and Eq. (2.20). In Fig. 2.11 one sees the relative error $\left(J^{\mathrm{FM}}_{(1)} - J^{\mathrm{FM}}_{(2)}\right)/J^{\mathrm{FM}}_{(2)}$ of the pure first order calculation as a function of growing ribbon width (red line), for the interaction between directly adjacent sites. This can be fitted well to the function (blue line)

$$f(M) = a + b \cdot M^{-1/3} \qquad \text{with } a \approx 0.05$$

The constant offset $a \approx 0.05$ is therefore expected to represent the maximal relative error for extremely broad ribbons. We conclude that the error stays in an acceptable range.

2.4. Next-nearest-neighbor hopping

Including a hopping $\propto t'$ to the second nearest neighbor makes the tight-binding model for graphene more realistic. However, it breaks the electron-hole symmetry, it shifts the Fermi surface to $\varepsilon_F = 3t'$, and it bends down the edge energy bands out of their before flat shape. Fig. 2.12 shows the band structure for a hopping $t'/t = 0.1$ in the free model $U = 0$. The energy has already been shifted back so that $\varepsilon_F = 0$.

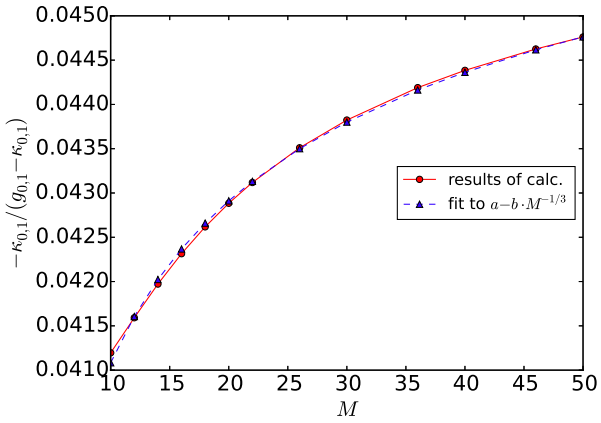

Figure 2.11.: Concerning the intra-edge coupling, the second order correction actually becomes more important for growing ribbons width. The relative error of the pure first order approximation behaves as $\sim M^{1/3}$. The plot shows the relative error for $N = 104$, $k_{\text{lim}} = \pi/3$ and $U = t = 1$. The fit results are $a \approx 0.0499$, $b \approx -0.0191$, so we assume the error to stay within the well acceptable range of $\delta_{\text{max}} \sim 5\%$.

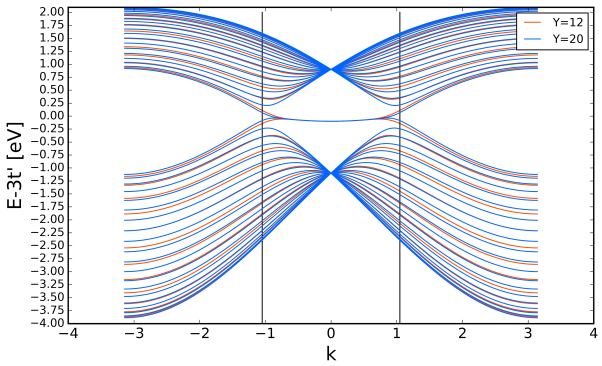

Figure 2.12.: The bandstructure of a graphene ribbon in a Hubbard model plus next-nearest neighbor hopping $t' = 0.1t$. The colors indicate different ribbon widths $W = 10$ unit cells and $W = 12$ unit cells, respectively; the length is $X = 602$ unit cells each. The bandstructure is shifted about a constant energy to bring the edge states back to charge neutrality.

One can see that at this strength of t' coupling, the edge bands are still well separated form the bulk bands. For further comparison, we write the contribution of next-nearest neighbor hopping to the Hamiltonian in the previously used basis. The next-nearest neighbor hopping couples states from the same sublattice. The hopping in momentum space reads:

$$\begin{aligned}
H_1 &= -t' \sum_{n=1}^{N,\,\mathrm{pbc}} \sum_{m=1}^{M,\mathrm{pbc}} \sum_{S\in\{A,B\}} c^\dagger_{nmS} \left\{ c_{(n-1)(m+1)S} + c_{n(m+1)S} + c_{(n+1)mS} + c_{(n+1)(m-1)S} + c_{n(m-1)S} + c_{(n-1)mS} \right\} \\
&= -t' \frac{1}{K} \sum_n \sum_m \sum_S \sum_{p,q} e^{-ikm} c^\dagger_{nkS} \Big\{ e^{iq(m+1)} c_{(n-1)qS} + e^{iq(m+1)} c_{nqS} + e^{iqm} c_{(n+1)qS} \\
&\quad + e^{iq(m-1)} c_{(n+1)qS} + e^{iq(m-1)} c_{nqS} + e^{iqm} c_{(n-1)qS} \Big\} \\
&= -t' \frac{M}{K} \sum_n \sum_S \sum_{k,q} \delta_{k,q} c^\dagger_{nkS} \left\{ e^{iq} c_{(n-1)qS} + e^{iq} c_{nqS} + c_{(n+1)qS} + e^{-iq} c_{(n+1)qS} + e^{-iq} c_{nqS} + c_{(n-1)qS} \right\} \\
&= -t' \frac{M}{K} \sum_n \sum_S \sum_k c^\dagger_{nkS} \left\{ \left(e^{ik}+1\right) c_{(n-1)qS} + 2\cos(k)\, c_{nqS} + \left(e^{-ik}+1\right) c_{(n+1)qS} \right\}
\end{aligned}$$

We use a tilted y-direction to get real entries in the free Hamiltonian: $c^{(\dagger)}_{nkS,\,\mathrm{new}} = i^n \cdot e^{(-)ikn/2} \cdot c_{nkS,\,\mathrm{old}}$, this gives

$$\begin{aligned}
H_1 &= -t' \sum_n \sum_k \sum_S c^\dagger_{nkS} \left\{ \left(e^{ik}+1\right) e^{-ik/2} c_{(n-1)kS} + 2\cos(k)\, c_{nkS} + \left(e^{-ik}+1\right) e^{ik/2} c_{(n+1)kA} \right\} \\
&\quad - t' \sum_{n=1}^{N,\,\mathrm{PBC}} \sum_k \sum_S c^\dagger_{nkS} \left\{ 2\cos\left(\frac{k}{2}\right) c_{(n-1)kS} + 2\cos(k)\, c_{nkS} + 2\cos\left(\frac{k}{2}\right) c_{(n+1)kS} \right\}
\end{aligned}$$

To have a symmetric band structure, in the end a shift $k \mapsto k + \pi$ is introduced, which finally yields:

$$H_1 = -t' \sum_{n=1}^{N,\,\mathrm{PBC}} \sum_k \sum_S c^\dagger_{nkS} \left\{ 2\sin\left(\frac{k}{2}\right) c_{(n-1)kS} - 2\cos(k)\, c_{nkS} + 2\sin\left(\frac{k}{2}\right) c_{(n+1)kS} \right\}$$

To make sure that small overlaps between edge and bulk states in the effective model are still a good starting point for perturbation theory, we look at the absolute value squared of an edge state as a function of ribbon site in y-direction. The logarithmic plot Fig. 2.13 displays that the edge state decays exponentially into the bulk of the ribbon, so the main prerequisites for the applicability of the effective model are still fulfilled, at least for the small hopping value $t' = 0.1t$, which should be a realistic estimate for actual graphene, compare Ref. [9]. However, one has to take care of the shift in the Fermi energy and make sure that the edge states as well as the whole system are still half filled. If we went away from the point of half filling in bulk graphene, we would get RKKY interactions between the edge states and additional bulk electrons or holes [44, 45]. These could be strong enough to render our approximations invalid. Karimi and Affleck [32] have shown that without an additional potential the edge states are stable up to a value of

$$t'_{\mathrm{crit}} = 0.109U$$

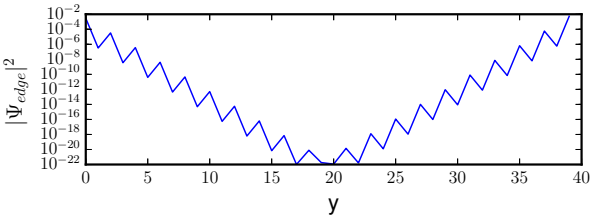

Figure 2.13.: The absolute value squared of an edge state as a function of y across the ribbon for $t'/t = 0.1,\ U = 0$ and $N = 120,\ M = 20$. The zigzag feature illustrates that the edge states do not vanish any more on one sublattice, but there is still a higher weight on the sublattice the edge belongs to.

Since we use $U = t$, the choice of $t'/t = 0.1$ is hence still in the regime where the effective model is fully valid with the edge states half filled.

To keep a correct hierarchy of the orders of magnitude, the second nearest neighbor hopping terms should be included in the same order perturbation theory as the onsite repulsion. For this, we go over to the Wannier basis

$$d^\dagger_{k\nu} = \sum_{m,s} \phi_{k\nu}(m,s)\, c^\dagger_{mks} = \sum_{\tilde{m}} \phi_{k\nu}(\tilde{m}) \left(c^\dagger_{\tilde{m}kA} + c^\dagger_{\tilde{m}kB}\right) \Leftrightarrow \qquad \left(c^\dagger_{\tilde{m}kA} + c^\dagger_{\tilde{m}kB}\right) = \sum_{\nu} \phi^*_{k\nu}(\tilde{m})\, d^\dagger_{k\nu}$$

where the $\overrightarrow{\phi}_{k,\pm}$ are of the form $(..., nA, nB, n+1A, n+1B, ...)^T$ or equivalently $(..., \tilde{n}, \tilde{n}+1, \tilde{n}+2, ...)^T$. In the next step, we only take into account the direct interaction between the edge states ("zeroth order"), hence the summation of the subbands ν, μ is restricted to the positive and negative edge bands $\nu, \mu \in \{+, -\}$. Therefore, $\phi_{kA}(\tilde{n}) = 0$ for $\tilde{n}$ even and $\phi_{kB}(\tilde{n}) = 0$ for $\tilde{n}$ odd, and the basis change can be separated into the A and B sublattices. We use again the conventional notation $\phi_{k\nu}(m,s)$.

We get the following result for the A sites:

$$\begin{aligned} H_{1,A} &= -t' \sum_n \sum_k \sum_{\nu,\mu} \phi^*_{k\nu}(n,A)\, d^\dagger_{k\nu} \left\{ 2\sin\left(\frac{k}{2}\right) \phi_{k\mu}(n-1,A) - 2\cos(k)\, \phi_{k\mu}(n,A) + 2\sin\left(\frac{k}{2}\right) \phi_{k\mu}(n+1,A) \right\} d_{k\mu} \\ &= -t' \sum_{k,\nu} \Bigg\{ -2\cos(k)\, d^\dagger_{k\nu} d_{k\nu} + \sum_{n=1}^{N} \sum_{\mu} 2\sin\left(\frac{k}{2}\right) \underbrace{\left(\phi^*_{k\nu}(n,A)\, \phi_{k\mu}(n-1,A) + \phi^*_{k\nu}(n,A)\, \phi_{k\mu}(n+1,A)\right)}_{\xi_{k\mu\nu}(n,A)} d^\dagger_{k\nu} d_{k\mu} \Bigg\} \end{aligned} \tag{2.36}$$

Going over to the sublattice polarized edge basis, the first addend can be rewritten straightforwardly:

$$t' \sum_{k,\nu} -2\cos(k)\, d^\dagger_{k\nu} d_{k\nu} = -t' \sum_k -2\cos(k) \left(e^\dagger_{kA} e_{kA} + e^\dagger_{kB} e_{kB}\right)$$

For the second addend, rewriting is more complicated. Using the symmetries $\sum_n \xi_{k,\nu\mu}(n,S) = \sum_n \xi^*_{k,\nu\mu}(n,S)$ and $\sum_n \xi_{k,+-}(n,S) = \sum_n \xi_{k,-+}(n,S)$, where the latter one is valid due to the

real eigenstates of the Hamiltonian, we get for the next-nearest neighbor Hamiltonian in zeroth order:

$$H_1^{(0)} = -t' \cdot \sum_k -4\cos(k)\left(e_{kA}^\dagger e_{kA} + e_{kB}^\dagger e_{kB}\right) + \sum_k \sum_{n=1}^{N} \sum_{S\in\{A,B\}} \sin\left(\frac{k}{2}\right)\left\{2\left[\xi_{k++}+\xi_{k+-}\right](n,S)\cdot e_{kA}^\dagger e_{kA} + 2\left[\xi_{k,++}-\xi_{k+-}\right](n,S)\cdot e_{kB}^\dagger e_{kB}\right\}$$

For details compare App. A.1. Rewriting this in terms of the sublattice polarized edge states and applying some reformulations gives:

$$\begin{aligned} H_1^{(0)} &= -t' \cdot \sum_k \Bigg\{ -4\cos(k)\left(e_{kA}^\dagger e_{kA} + e_{kB}^\dagger e_{kB}\right) \\ &\quad + 2\sin\left(\frac{k}{2}\right)\cdot \sum_n \left(2\phi_{kA}(\tilde{n})\,\phi_{kA}(\tilde{n}+2)\,e_{kA}^\dagger e_{kA} + 2\phi_{kB}(\tilde{n})\,\phi_{kB}(\tilde{n}+2)\,e_{kB}^\dagger e_{kB}\right)\Bigg\} \\ &= \sum_k \left(H_1^{(0)}(k,A)\cdot e_{kA}^\dagger e_{kA} + H_1^{(0)}(k,B)\cdot e_{kB}^\dagger e_{kB}\right) \end{aligned}$$

Now we transform this back into real space using

$$H_1^{(0)}(x,x') = \frac{1}{K}\left(\sum_{|k|\le k_{\lim}} H_1^{(0)}(k,A)\,e^{-ika(x-x')}\right) e_{xA}^\dagger e_{x'A} + [A\leftrightarrow B] = t_{\text{intra}}^*\left(e_{xA}^\dagger e_{x'A} + e_{xB}^\dagger e_{x'B}\right)$$

Hence, the next-nearest neighbor interaction to zeroth order yields an additional hopping term inside the edge. Numerical calculations reveal that the hopping term has alternating sign and fulfills $t_{\text{intra}}^* \ll U^*$. It is therefore again possible to include it into the effective spin model in second order perturbation theory, which yields an effective reduction of the ferromagnetic intra-edge coupling. In Fig. 2.14 (left) one can see a comparison of the pure ferromagnetic coupling term and the reduced one which includes the next-nearest neighbor hopping contributions. To this resolution it is not possible to discern any visible difference between the two graphs, even for the nearest edge states along the ribbon.

On the right hand side, we compare the long-range behavior of the full result to the long-range behavior of the effective antiferromagnetic correction term $-\left(t_{\text{intra}}^*\right)^2/U^*$. The latter decays also with a power law, but it obviously has a higher exponent than the full term. Consequently, these correction terms will not alter the long-range behavior of the ferromagnetic coupling.

Thus we conclude that it is safe to ignore the corrections to the effective model that come from next-nearest neighbor hopping, as long as it remains below the critical value of $t' = 0.109U = 0.109t$. This should be the case in realistic graphene nanoribbons.

For curiosity we also tested the influence of the next-nearest neighbor hopping onto the effective model outcome when included directly into the Hamiltonian and treated in the same order as the direct hopping t'. Such an approach could be useful for $t' \gg U^* = U\Gamma^{xxxx}$, so in particular for the case of a small onsite repulsion U. With such a calculation, both the intra- and interleg coupling are changed due to the second nearest neighbor hopping. As presented in Fig.2.15, the

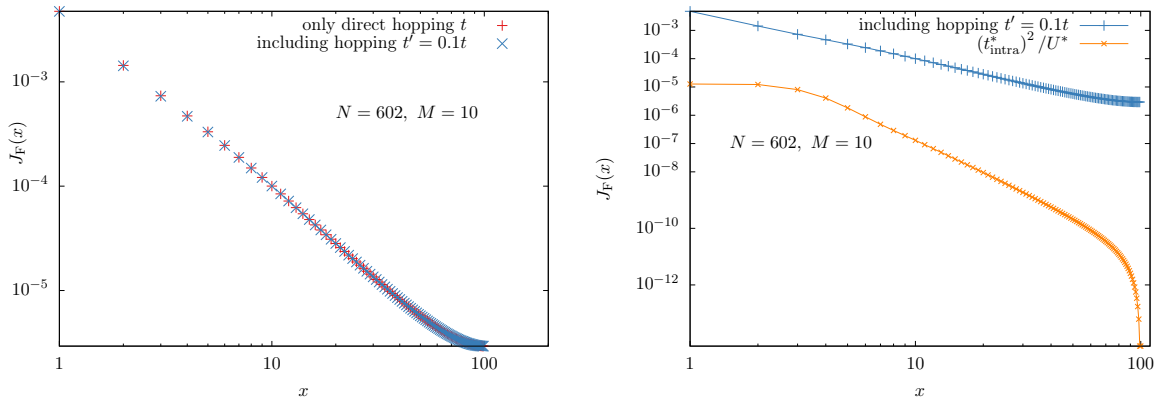

Figure 2.14.: The ferromagnetic coupling of a GNR with 10×602 unit cells with and without next-nearest neighbor hopping terms as a function of distance along the ribbon. The terms $\propto t'$ are included into the perturbation part of the effective model and then treated by conventional second-order perturbation theory when going over to the spin basis. On the left, the full result including $t' = 0.1t$ (blue) is compare to the one for $t' = 0$ (red), while on the right, the full result is plotted together with the difference between both.

intraedge coupling in this case gets a slightly "waved" feature that stems from the next-nearest hopping terms. Especially the long-range tail seems to be affected by this behavior, while, however, the valleys of the curves still follow the $1/x^2$ decay. We get qualitatively similar results for $W = 8, 10$ unit cells.

For the inter-edge hopping, the next-nearest neighbor terms, when included directly in the unperturbed part, enhance the coupling strength on the short-range opposite sites, compare Fig. 2.16. This effect occurs equally for $W = 10$ and $W = 12$. However, the long-range behavior is not significantly altered by this.

To summarize, the most significant effect of including the next-nearest neighbor terms $t' = 0.1t$ into the unperturbed part of the Hamiltonian are the introduction of a wavy behavior for the intraedge couplings and the enhancement of the short-range interedge interactions.

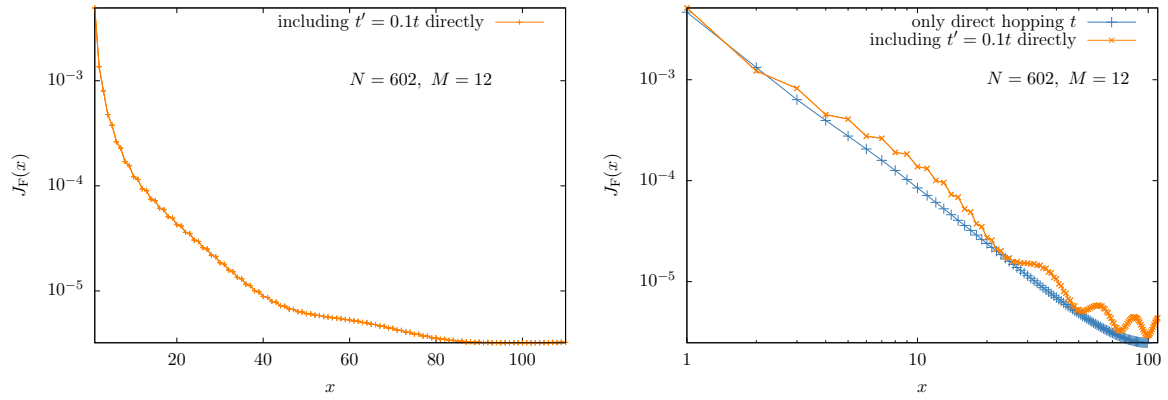

Figure 2.15.: The intraedge interaction of a ribbon with 12×602 unit cells, when $t' = 0.1t$ is included directly into the unperturbed Hamiltonian. The left plot features linear-logarithmic axes, while the right one ist a log-log plot.

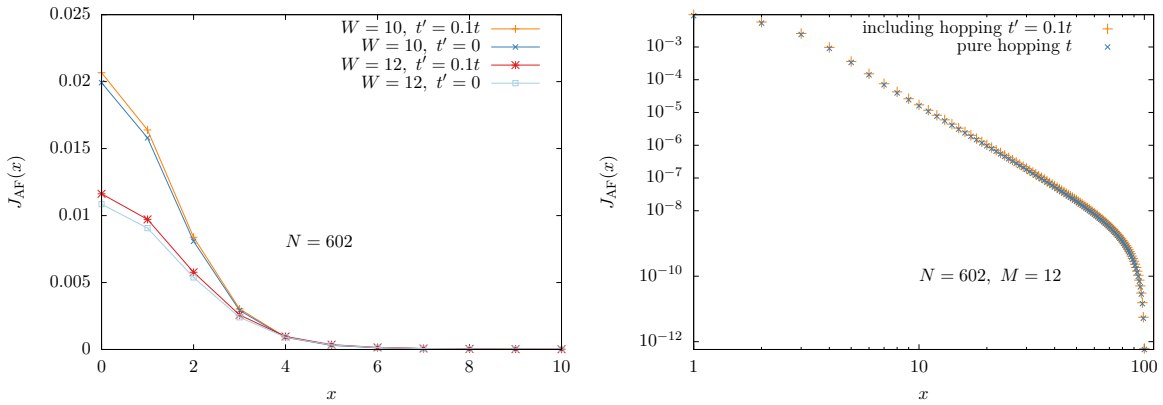

Figure 2.16.: Left: The interedge couplings of ribbons with 10×602 and 12×602 unit cells, respectively, comparing the case with and without next nearest neighbor hopping. Right: The long-range behavior for 12×602 unit cells in a log log plot.

2.5. Phosphorene

Motivated by the paper by Yang et al. [46] on the edge states in a single layer of black phosphorus, we adapt the effective model to this system, which is also known as phosphorene. The material has a honeycomb structure like graphene, but the distances between the atoms are different in the two spatial directions. Seen from the side, phosphorene has a corrugated structure (compare e.g. Ref. [47] Fig. 3) with a thickness of about 5 Å (compare Ref. [48]), so that the further apart tight-binding hopping parameters cannot be understood by only looking at the two-dimensional structure. The largest hopping values again belong to the nearest-neighbor hopping, with the peculiarity that one of the values is positive. We will use the anisotropic nearest neighbors here with the values from Ref. [46]:

$$t_1 = -1.22 \text{ eV} \qquad t_2 = 3.665 \text{ eV} \tag{2.37}$$

These tight-binding parameters have originally been calculated in Ref. [48] using an ab initio method with quasiparticle *GW* approximations. These two hoppings dominate the behavior of the tight-binding model, since the next largest quantity is a fourth nearest neighbor hopping with the amplitude of only $t_3 = -0.205$ and therewith $|t_3| \ll |t_1|$.

The different layers in bulk and multi-layer black phosphorus are coupled by van der Vaals forces, as it is the case in graphite. Monolayer phosphorene is held together by covalent bindings of the sp^3 hybridized orbitals, but in contrast to graphene, there are no free electrons[46], so the material exhibits a significant band gap. The bulk material has a band gap of about 0.3 eV, but for single layer this is expected[48, 49] to be in the range of ~ 1.5 eV. This value lies between the one for freestanding graphene and two-dimensional semi-conducting dichalcogenides[49]. Phosphorene is also classified as a semiconductor[50]. The carrier mobility in a monolayer of black phosphorus is estimated[50] to be up to $\sim 1000 \frac{\text{cm}^2}{Vs}$. However, the electronic properties of phosphorene are highly anisotropic[47] due to its puckered structure. Since it has been shown[51]that in graphene dots, strain can strongly enhance the magnetization, it appears interesting to study the edge magnetism in a phosphorene nanoribbon (PNR). The intrinsic anisotropy in phosphorene is larger than what can be achieved from strain in graphene[46].

Few-layer thick flakes of black phosphorus were synthesized in the laboratory 2014 by Li et al. (compare Ref. [50]) and they were used as field-effect transistors. To produce these layers from bulk black phosphorus, the group again used a method based on scotch tape, and deposited the flakes on a silicon wafer covered with a layer of silicon dioxide[50]. Castellanos-Gomez et al. have modified the classical technique, compare Ref. [52]: They used an intermediate viscoelastic surface of a poly-dimethilsiloxane based substrate to improve the yield of thin, few-layer phosphorus flakes. Following this, they examine the flakes with Raman spectroscopy and transmission electron microscopy.

Concerning the edge states of a nanoribbon, the most fundamental difference between the band structures of graphene and phosphorene is that the latter is fully gapped, but the edge bands are much flatter, and with the exception of extremely narrow ribbons, they extend at the Fermi surface over the whole Brillouin zone, not only one third of it, compare Fig. 2.18.

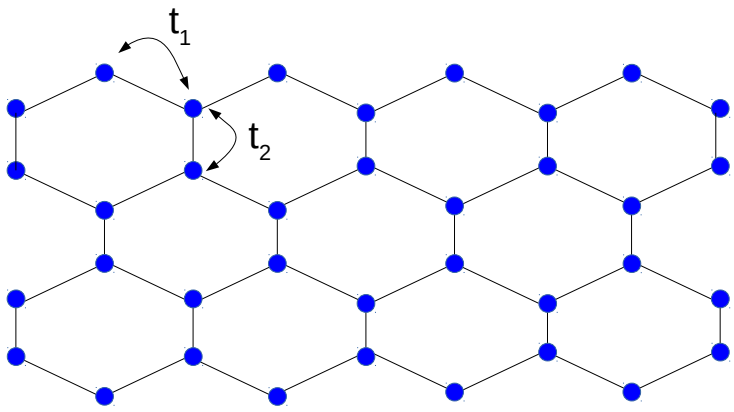

Figure 2.17.: The squeezed honeycomb structure in phosphorene as seen from the top. The hopping t_2 is highly unfavorable because of the puckered structure of the material: Subsequent zigzag segments lie in different layers in z-direction. For a three dimensional view of the material compare Ref. [48], Fig. 4 therein.

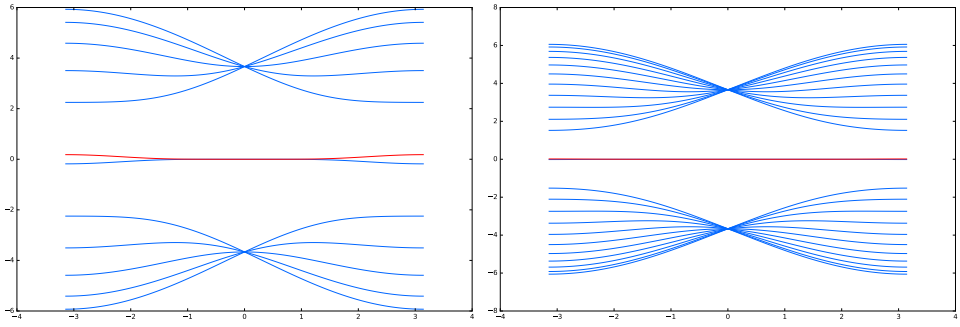

Figure 2.18.: The bandstructure of a phosphorene nanoribbon in nearest-neighbor tight binding approximation with $U = 0$ for 6×102 unit cells (left) and 12×102 unit cells (right), respectively. One of the edge states is marked in red. As for graphene, the Brillouin zone was shifted to $[-\pi, \pi]$ as before.

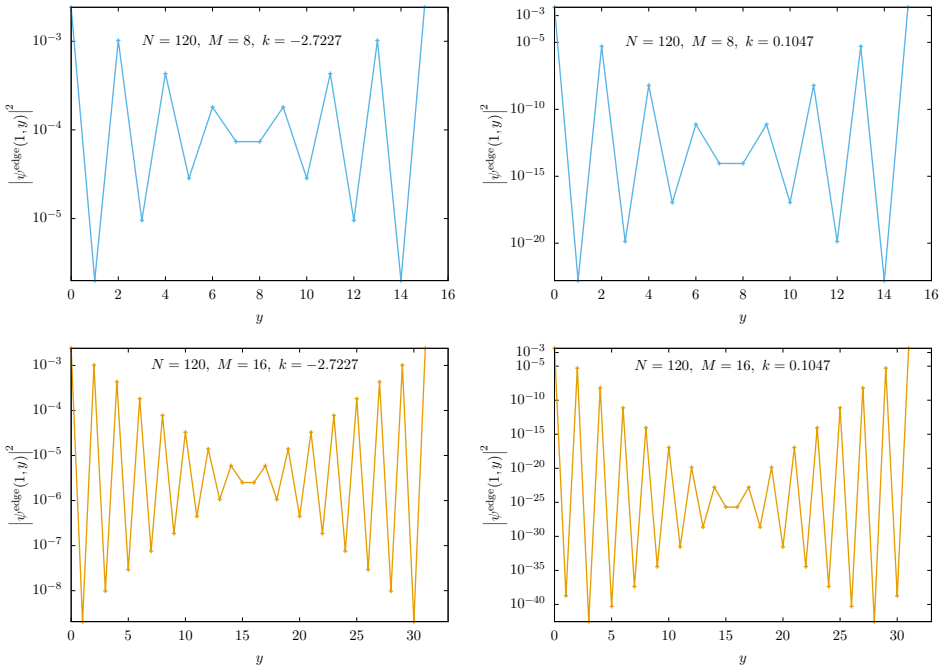

Figure 2.19.: The amplitude squared of the edge states with $k = -2.7227$ (left) and $k = 0.1047$ (right), respectively, as a function of y across the ribbon for $U = 0$ and $N = 120$ in phosphorene. The upper row has $M = 8$, the bottom row $M = 16$. According to the zigzag feature the edge states do not vanish any more on one sublattice, but there is still a significantly higher weight on one sublattice, especially near the edges. Both edge states decay exponentially into the bulk, but with a different decay exponent.

As a first step, we test the edge states for narrow ribbons and different momenta k for their localization across the ribbons. Fig. 2.19 presents the amplitude of one edge state with momentum close to the boundary of the Brillouin zone (left), and one edge state with a k-value from the center (right) as a function of y coordinate for ribbon width $M = 10$. It is easily visible that the edge states are not fully localized on one sublattice in this system, but still strongly prefer one. For the momentum in the center, the decay is otherwise similar to a graphene edge state. For the larger absolute momentum value, the decay of the amplitude into the ribbon is much weaker, but it is still of exponential form. Together with the fact that there is a significant gap between the edge and bulk states also outside the center third in the band structure, this suffices to conclude that edge states similar to the ones in graphene live on the whole Brillouin zone in phosphorene.

Hence, we can further utilize all calculation steps used in the first order edge states calculation for graphene, compare Sec. 2.1.2, setting the momentum "limit" to $k_{\text{lim}} = \pi$ and adjusting the hopping strengths.

Ref. [46] investigates the edge magnetism in narrow nanoribbons of phosphorene with determinant quantum Monte Carlo techniques, taking into account the hopping parameters up to

and including t_5. They stay in the original lattice basis and define a row magnetic structure factor $M = \frac{1}{L^2} \sum_{i,j \in \text{ row}} \langle \boldsymbol{S}_i \cdot \boldsymbol{S}_j \rangle$ with the usual onsite spin operators $\boldsymbol{S}_i$ and an edge magnetic susceptibility that is the same as the usual definition we will use later on (compare Eq. (3.23)

$$\chi_{\text{leg}} = \sum_{i,j \in \text{edge}} \int_0^{1/T} \langle S_{i\mu}(\tau) S_{j\mu}(0) \rangle \quad \mu \in \{A, B\}$$

with the sole difference that their sites i, j are the original lattice sites. Yang et al. then find strong ferromagnetic correlations along the edges and a non-vanishing edge magnetization for finite temperatures, with T_C even as high as room temperature. They fit the $\chi_{\text{leg}}^{-1}(T)$ behavior to the Curie-Weiss law $\chi^{-1} = (T - T_c)/A$ and deduce the critical temperature as the intercept with the T- axis (compare Fig. 2 in Ref. [46]). For undoped phosphorene, they find critical temperatures on the order of $\sim 10^{-2}$eV, which grow as the onsite repulsion U is increased and for $U = 2.0$eV reach ~ 0.032eV, corresponding to ~ 320 K. For details compare Ref. [46].

Our theoretical considerations and numerical findings also support the fact that ferromagnetic order is enhanced in phosphorene compared to the isotropic honeycomb lattice. Fig.2.20 (right) presents the effective model results for the antiferromagnetic couplings in a phosphorene nanoribbon compared to a GNR of the same dimensions. Contrary to what one might expect, the antiferromagnetic coupling is significantly weakened in phosphorene, although the spacial distance between the zigzag edges is reduced. The main reason for this is the puckered structure of phosphorene that causes the hopping t_2 to have a positive value, reflecting the height difference between each two involved sites. Because the edge bands fill the whole Brillouin zone, phosphorene—contrary to graphene—does not to have a portion of edge states with bent bands in the relevant momentum range. Going back to the band structure of graphene Fig. 2.2, the red colored parts of the bands exhibit a splitting and bending behavior already for $|k| < \pi/3$, which is particularly pronounced in narrow ribbons and originates in the hybridization of the two edge modes. This portion of the bands—and basically the effect of hybridization—much enhances the effective hopping t^* in Eq. (2.12) and Eq. (2.7). With this part missing in the anisotropic lattice, the zero modes are much more localized in real space, and the effective hopping is reduced, which leads to a much smaller antiferromagnetic coupling for the same width, as measured by unit cells. Moreover, one sees that the long-range behavior of phosphorene is less affected by finite size effects, but the short-range correlations behave much more irregularly, before transitioning into the $1/x^4$ decay. Probably the reason for such irregularities are the distorted shape of the material and the different hopping strengths.

The results from Ref. [46] are consistent with ours relating to the enhancement of ferromagnetic correlations for larger onsite repulsion U, compare Eqs. (2.13) and (2.14).

However, our results do not support the picture of a stark qualitative difference between GNRs and PRNs considering the edge magnetism. We, too, would expect a non-vanishing edge magnetization for finite temperature and finite ribbon length. In the thermodynamic limit, however, we do not expect to find a finite critical temperature $T_{\text{crit}} > 0$ for the formation of ferromagnetic order in phosphorene, because the ferromagnetic couplings still decay $J_{\text{F}} \propto x^{-2}$, as shown in

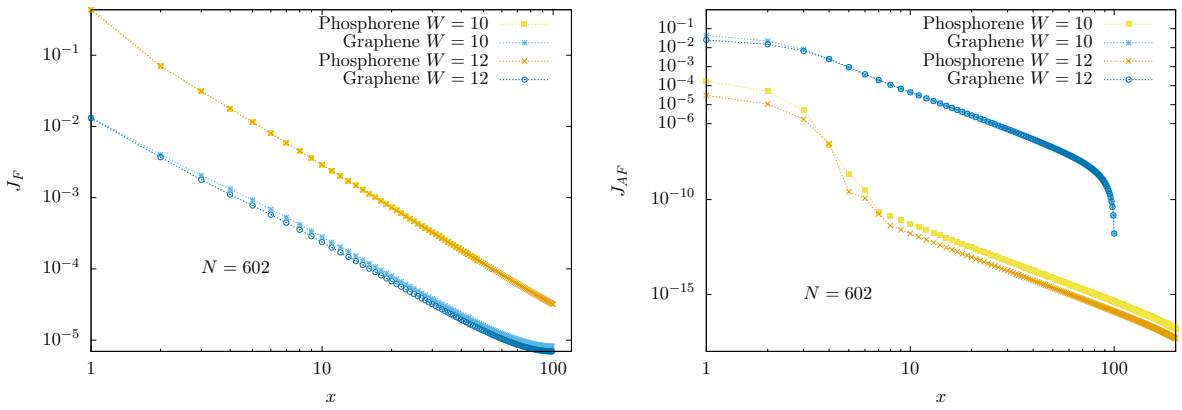

Figure 2.20.: The intraleg (left) and interleg couplings for graphene and phosphorene at two different ribbons widths. The Hubbard parameters for phosphorene are $t_1 = -1.22\text{eV}, t_2 = 3.665\text{eV}$ and $U = 3.0\text{eV}$. The parameters for graphene are $-t = U = 2.8\text{eV}$.

Fig. 2.21 (left). The decay exponent for the antiferromagnetic coupling is also the same as in graphene nanoribbons, namely $J_{\text{AF}} \propto x^{-4}$.

The investigation of the long-range coupling behavior and its influence on the thermodynamic limit properties of graphene nanoribbons will be the key goal of the following chapter.

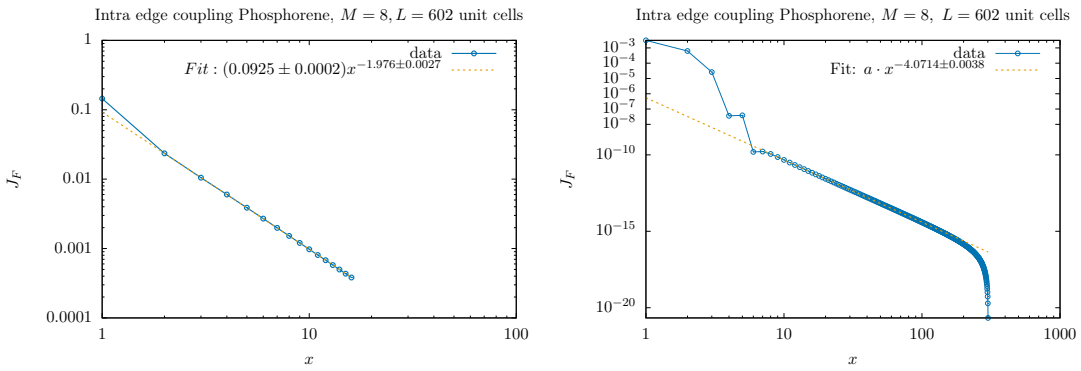

Figure 2.21.: The ferromagnetic correlations (left) are quantitatively enhanced and the antiferromagnetic ones (right) are reduced in phosphorene as compared to graphene. However, the decay exponents remain essentially unaltered. The factor in the right plot is $a \approx 5 \cdot 10^{-7}$.

3. QMC analysis of spin-ladder models with long-range interactions

3.1. The Stochastic Series Expansion

3.1.1. Fundamentals and sign problem

General idea Monte Carlo simulations in general are an important numerical tool to analyze the behavior of a variety of physical systems, equally in classical and quantum settings, in equilibrium and non-equilibrium. The special type of Monte Carlo technique that we will use is tailored for a quantum spin system at finite temperatures in equilibrium. In principle, any physical system can be simulated by Monte Carlo methods[53]; however, the performance is extremely limited in cases where the infamous sign problem occurs. We will discuss this below and explain why it does not occur for the systems we are interested in here.

The basic idea behind the technique is to statistically sample over all possible configurations of a many-body system, weighted according to the statistical probabilities. Then expectation values can be calculated in the form of[53][54] $\langle A \rangle = \frac{1}{N} \sum_{n=1}^{N} A_n$, where each n represents one many-body configuration obtained in the course of the Monte Carlo sampling. In total N such steps are performed.

The set of all possible configurations is called the configuration space Ω of the system. A sampling usually starts at an arbitrary configuration $\in \Omega$ and then proceeds to the following steps via a specially tailored update scheme that represents a stochastic process. This scheme must fulfill some prerequisites:

First, completeness and ergodicity have to be granted: The transition probabilities should be chosen such that from any starting point in Ω all other configurations can be reached within a finite number of steps, so that the process samples over the whole configuration space. The second requirement is that the process should preserve the stochastic probabilities given by the distribution function. This means that detailed balance must be preserved, i.e., the transition probabilities P from one configuration C to another one C' depend on the weights W of the configurations as[54]:

$$W(C) \cdot P\left(C \to C'\right) = W\left(C'\right) \cdot P\left(C' \to C\right)$$

The probabilities to go over to a next configuration hence only depend on the current configuration and not on the earlier states the system has passed through before in the process. A sequence of states that fulfills this condition it called a “Markov chain”, the update procedure called a “Markov process”.

For finite temperature physics in the canonical ensemble, the probability to find a configuration is defined by the Boltzmann distribution:

$$P(C_i) = \frac{1}{Z} e^{-\beta E(C_i)} \qquad \text{with the partition function } Z = \sum_i e^{-\beta E(C_i)} \tag{3.1}$$

where $\beta = (k_B T)^{-1}$, and k_B is the Boltzmann constant. The detailed balance condition can then be calculated to be[53]:

$$\frac{P(C_i \to C_j)}{P(C_j \to C_i)} = \exp\left(-\beta \left[E(C_j) - E(C_i)\right]\right)$$

In practice, such a condition is implemented like this: A new configuration is found according to an update scheme (see below), and if the energy of the new configuration is smaller than that of the old one, the new configuration is always accepted. If the energy of the new configuration is larger than before, a random number $r_j \in [0, 1)$ is generated. The new configuration is then accepted, if $r_j \leq \exp\left(-\beta\left(E_j - E_i\right)\right)$, otherwise the update is discarded.

World line quantum Monte Carlo A central quantity in statistical physics is the partition function $Z = \mathrm{Tr}\left(e^{-\beta \hat{H}}\right)$, which is involved in the calculation of any expectation value $\left\langle \hat{A} \right\rangle = \frac{1}{Z}\mathrm{Tr}\left(\hat{A} e^{-\beta \hat{H}}\right)$ with the inverse temperature $\beta = 1/T$ and the Hamiltonian $\hat{H}$. Since the exact spectrum of $\hat{H}$ is usually not known in quantum statistical setups, such quantities cannot be calculated right away[55].

Instead, in world line QMC methods, the problem is mapped to a classical system, for which Monte Carlo simulations are already applicable. This mapping yields an additional dimension, which is associated with the imaginary time τ. Mathematically, we perform a Taylor expansion of the exponential function in the partition function, rewriting

$$Z = \mathrm{Tr}\left(\left(e^{-\beta/M \cdot \hat{H}}\right)^M\right) = \mathrm{Tr}\left(\left(e^{-\Delta\tau \cdot \hat{H}}\right)^M\right) \tag{3.2}$$

which is called a Suzuki-Trotter decomposition, see Refs. [56, 57], with a large integer M and the imaginary time step $\Delta\tau = \beta/M$. Let us regard the case of a Hamiltonian that can be written as a sum of two contributions $H = H_A + H_B$. As an example, these could be the operators acting on even and odd bonds[53] of a bipartite lattice, as used in the next paragraph, but as of now, any other decomposition is also possible. Then there are several possibilities to decompose the exponential in Eq. (3.2), of which the easiest ones are[58]

$$e^{-\Delta\tau(H_A+H_B)} = e^{-\Delta\tau H_A} \cdot e^{-\Delta\tau H_B} + \mathcal{O}\left((\Delta\tau)^2\right)$$
$$e^{-\Delta\tau(H_A+H_B)} = e^{-\frac{1}{2}\Delta\tau B} \cdot e^{-\Delta\tau A} e^{-\frac{1}{2}\Delta\tau B} + \mathcal{O}\left((\Delta\tau)^3\right)$$

and the accuracy of the expansion becomes better, the smaller the commutator of the two operators is. Inserting this into Eq. (3.2) gives, however, the same result for both cases (compare Ref. [55]) using the cyclic permutation under the trace:

$$Z = \mathrm{Tr}\left(\prod_{l=1}^{M} e^{-\Delta\tau H_A} \cdot e^{-\Delta\tau H_B}\right) + \mathcal{O}\left((\Delta\tau)^2\right)$$

Thus the systematic error of a single decomposition scales as $\propto (\Delta\tau)^3$, but since this occurs for each single factor in the product[58], the overall error is again $\Delta_{\mathrm{tot}} \propto M\,(\Delta\tau)^3 \propto (\Delta\tau)^2$. For the special case of commuting operators $[H_A, H_B] = 0$ the decomposition would be exact. Such commuting operators are however hard to achieve in real systems.

In the next step, a complete set of basis states $|\sigma\rangle$ of the underlying Hilbert space is used with $\mathbf{1} = \sum_\sigma |\sigma\rangle\langle\sigma|$, where it is convenient to choose a basis in which part of the involved operators are diagonal, e.g. the S^z basis for a spin Hamiltonian. Then one can further rewrite[55]

$$\begin{aligned} Z &= \sum_{\sigma^0} \left\langle \sigma^0 \left| \prod_{l=1}^{M} e^{-\Delta\tau H_A} \cdot e^{-\Delta\tau H_B} \right| \sigma^0 \right\rangle + \mathcal{O}\left((\Delta\tau)^2\right) \\ &= \sum_{\sigma^0,\sigma^1,\ldots,\sigma^{2M-1}} \left\langle \sigma^0 \left| e^{-\Delta\tau H_A} \right| \sigma^1 \right\rangle \left\langle \sigma^1 \left| e^{-\Delta\tau H_B} \right| \sigma^2 \right\rangle \cdot \ldots \cdot \left\langle \sigma^{2M-1} \left| e^{-\Delta\tau H_B} \right| \sigma^0 \right\rangle + \mathcal{O}\left((\Delta\tau)^2\right) \end{aligned} \tag{3.3}$$

where the superscript indices in σ^i indicate the possibility of choosing different basis sets. Usually H_A and H_B are built up of single-bond operators which represent the interaction between two sites of the lattice, as for example in Eq. (3.4). This decomposition can be visualized in a so-called world-line configuration like in Fig. 3.1 (left), where the horizontal axis is the spatial dimension, while the vertical axis represents the imaginary time dimension. Note that one returns to the original configuration after M steps.

If we consider again the example of a one-dimensional lattice with only nearest-neighbor spin operators, separated into the above mentioned even and odd bonds, $H_A = \sum_i H_{2i,(2i+1)}$ and $H_B = \sum_i H_{(2i+1),2i}$, then in both H_A and H_B the summands—as the single-bond operators—all commute with each other[58]:

$$[H_{i,i+1}, H_{i+2j,i+2j+1}] = 0 \quad \forall j$$

Then in each matrix element in Eq.(3.3), the matrix exponentials exactly factorize into a product of exponentials of the single-bond operators. This is called the checkerboard decomposition, compare e.g. Ref. [59]. When the basis states are chosen appropriately, these matrix products of single-bond operators can be directly calculated. However, we still have an extremely large configuration space due to the sums over all basis unit decompositions in Eq. (3.3). The Monte-Carlo approach is now to *sample over* this configuration space by picking out a specific basis state $|\sigma_i^n\rangle\langle\sigma_i^n|$ in each Trotter step n, so that each sweep consist of M successive configurations that are changed only by the effect of maximally one single-side operator per step. As further

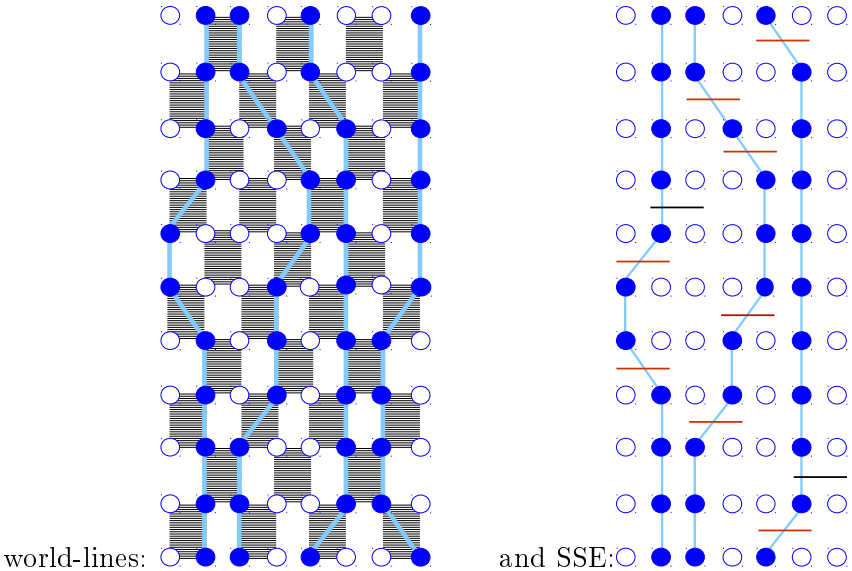

Figure 3.1.: Left: A visualization of a conventional world-line Monte-Carlo sweep on a one-dimensional system with checkerboard decomposition for $L = 8$ and $M = 10$. Filled and empty dots stand for spin $\sigma =\uparrow$ and $\sigma =\downarrow$, respectively. Each black square represents a matrix element. Right: A sketch representing an operator string in SSE with expansion level and $M = n = 10$ with $L = 7$ sites. There are no steps with unit operators in this example. The black bars represent the diagonal operator $H_{1,b}$, while the red bars are the off-diagonal $H_{2,b}$. For simplicity, we only considered nearest-neighbor correlations here. In both pictures, the light blue lines stand for the so-called world lines that serve as a guide to the eye. Naturally, one can draw equivalent lines between the white spin up sites.

constraints, operators on even and odd bonds must alternate, and when starting in the state $\left\langle \sigma_j^0 \right|$ we have to return to that initial configuration $\left| \sigma_j^0 \right\rangle$ in the end.

To sample over the subscript indices i, j, i.e. over the intermediate configurations in the imaginary time dimension, one then implements specific update procedures that successively change part of the picture in Fig. 3.1. These, too, have to fulfill certain constraints while still reaching the whole configuration space. These are mostly model dependent and in many cases the same as for the stochastic series expansion. So we will first review the SSE method here before coming to the update procedures in Sec. 3.1.2.

Stochastic Series Expansion The stochastic series expansion (=SSE) technique was developed in 2003 by Sandvik, and in part Kurkijärvi, compare Refs. [33, 34, 60]. The technique is an important improvement to formerly known quantum Monte Carlo approaches (see above) and is based on a high-temperature expansion of the partition function. The key idea is to write out traces over parts of the Hamiltonian as sums over diagonal matrix elements. The method can be applied to various quantum spin systems and systems of bosons[54]. SSE fits extremely well for our case, because it makes the implementation of long-range interactions much more efficient[60]. In quantum lattices, for ferromagnetic interactions in general, or for antiferromagnetic interactions on bipartite lattices, the method can be made sign-problem free through an appropriate basis choice[54]. The computational cost scales linearly[55] in the system size as well as in the inverse temperature $\beta = 1/T$. For the SSE algorithm we start again from the partition function, written as $Z = \sum_\alpha \left\langle \alpha \left| \sum_{n=0}^{\infty} \frac{\beta^n}{n!} (-1)^n H^n \right| \alpha \right\rangle$. In the systems considered here, the Hamiltonian is a sum over the lattice sites

$$H_{\text{Heisb.}} = \sum_{i,j} J_{ij} \boldsymbol{S}_i \boldsymbol{S}_j \qquad \text{or } H_{\text{Ising}} = \sum_{i,j} J_{ij} S_i^z S_j^z \tag{3.4}$$

with short-range or long-range behavior depending on J_{ij} and multiple possible lattice shapes.

In contrast to the above method, the power of the Hamiltonian that occurs in Z is now expanded in a sum over all possible products, all possible permutations placing one of the involved operators between each pair of lattice sites that is affected by interaction. This can be made clear by again introducing the above used bond operators, which each connect two single-site spin operators. Let us regard the following example, taken from Ref. [55]: The Heisenberg Hamiltonian is rewritten into bond Hamiltonians in the following form:

$$H = \sum_{i,j} J_{ij} \boldsymbol{S}_i \boldsymbol{S}_j = -\sum_{b=1}^{N_b} (H_{1,b} - H_{2,b}) + \sum_{b=1}^{N_b} J_{i(b)j(b)} \frac{N_b}{4} \tag{3.5}$$

with

$$H_{1,b} = J_{ij} \left(\frac{1}{4} - S_{i(b)}^z S_{j(b)}^z \right) \qquad H_{2,b} = \frac{J_{ij}}{2} \left(S_{i(b)}^+ S_{j(b)}^- + S_{i(b)}^- S_{j(b)}^+ \right)$$

Sites i and j are nearest neighbors, b is the index of the bond between them, and N_b is the total number of bonds in the system, i.e., for a chain with length L is $N_b = L - 1$. The constant energy

offset will be dropped in the following. A spin Hamiltonian of this type on any lattice and for any real prefactors J_{ij} can be described by these bond operators. With this, we can rewrite the partition function as

$$Z = \sum_{\alpha} \sum_{\mathcal{S}_n} \frac{\beta^n}{n!} (-1)^{n_2} \left\langle \alpha \left| \prod_{i=1}^{n} H_{t(i),b(i)} \right| \alpha \right\rangle ,$$

where n_2 is the number of operators $H_{2,b}$.

The weight $W(C_n)$ of a configuration C_n according to Eq. (3.1) then enters the calculation as:

$$Z = \sum_{C_n} W(C_n) \qquad \text{with } W(C_n) = \frac{\beta^n}{n!} \left\langle \alpha \left| \prod_{i=1}^{n} H_{t(i),b(i)} \right| \alpha \right\rangle \tag{3.6}$$

where any configuration C_n has a defined expansion order n and comprises the start/end state σ and the operator sting $\mathcal{S}_n$ of length n, which must return the state σ on itself in the end. It now remains to test under which circumstances the weights $W(C_n)$ can become negative, which would lead to a sign problem in the simulation. As explained in Ref. [55], for a non-frustrated lattice the number n_2 of off-diagonal bond-operators must always be even to bring the system back to its original state $|\sigma\rangle$. So the factor $(-1)^{n_2} = 1$ can be ignored. Therefore, for an antiferromagnetic coupling $J > 0$ on a non-frustrated lattice no sign problem occurs. For a ferromagnetic interaction $J < 0$ it is better to omit the energy shift in Eq. (3.5). Then one writes instead $H = \sum_b \tilde{H}_{1,b} + H_{2,b}$ with $\tilde{H}_{1,b} = JS^z_{i(b)}S^z_{j(b)}$, and the factor $(-1)^n$ remains untouched. Like this, all $H_{1/2(b)}$ have negative prefactor, and this cancels with $(-1)^n$ in the partition function. If H contains a mixture of ferromagnetic and antiferromagnetic terms, then the energy shift must only be carried out for the antiferromagnetic ones. No frustration occurs in our system, so the calculation will be sign-problem free.

In the special case of the $S = \frac{1}{2}$ quantum Heisenberg model all matrix elements are equal to $\frac{1}{2}$, so that the weights are simply $W^{\text{Heis}}(C_n) = \frac{\beta^n}{2^n n!}$.

In practice it is of course not possible to work with infinitely long operator strings $n \to \infty$, and it is even much more convenient to have a fixed length M for all operator strings $\mathcal{S}_n$. To implement this, all operator strings with $n < M$ are filled up with unit operators $\mathbf{1} = H_{0,0}$, while all strings with $n > M$ can be discarded without losing precision if the cutoff M is chosen "large enough to reduce the truncation error below the statistical error of the Monte Carlo simulation" (quote from Ref. [34]). Usually, M can be determined during the thermalization process[55], compare Sec. 3.1.3. The insertion of unit operators, however, slightly changes the calculation of the partition function[54, 55]. Taking into consideration that there are $\binom{M}{n}$ different possibilities to insert $M - n$ unit operators into a string of n operators gives the following

$$Z = \sum_{\alpha} \sum_{\mathcal{S}_M} \frac{\beta^n (M-n)!}{M!} \left\langle \alpha \left| \prod_{i=1}^{M} H_{t(i),b(i)} \right| \alpha \right\rangle$$

with n the number of non-unit operators in $\mathcal{S}_M$.

In the spin $\frac{1}{2}$ Heisenberg model, the matrix elements give 1 for the unit operator and $\frac{1}{2}$ otherwise. For L sufficiently large, the weights then essentially only depend on the number n of involved operators:

$$W^{\text{Heis}}(C_n) = \left(\frac{\beta}{2}\right)^n \frac{(M-n)!}{M!} \tag{3.7}$$

3.1.2. Update procedures

It is common and very helpful to represent a single configuration of operator stings in a graphical way, compare e.g. Ref. [60] Fig. 1 therein. Here Fig. 3.1 presents a sketch of the same type for a one-dimensional system with $L = 7$ sites. In the original worldline Monte-Carlo representations, the vertical axis was directly given by the imaginary time steps $\Delta\tau$ of the Suzuki-Trotter decomposition Eq. (3.3), and in the SSE algorithm this dimension represent the expansion level p and can also be identified as an imaginary time. As stressed in Ref. [60], it is sufficient to store the starting configuration and the operator string in the computer memory during a simulation.

It goes by itself that for a Monte Carlo simulation we need to sample over multiple such operator stings. To get from one to the next, special update schemes are necessary. The following explanations have been taken from Refs. [55, 58, 60].

Local updates The easiest update is a diagonal update: It replaces a unit operator by a diagonal operator and vice versa. No spins need to be flipped for this. The algorithm transverses the whole configuration in the direction of propagation levels. If at a propagation level p a unit operator acts, the algorithm replaces it by a diagonal bond operator—where the bond is chosen at random—with the probability:

$$P(\text{insert}) = P([0,0] \to [1,b]) = \min\left(\frac{\beta N_b}{M-n}\left\langle\sigma(p-1)\left|H_{1,b}\right|\sigma(p-1)\right\rangle, 1\right) \overset{S=\frac{1}{2}\text{Heisb.}}{=} \min\left(\frac{\beta N_b}{2(M-n)}, 1\right)$$

where n is the number of non-unit operators before the update. The second equality holds for the spin-$\frac{1}{2}$ Heisenberg chain for antiparallel spin orientations at bond b. In that system, we either have a parallel arrangement of the two involved spins, which leads to an immediate rejection of the update, or an antiparallel arrangement, for which the involved matrix element equals $\frac{1}{2}$.

If at propagation level p a diagonal operator is present, then the algorithm removes it and replaces it by a unit operator with probability

$$P(\text{remove}) = P([1,b] \to [0,0]) = \min\left(\frac{M-n+1}{\beta N_b}\frac{1}{\left\langle\sigma(p-1)\left|H_{1,b}\right|\sigma(p-1)\right\rangle}, 1\right) \overset{S=\frac{1}{2}\text{Heisb.}}{=} \min\left(\frac{2(M-n+1)}{\beta N_b}, 1\right)$$

where again n is the number of non-unit operators before the update.

The second type of local updates are off-diagonal updates. For the Heisenberg system, they are carried out by replacing two operators of type $H_{2,b}$ with diagonal operators of type $H_{1,b}$, and this involves flipping the spins next to the bond and between these two operators. Such a spin flip is not possible if other off-diagonal operators lie between the two chosen ones; however, the area

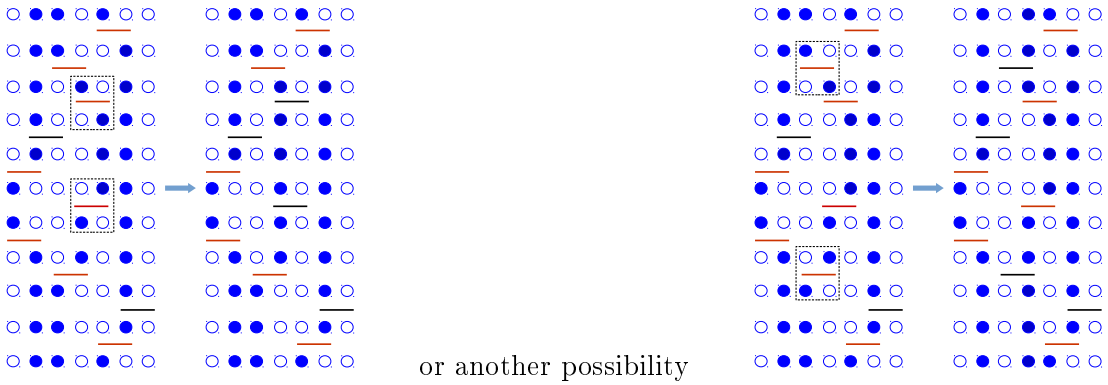

Figure 3.2.: These sketches visualize the effect of off-diagonal updates and are similar to Fig. 59 from Ref. [58]. For both choices of operators pairs here, there is only one possibility each to define the area where the spin should be switched. Spin cannot be switched if other offdiagonal operators act on them in the respective area.

"between" can be defined in two alternative ways, using the periodicity $|\sigma\,(p = N)\rangle = |\sigma\,(p = 1)\rangle$. Fig. 3.2 illustrates the update.

This sort of updates changes the configuration quite a lot, but they cannot change the winding number of the world lines in a one-dimensional system with periodic boundary conditions. While this does not present a problem if one is targeting the ground state of a system, it breaches ergodicity for any higher temperature[58]. Moreover, in two ore more dimensions, the whole configuration space cannot be targeted with only these local updates, either. Therefore, so called loop or cluster updates have been introduced.

Loop updates The loop updates ensure ergodicity in the update process, and they also significantly speed up the updating process. There are several versions of this in use, the one presented here is valid for the Heisenberg Hamiltonian and some related systems[58]. The recipe to construct a cluster is as follows: choose a spin and follow its world line until an operator is reached, then turn around along the operator and return in the opposite direction on the world line of the second spin that was on the same side of said operator, and continue that way—using periodic boundary conditions also in the imaginary time direction— until the loop closes. In Fig. 3.3 two examples are presented, one for a very small, the other for a very large loop. The whole configuration can be divided into such loops, with each spin uniquely belonging to one loop.

In the second step, these loops are flipped, and the adjacent operators must be switched from diagonal to off-diagonal and vice versa accordingly. This sort of update does not change the overall number of operators, and therefore in the spin $\frac{1}{2}$ Heisenberg model the weight of the configuration Eq. (3.7) remains unchanged, compare also Ref. [58]. For our case with long range interaction and an interaction strength J_{ij} that depends on the distance of the involved spins, it is important that not only the number, but also the position of operators remains unchanged, which is indeed the case. The only thing altered in the operator string is that some diagonal

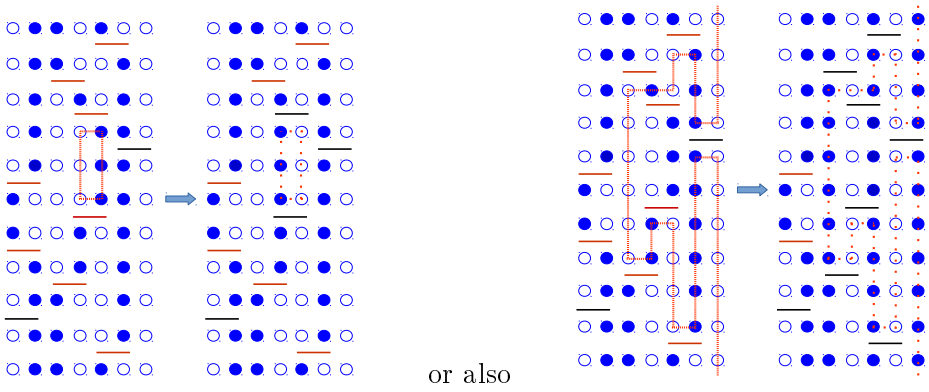

Figure 3.3.: Two possible steps in a loop update are shown here, again for a system with $L = 7$ sites and expansion level $n = M = 10$. For simplicity, only nearest neighbor interactions are considered. The dashed/dotted red lines mark the cluster and serve as guides to the eye.

operators are changed into off-diagonal ones, and the other way round. Due to the resulting matrix element being $J_{ij}/2$ for both $H_{1,b}(i,j)$ and $H_{2,b}(i,j)$, the weight of the configuration will remain the same also for our model. This is why loop updates for Heisenberg type spin systems can in principle always be accepted right away. Flipping all the loops included in the system takes it back to its original state, which is of course not helpful. One useful possibility is to arbitrarily choose the start spin and therewith the loop, but this suffers from the disadvantage that some loops will be switched twice, which is a waste of computational resources. The better approach[58] is to successively choose all involved loops and switch each with the probability $\frac{1}{2}$ in one such update.

Walker's alias method This method is used to increase the performance of the local updates by speeding up the choice of a bond operator. The idea behind the method is that in the process of choosing bonds at random, the discarding of choices should be avoided, while still keeping the stochastic probabilities. If a bond is chosen and the random variable generation would result in discarding the choice, then we will instead choose a substitute bond, which has been previously defined for the initially chosen bond. The following description is strongly based on the explanations given in Ref. [61, 62]:

The conventional technique for choosing a bond is the acceptance-rejection method[53]: To generate random variables that follow the desired distribution p_i with $\sum_{m=1}^{M} p_m = 1$, one carries out the following steps:

1. One generates a random, uniform distributed variable m_{try} for the "x-axis", with $0 < m_{\text{try}} < M$.
2. One generates a random, uniform distributed variable p_{try} for the "y-axis", with $0 < p_{\text{try}} < 1$.
3. If $p_{\text{try}} < p_m/p_{\max}$, then m is accepted in the set of random variables, otherwise m is rejected. The division by the maximal probability $p_{\max}$ serves as a normalization.

One can picture this method as choosing a random point on a plot of the function $p(x)$ and accepting the x-Coordinate if the point lies within the integral area of the function (compare the oftentimes used "shooting pi" example). This method has the major disadvantage that many trials are not used, but rejected, and it can hence become numerically very costly, especially if the underlying function p has a large variance.

Walker's method of alias circumvents this problem by designating an ersatz choice $a(m)$ for every m, so that in the third step, we accept m if $p_{\text{try}} < \frac{p_m}{p_{\max}}$ and otherwise we accept $a(m)$. Therefore, a table must be set up that assigns to each m a modified probability c_m, and a replacement choice $a(m)$ if $c_m < 1$. The modified probabilities must fulfill:

$$p_m = \frac{1}{N}\left(c_m + \sum_{k=1}^{M}(1-c_k)\,\delta_{a(k),m}\right)$$

A recipe for generating such a table from the original probabilities can be found in Ref. [62], App. A therein.

3.1.3. Measuring observables

Equilibration and binning The algorithm starts in a random configuration independent of the temperature at which the sampling takes place. The operator string at the start of the simulation is empty and will be successively filled with operators by diagonal updates[63]. Typically, this configuration will not represent a particularly probable state and the first few steps will be highly influenced by this starting configuration. Since the final outcome must be independent of the initially chosen state, one must designate the first steps of the procedure to the so-called thermalization and discard them for measurements. After these thermalization steps, the system has reached some state according to the stochastic probability. For our systems, a number of $N_{\text{equi}} = 10000$ equilibration steps has turned our sensible.

Another point that is important for avoiding statistical errors is the autocorrelation time. Since all updates only affect part of the configuration, consecutive measurements are not fully statistically independent. To quantify this effect, one defines the autocorrelation function, which measures the correlation in an observable A for two measurements that are i steps apart[53]:

$$C_A(i) = \frac{\langle A_k A_{k+i}\rangle - \langle A_k\rangle^2}{\langle A_k^2\rangle - \langle A_k\rangle^2}$$

The quantity is normalized to $C_A(0) = 1$, and if two measurements are fully statistically independent, then $C_A^{\text{ind}}(i) = 0$. In a Markov chain QMC simulation, the autocorrelation function decays exponentially[53] for the long-distance case:

$$C_A(i) \to e^{-i/\Theta_A},$$

which defines the autocorrelation time Θ_A.

Carrying out a measurement after each Monte Carlo step and using it as one independent result would not give a wrong estimate for the value $\langle A \rangle$ itself, but the statistical error $(\Delta A)^{\text{each}}$ would be wrong, because the true result should be

$$\Delta(A) = (\Delta(A))^{\text{each}} \sqrt{2\Theta_A^{\text{int}}} \qquad \text{with } \Theta_A^{\text{int}} = \frac{1}{2} + \sum_{i=1}^{\infty} C_A(i)$$

A derivation of the result is found in Ref. [53]. Due to the loop updates, autocorrelation times in SSE are considerably reduced[58, 64] with respect to older QMC implementations. To get fully rid of these effects, we apply a rebinning to our results, where M consecutive measurements are grouped together to one value each, in groups called bins (compare Ref. [53]). For large enough bin size M, the bin averages are then statistically independent, and according to the central limit theorem, they follow a Gaussian distribution[58]. In practice, we start from a previously chosen bin length and then follow a rebinning process, increasing the bin length by a factor of 2 in every step (and hence reducing the number of bins by the same amount). For each rebinning level, the average value and the statistical error are calculated. The result for $\langle A \rangle$ itself is easily obtained by the mean of results from the previous binning level and does not change systematically. If the error systematically increases up to a certain rebinning level, then the original bin length is not long enough, and one must instead use the error at said rebinning level, or start with a higher number M right away to get the correct error. If σ_A does not go up by rebinning, then M has been chosen large enough to get a correct σ_A. In our systems, we start at a bin length $M = 1000$ and proceed with rebinning till $M = 64000$. For $N = 10^6$ Monte Carlo sweeps, we then have 15 bins. For our systems, this bin number proves large enough for reliable results, and the error has saturated as this rebinning level. We use the last result $\sigma_A(M = 64000)$.

Linear response functions Diagonal operators can be measured right away during the course of the simulation: After a Monte Carlo sweep i, the mean over all propagation levels is determined as[55]

$$\langle A \rangle_i = \frac{1}{n} \sum_{p=0}^{n-1} \langle \sigma(p) |A| \sigma(p) \rangle \ ,$$

where p is the propagation level, represented by a line of dots in Figs. 3.1, 3.2, and 3.3. After the run, the different $\langle A \rangle_i$ are grouped in bins (see above), and then the overall estimate is determined as

$$\langle A \rangle = \frac{1}{N} \sum_{j=0}^{N} \langle A \rangle_j \ ,$$

which—as explained above—is independent of the number of bins.

The determination of generalized susceptibilities

$$\chi(\vec{q}) = \frac{1}{N} \sum_{ij} e^{-i\vec{q}(\vec{r}_i - \vec{r}_j)} \left. \frac{\partial \left\langle \hat{S}_i^z \right\rangle}{\partial h_j} \right|_{h_j = 0} = \frac{1}{N} \sum_{ij} e^{-i\vec{q}(\vec{r}_i - \vec{r}_j)} G(i,j)$$

with respect to an external field h_i is a bit more involved. The derivation given below follows the ones performed in Ref. [34] and Ref. [65]: The single-spin Green's function is given by

$$\begin{aligned}
G(i,j) &= \left(\frac{1}{Z}\frac{\partial}{\partial h_j} \mathrm{Tr}\left(\hat{S}_i^z e^{-\beta\left(\hat{H}-h_j\hat{S}_j^z\right)} \right) - \frac{1}{Z^2}\mathrm{Tr}\left(\hat{S}_i^z e^{-\beta\left(\hat{H}-h_j\hat{S}_j^z\right)} \right) \frac{\partial Z}{\partial h_j} \right)_{h_j=0} \\
&= \left(\frac{1}{Z}\sum_\alpha \frac{\partial}{\partial h_j} \sum_{n=0}^{\infty} \frac{(-\beta)^n}{n!} \left\langle \alpha \left| \hat{S}_i^z \left(\hat{H} - h_j \hat{S}_j^z \right)^n \right| \alpha \right\rangle - \left\langle \hat{S}_i^z \right\rangle \frac{1}{Z}\frac{\partial Z}{\partial h_j} \right)_{h_j=0} \\
&= \left(\frac{1}{Z}\sum_\alpha \sum_{n=1}^{\infty} \sum_{m=1}^{n} -\frac{(-\beta)^n}{n!} \left\langle \alpha \left| \hat{S}_i^z \left(\hat{H} - h_j \hat{S}_j^z \right)^{n-m} \left(-\hat{S}_j^z \right) \left(\hat{H} - h_j \hat{S}_j^z \right)^{m-1} \right| \alpha \right\rangle - \left\langle \hat{S}_i^z \right\rangle \frac{1}{Z}\frac{\partial Z}{\partial h_j} \right)_{h_j=0}
\end{aligned}$$

Now we send h_j to zero in the first summand:

$$\begin{aligned}
G(i,j) &= \frac{1}{Z_0}\sum_\alpha \sum_{n=1}^{\infty} \sum_{m=1}^{n} -\frac{(-\beta)^n}{n!} \left\langle \alpha \left| \hat{S}_i^z \hat{H}^{n-m} \hat{S}_j^z \hat{H}^{m-1} \right| \alpha \right\rangle - \left(\left\langle \hat{S}_i^z \right\rangle \frac{1}{Z}\frac{\partial Z}{\partial h_j} \right)_{h_j=0} \\
&= \frac{1}{Z_0}\sum_\alpha \sum_{n=1}^{\infty} \sum_{m=1}^{n} -\frac{(-\beta)^n}{n!} \left\langle \alpha \left| \hat{S}_j^z \hat{H}^{m-1} \hat{S}_i^z \hat{H}^{n-m} \right| \alpha \right\rangle - \left\langle \hat{S}_i^z \right\rangle \left(\frac{1}{Z}\frac{\partial}{\partial h_j} \mathrm{Tr}\left(e^{-\beta\left(\hat{H}-h_j\hat{S}_j^z\right)} \right) \right)_{h_j=0} \\
&= \frac{1}{Z_0}\sum_\alpha \sum_{\tilde{n}=0}^{\infty} \sum_{\tilde{m}=0}^{\tilde{n}} -\frac{(-\beta)^{\tilde{n}+1}}{(\tilde{n}+1)!} \left\langle \alpha \left| \hat{S}_j^z \hat{H}^{\tilde{m}} \hat{S}_i^z \hat{H}^{\tilde{n}-\tilde{m}} \right| \alpha \right\rangle - \left\langle \hat{S}_i^z \right\rangle \left(\frac{1}{Z}\frac{\partial}{\partial h_j} \mathrm{Tr}\left(e^{-\beta\left(\hat{H}-h_j\hat{S}_j^z\right)} \right) \right)_{h_j=0}
\end{aligned}$$

In most systems of relevance $\left\langle S_j^z \right\rangle = 0$. Moreover, one has $\hat{H} = \sum_{l=1}^{M} \hat{H}_l$, which leads to rewriting the powers of the Hamiltonian with operator strings $\mathcal{C}_n$ of length n. Again, the expansion of the exponential function can be cut at a sufficiently large L, and unit operators H_0 are inserted to take care of the summands $n < L$. Then $n(\mathcal{C}_L)$ is the number of non-unit operators in the operator string $\mathcal{C}_L$. The basis $\{|\alpha\rangle\}$ shall be chosen such that the $\hat{S}_j^z$ are diagonal with eigenvalues $S_j(\alpha)$. This yields

$$\begin{aligned}
G(i,j) &= \frac{1}{Z}\sum_\alpha \sum_{\mathcal{C}_L} \sum_{m=0}^{L} -\frac{(-\beta)^{n(\mathcal{C})+1}}{(n(\mathcal{C}_L)+1)!} \cdot \binom{L+1}{n(\mathcal{C}_L)+1}^{-1} \cdot \left\langle \alpha \left| \hat{S}_j^z \prod_{k=L-m+1}^{L} \hat{H}_{l_k} \hat{S}_i^z \cdot \prod_{r=1}^{L-m} \hat{H}_{l_r} \right| \alpha \right\rangle \\
&= \sum_\alpha \sum_{\mathcal{C}_L} \sum_{m=0}^{L} \frac{\beta}{L+1} \cdot S_j(\alpha_L) S_i(\alpha_m) \cdot W(\alpha, \mathcal{C}_L) \\
&= \left\langle \sum_{m=0}^{L} \frac{\beta}{L+1} \cdot S_j(\alpha_L) S_i(\alpha_m) \right\rangle_{W(\alpha,\mathcal{C}_L)}
\end{aligned}$$

The bracket $\langle ... \rangle_W$ denotes that the expectation value is calculated with respect to a sampling over configurations that follows the weight function

$$W(\alpha, \mathcal{C}_L) = \frac{1}{Z}\frac{(-\beta)^{n(\mathcal{C}_L)}(L - n(\mathcal{C}_L))!}{L!} \left\langle \alpha \left| \prod_{j=1}^{L} \hat{H}_{l_j} \right| \alpha \right\rangle$$

All allowed operator strings have to fulfill $\alpha_L = \alpha_0$, and moreover, we can form the average over the whole cyclic operator string. We then get:

$$\begin{aligned} G(i,j) &= \left\langle \sum_{m=0}^{L} \sum_{p=0}^{L-1} \frac{\beta}{L(L+1)} \cdot S_j(\alpha_p) S_i(\alpha_{m+p}) \right\rangle_W \\ &= \left\langle \frac{\beta}{L(L+1)} \cdot \left\{ \sum_{p=0}^{L-1} S_j(\alpha_p) \sum_{m=0}^{L-1} S_i(\alpha_m) + \sum_{p=0}^{L-1} S_i(\alpha_p) S_j(\alpha_p) \right\} \right\rangle_W \\ &= \left\langle \frac{\beta}{L(L+1)} \cdot \sum_{p=0}^{L-1} S_j(\alpha_p) \sum_{m=0}^{L-1} S_i(\alpha_m) + \frac{\beta}{(L+1)^2} \sum_{p=0}^{L} S_i(\alpha_p) S_j(\alpha_p) \right\rangle_W \end{aligned} \tag{3.8}$$

where in the last line the second summand compensates for the fact that in the product of two sums the case of equal indices occurs only once, while all other pairs are summed twice. The last expression can be accessed by direct measurements in the course of the QMC simulation.

The Bootstrap and Jackknife method for error calculation The SSE method allows for a direct measurement of diagonal operators and their response functions, as described above. In these cases, the errors can be determined right away from the statistical distribution after the binning analysis. If a combined quantity which is calculated directly from these observables is determined in the course of the Monte Carlo run, then one can calculate its error in the same manner as for the observables themselves. However, it is desirable to be able to calculate composite quantities and their errors from the know data after the Monte Carlo run has finished, and without starting it all over again.

The Bootstrap and Jackknife method are statistical resampling techniques, which we use here to obtain the error of these evaluables, i.e., derived quantities, from the direct results of the Monte Carlo simulation. In contrast to conventional Gaussian error propagation, the Jackknife method automatically respects cross-correlations and hence allows for a direct calculation of the errors e.g. of the Binder ratio $B = \langle m^4 \rangle / \langle m^2 \rangle^2$, where the involved measured quantities and their errors are not uncorrelated. The present short explanation follows the ones given in Refs. [66, 67]. Assume we have n uncorrelated Monte Carlo samples (after rebinning), from which we want to get the derived quantity c. For the Jackknife procedure, in each step we ignore the jth Monte Carlo sample and calculate one possible c_j from the remaining $n-1$ samples. In the next step, we then proceed by ignoring the $(j+1)$th sample and get a different result for the derived quantity c_{j+1} and so on. In the end, the final value for c is calculated from all Monte Carlo samples, and an estimator for its error is obtained via

$$\sigma = \sqrt{\frac{n-1}{n} \sum_{j=1}^{n} (c_j - c)^2}$$

To undermine the validity of this expression, one can check it on a very simple derived quantity, namely the sample mean $\bar{x} = \frac{1}{n}\sum_{i=1}^{n} x_i$. Ref. [67] gives the simple derivation for this case:

$$c_j - c = \frac{n\bar{x} - x_j}{n-1} - \frac{1}{n}\sum_{i=1}^{n} x_i = \frac{1}{n-1}\left(n\bar{x} - x_j - \frac{1}{n}\sum_{i=1}^{n}\{nx_i - x_i\}\right)$$
$$= \frac{1}{n-1}\left(n\bar{x} - x_j - n\bar{x} + \frac{1}{n}\sum_{i=1}^{n} x_i\right) = \frac{1}{n-1}\left(\bar{x} - x_j\right)$$

which leads to

$$\sigma_{\mathrm{jk}}^2 = \frac{n-1}{n}\sum_{i=1}^{n}(c_j - c)^2 = \frac{1}{n\,(n-1)}\sum_{i=1}^{n}(x_i - \bar{x})^2 = \sigma_{\mathrm{usual}}^2$$

Another, slightly more simple, resampling method for error calculation is the so called bootstrap. From the group of n sample numbers, n are chosen at random in each step, but it is allowed to take the same sample more than one time. It can be shown[66] that for this sampling with replacement, the standard deviation in the derived values c_j is a measure for the error of c, so one can calculate

$$\sigma_{\mathrm{boots}} = \sqrt{\overline{c^2} - \bar{c}^2} = \sqrt{\frac{1}{N}\sum_{j=1}^{N} c_j^2 - \left(\frac{1}{N}\sum_{j=1}^{N} c_j\right)^2},$$

where N is the number of restructured samples used. We will utilize the bootstrap method for measuring the errors of the critical exponents obtained by numerical fits. For details on the physics compare Sec. 3.6, and for the fitting see App. A.3. In these cases, our sample size usually only reaches values around $n \sim 30 - 35$, and we find that a resampling number of $N = 100$ appears to be adequate and give a reliable estimate.

3.2. General consideration for Heisenberg-like spin ladders

Quantities of interest The Heisenberg spin-$\frac{1}{2}$ ladder with antiferromagnetic couplings has already been subject of research for several decades. It can well be analyzed with quantum Monte Carlo techniques (for example Ref. [68]) as well as with DMRG (for example Refs. [59]), or for small systems with exact diagonalization (compare Ref. [69]). For the conventional ladder, and for an even number of legs in general, one finds that in the thermodynamic limit the system has an excitation gap and spin correlations fall off exponentially[70]. Thereby they resemble Haldane's conjecture on integral spin chains, Ref. [71]. In contrast to this, spin ladders with an odd number of rungs behave similar to a half-integer spin chain: They show gapless excitations and a power-law decay of the spin-spin correlations along the legs[70]. In this chapter, only the conventional two-leg ladder will be further looked at.

The most popular case is the one with all couplings antiferromagnetic, while the system with ferromagnetic legs has been less investigated. For the ferromagnetic XXZ leg interaction with additional rung coupling

$$H = -J\sum_{j=1}^{N}\sum_{\alpha\in\{1,2\}}\left(S_{\alpha,j}^x S_{\alpha(j+1)}^x + S_{\alpha,j}^y S_{\alpha(j+1)}^y + aS_{\alpha,j}^z S_{\alpha(j+1)}^z\right) + J_\perp^{xy}\sum_{j=1}^{N}\left(S_{1j}^x S_{2j}^x + S_{1j}^y S_{2j}^y\right) + J_\perp^z\sum_{j=1}^{N} S_{1j}^z S_{2j}^z$$

exist results based on bosonization: The work in Ref. [72] starts from the exact solution for the single XXZ chain and extends to the ladder in a perturbation approach with weak leg-coupling. Without the rung coupling, so in the case $J_\perp = 0$, one just has two independent ferromagnetic spin chains, whose solution is the obvious Néel ordering: In the ground state all spins point in one direction; which one is a result of arbitrary fluctuations: This effect is called spontaneous symmetry breaking. In a classical model one would expect an antiferromagnetic rung interaction $J_\perp > 0$ to stabilize this Néel order with spins on the the two legs pointing in opposite direction[69]. However, in the quantum setup, this is no longer case, because the antiferromagnetic rung interactions favor a singlet coupling between two opposite sites $|s\rangle = 1/\sqrt{2}\,(|\uparrow\downarrow\rangle - |\downarrow\uparrow\rangle)$, a superposition of both directions on each site that is not compatible with the ordered Néel state.

So for two-leg quantum ladder with ferromagnetic legs and antiferromagnetic bonds, there is a competition between two possible states: On the one hand, in the ordered phase, the ferromagnetic couplings dominate and both legs are (at least weakly) ordered ferromagnetically. This ferromagnetic order is quantified in terms of the leg magnetization, which is directly related to the spin structure factor along one leg:

$$m_{\text{leg}} = \sqrt{\frac{S_{\text{leg}}}{L}} = \frac{1}{L}\sqrt{\sum_{i,j} S^z_{1i} S^z_{1j}} \tag{3.9}$$

For an ordered phase we expect the spin excitation gap to vanish, so that any arbitrarily small amount of energy can cause spin excitations, namely bosonic spin waves. A quantity closely related to this feature is the uniform susceptibility. As can be found in Refs. [73] or [74], it is defined as

$$\chi_{\text{uni}}(T) = \frac{\beta}{2L}\left\langle \left(\sum_{i=1}^{L} \sum_{\alpha} S^z_{\alpha i} \right)^2 \right\rangle = \beta L \left\langle m^2 \right\rangle, \tag{3.10}$$

with $\beta = 1/(k_B T)$, and in our calculations we will always set the Boltzmann constant $k_B = 1$. The index $\alpha = A, B$ denotes the right or the left leg, respectively. Physically, χ_{uni} measures the linear response in the total magnetic moment $M = Lm$ when a uniform magnetic field is applied. The uniform susceptibility is suitable to find information about the spin excitation gap of a system: For a gapless system, $\chi_{\text{uni}}(T \to 0)$ tends to a finite, not vanishing value in the thermodynamic limit, which descriptively means that even at $T \to 0$ an arbitrarily small external field yields a small but finite answer of the system.

At this point it is important to state, however, that in a one-dimensional (or also two-dimensional) quantum system with homogeneous interactions, no magnetic long range order is possible at finite temperatures, following the Mermin-Wagner theorem Ref. [20]. So even in the case without rung coupling, will do not expect to see a classical Néel state, as one might intuitively assume. Instead, the critical temperature for this fully ordered state is $T_{\text{crit}} = 0$, and any small thermal quantum

fluctuation destroys the order. This is reflected when measuring the single leg susceptibility of the system.

$$\chi_{\text{leg}} = \sum_{ij} \frac{1}{L} \int_0^\beta d\tau \, \langle S_i(\tau) \cdot S_j(0) \rangle = \frac{1}{L} \int_0^\beta d\tau \, \langle M_{\text{leg}}(\tau) \cdot M_{\text{leg}}(0) \rangle \,, \tag{3.11}$$

which would be identical to χ_{uni} for a single spin chain. In the weakly ordered phase, the leg susceptibility diverges as $T \to 0$, reflecting the criticality of this point. For temperatures in the vicinity of zero, an arbitrarily small external magnetic field causes a huge reaction of the system, namely when the direction of the magnetic order is determined and a large amount of spins might be flipped.

On the other hand, we find the second competing phase to have dominant singlet formation along the rungs, and therefore a vanishing leg magnetization in the thermodynamic limit. Along with this come a vanishing uniform susceptibility $\chi_{\text{uni}}^{\text{rung-singlet}}(T \to 0) = 0$ and therefore a finite spin excitation gap at zero temperature. One can physically explain this by the finite amount of energy that is needed to break up the bond of at least one singlet state in order to go over from the ground state to an excited one.

In Ref. [72], it is shown that for the case of isotropic rung coupling, the system undergoes a phase transition as the anisotropy of the leg coupling vanishes $a \to 1$. At $a \lesssim 1$, the system is in the rung singlet phase with an excitation gap, while for $a > 1$ it is in the ferromagnetically ordered phase. For more details compare Fig. (4) in Ref. [72]. In Ref. [69] it is argued that for the fully isotropic case with $a = 1$ and $J_\perp^{xy} = J_\perp^z$, the ferromagnetic order in the thermodynamic limit is destroyed for any small rung coupling $J_\perp > 0$. Another investigation can be found in Ref. [75], where an nonlinear σ-approach is used and the same result is found, concerning the critical rung coupling in the isotropic case. Because our GNRs also map on an isotropic Heisenberg spin, it will be interesting to investigate to what extend this result also applies to the models that are set up in Sec. 3.3. However, we will first regard the results our SSE code gives for the conventional isotropic Heisenberg ladder.

Test: SSE for the antiferromagnetic Heisenberg ladder As an introduction, we will first probe the behavior of our QMC code[a] for systems that have already been well investigated, like the standard Heisenberg ladder.

Here, we just briefly reassess some of the key properties of the ferromagnetic Heisenberg ladder with antiferromagnetic rung coupling for comparison to later results. First, we examine the standard Heisenberg ladder with $J^{\text{AF}} = -J^{\text{F}} = 1.0$.

The uniform susceptibility Eq. (3.10) shows a maximum around $T \approx 0.6$, and it exponentially decays to zero as $T \to 0$ (compare Fig. 3.4) . This confirms the expectation that the system should have a spin excitation gap for isotropic leg coupling at non-vanishing rung couling. The

[a] The stochastic series expansion code has been written by Stefan Wessel, with a small adaption to spin ladder systems by Michael Golor. I have made some small adjustments and utilized the program for all the results in this and the following chapters, i.e. Secs. 3.2,3.3.2 , and 3.4—3.6

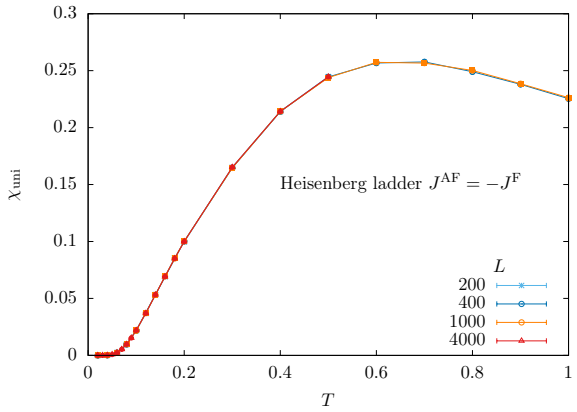

Figure 3.4.: The uniform susceptibility of the Heisenberg model with antiferromagnetic rung coupling and ferromagnetic legs decays exponentially as $T \to 0$. The different system lengths display almost no difference, so the system is converged to the thermodynamic limit. The data pionts for high temperatures and $L = 4000$ are omitted, because saturation is already visible.

different lengths display almost no visible difference, so we conclude that finite size effects do not play a role at these values for L. The plot is consistent with the result from Ref. [73] (Fig. 70 therein).

Using a perturbation theory approach for weak rung coupling it has been found in Ref. [59] that the uniform susceptibility of the two-leg Heisenberg ladder for low temperatures behaves as follows (with some real constant a):

$$\chi_{\mathrm{uni}}(T) = \frac{a}{\sqrt{T}} e^{-\Delta/T}$$

So the size of the spin gap Δ can be found as the axis intercept of the following expression[73]:

$$\chi_{\mathrm{fit}} = -T \cdot \ln\left(\sqrt{T}\chi\right) = \Delta - T \cdot \ln(a) \tag{3.12}$$

Here we find a value of about $\Delta^{\mathrm{F}} = 0.37$. This is different from the gap size for the purely antiferromagnetic Heisenberg ladder, as calculated in Ref. [59]: They find a value of about $\Delta^{\mathrm{AF}}_{\mathrm{lit}} \approx 0.5$.

Another interesting property, which we have not analyzed yet, is the decay of the spin-spin correlation. It is more closely related to the direct quantity of spin-spin correlations than the derived susceptibilities. Its decay indicates whether the system has long range order or not. A quasi long-range order component is given if the spin correlation has a portion that decays following a power law. For an exponential decay $\langle S_i S_{i+x}\rangle \propto e^{-x/\xi}$ however, long range order is absent, and instead the correlation length ξ is defined, on which the correlations decay.

The Heisenberg ladder for $J^{\mathrm{AF}} > 0$ does should have a long-range order, and Ref. [68] predicts a decay of the form

$$\langle S_i S_{i+x}\rangle = c \cdot \exp\left(-\frac{x}{\xi}\right) \cdot x^{-a} \tag{3.13}$$

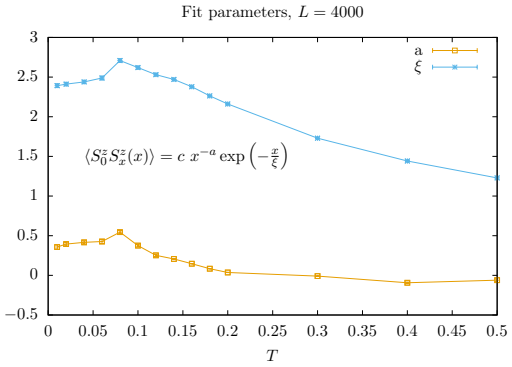

Figure 3.5.: The ranges for the fits are $x_{\text{fit}} \in [5, 25]$ for $T < 0.14$ and $x_{\text{fit}} \in [2, 20]$ for $T \geq 0.14$, respectively. The upper bound has been chosen by visual inspection, ignoring the long distances where the data is essentially noise. The lower bound is arbitrary to a certain extend: One must ignore short-range behavior, but also keep enough data points for a reliable fit. The constant prefactor is in all cases $c \sim 0.1$.

where $a \sim 0.5$ for small temperatures and $a \sim 0$ for higher temperatures, with a change at $0.2\Delta \lesssim T_{\text{change}} \lesssim 0.4\Delta$. We can confirm this result and find $T_{\text{change}} \sim 0.08$, compare Fig. 3.5. However, our fits of the spin-spin correlation function are not very stable, firstly due to the rather complicated form of Eq. (3.13), and secondly because it is difficult to adjust the fit range. The distances must be large enough to follow long-range behavior, but not so large that the values become completely washed-out by noise. The useful range has to be adjusted according to temperature. One can see two exemplary temperatures in Fig. 3.6. Despite these difficulties in fitting, this example shows that also for this sensitive quantity, the outcomes of our SSE simulation are in accordance with literature results.

Fig. 3.7 displays the leg magnetization Eq. (3.9), which is a measure for the ferromagnetic order, as a function of temperature for different ribbon lengths. As discussed before, the ground state of this model should be a gapped rung singlet phase[72]. Therefore, we explain the increase of the leg magnetization for small temperatures by by a breakup of the singlet bonds due to temperature. After T has reached ~ 0.2, the effect of thermal fluctuations disturbing the ferromagnetic order becomes stronger than this breakup, and the magnetization decreases again.

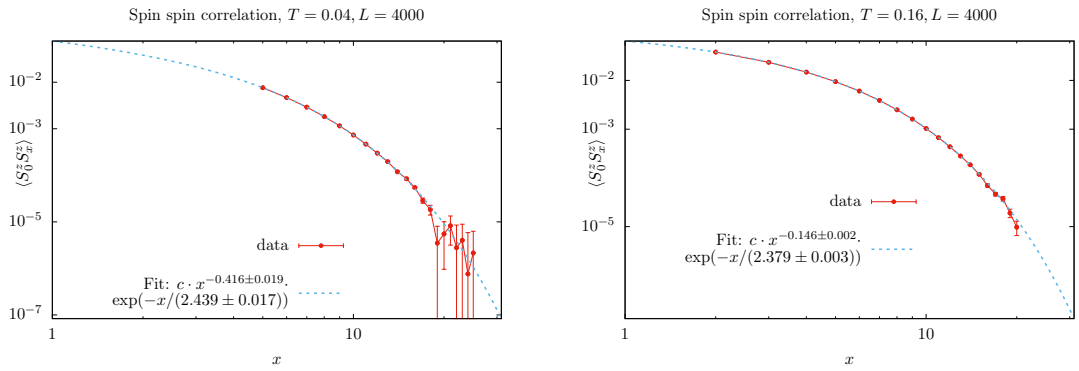

Figure 3.6.: The spin-spin correlation function Eq. (3.13) of the Heisenberg ladder with ferromagnetic legs and antiferromagnetic rungs.

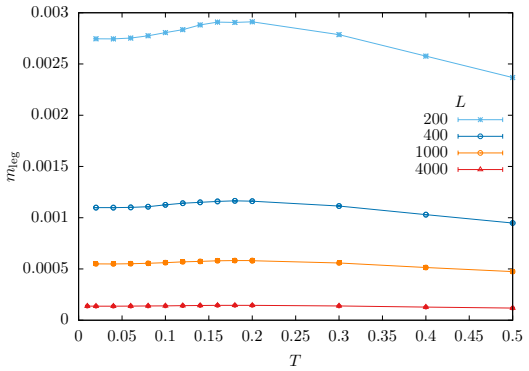

Figure 3.7.: The ferromagnetic order parameter for the standard Heisenberg ladder $J_{\text{F}} = -J_{\text{AF}}$ shows a maximum as a function of temperature. The plots are consistent with the expectation that the order vanishes in the thermodynamic limit.

3.3. From zigzag graphene nanoribbons to effective spin ladders

The results from this and the following chapters have been published before in Ref. [76]: Cornelie Koop and Stefan Wessel, Phys. Rev. B **96**, 165114 (2017) [a]. Some of the figures and text passages were taken from this publication.

3.3.1. Setup of the two models

In the first part of this thesis, the effective couplings between the magnetic edge states in plain zigzag graphene nanoribbons were determined in the context of an effective model for a Wannier edge state basis. In the following, the results from Chapter 2 shall be further investigated and the magnetic ground state properties of the system shall be looked at by means of quantum Monte Carlo simulations. For this, one needs to treat the system at small, but finite temperatures and derive the ground state behavior by extrapolation. In a similar manner, one can derive thermodynamic limit results from the analysis of several different finite system lengths. In detail, we will use the stochastic series expansion technique presented in the previous section (compare Sec. 3.1), which offers the possibility to obtain several quantities of interest, for example magnetizations and spin susceptibilities. We will remain in the equilibrium and first aim at describing the magnetic properties of the system's ground state and how they depend on the ribbon width and coupling constants. We can then try and investigate the phase diagram, checking if there is a finite temperature phase transition depending on T and/or a quantum phase transition depending on other parameters. For these questions, we are most interested in the properties in the thermodynamic limit, i.e., in the limit $L \to \infty$.

In Chap. 2 it was shown that the second order corrections do not dramatically alter the result for the coupling constants and can be safely neglected in most cases. As we will see below, for the quantum Monte Carlo analysis we need to look at large system sizes to overcome finite size effects. It is therefore sensible to neglect the second order corrections in the following and instead analyze only first order results, but longer ribbon lengths L than in Chap. 2. We will still regard similar widths in the range of $W = 8, 10, 12, 14, ...$ unit cells, where 8 unit cells is the minimum that allows for a second-order perturbation treatment of the leg coupling, when going over from the fermionic model to the spin model. Moreover, even values are necessary to have the zigzag structure qualitatively the same and to avoid an offset between the zigzag sites of right and left edge. For very large W the rung couplings become very small (compare Sec. 2.3.1), which makes those systems less interesting.

We now aim at determining the long-range behavior of the couplings, aiming at a generic description of long ribbons as effective spin ladders. Like this, we can afterwards also analyze the magnetic properties of the these spin ladder models using different length scales. Fig. 3.8 shows the coupling values together with a fit to power-law behavior $J^{\mathrm{F}}(r) = k \cdot r^{-\alpha}$ (left) and $J^{\mathrm{AF}}(r) = \tilde{k} \cdot r^{-\tilde{\alpha}}$(right) as a function of distance r measured in Wannier indices. To realize a logarithmic scale, we must omit the direct opposite rung coupling $J^{\mathrm{AF}}(0)$. The exponents

[a] For this paper, C. Koop did the calculations and most of the figures. Both authors worked together analyzing and interpreting the results. S. Wessel wrote the predominant part of the text and created Fig. 14.

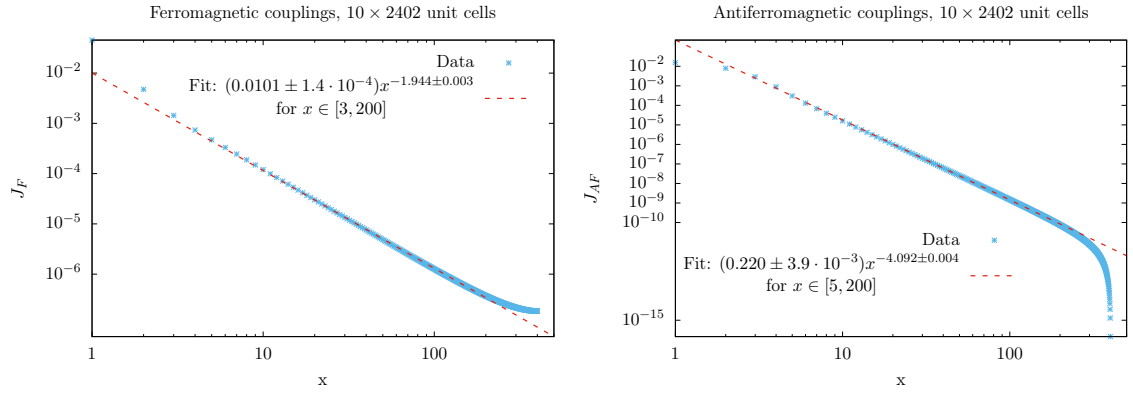

Figure 3.8.: In the framework of the effective model in Wannier basis, the ferromagnetic (left) as well as the antiferromagnetic (right) edge state couplings decay with a power-law behavior. For the fits, we ignore the first few steps to get the long-range behavior, and we do not take into account the range $x > 200$, because it appears to be influenced by finite-size effects. The number of edge states is one third of the number of unit cells, and periodic boundary conditions apply.

are identified as $\alpha \sim 2$ and $\tilde{\alpha} \sim 4$, respectively. It follows directly from the effective model calculation (compare Sec.2.1.2) that to leading order, the spin couplings scale with the original Hubbard parameters as

$$J^{\mathrm{F}} \propto U \qquad \text{and} \qquad J^{\mathrm{AF}} \propto \frac{t^2}{U}$$

Therefore, their relative magnitudes can be tuned by altering the underlying Hubbard model, but the values of the exponents are not influenced by this. One has to check now how the ribbon geometry influences the long-range behavior of the couplings.

As can be seen in Fig. 3.9, the length of the ribbon does not change either of the exponents beyond numerical uncertainties. This meets our expectations because the general dependence of the effective coupling parameters on the ribbon length is very weak, compare Sec.2.1.2. Moreover, it confirms that it is useful not to determine the parameters depending on lengths of actual nanoribbons, but to aim at analyzing the model properties near the thermodynamic limit, i.e. for $L \to \infty$.

The only relevant geometric dependence is that of short-ranged antiferromagnetic rung couplings on the ribbon width W. While the rung coupling to the direct opposite neighbor scales as $J^{\mathrm{AF}}(r = 0) \propto W^{-3}$ (compare Fig.2.8, where the width is named M instead), the long-range behavior is again much less affected by the ribbon width. In particular, there is no relevant dependence of the exponents of the power-law decay on ribbon width W, neither for the ferromagnetic leg coupling, nor for the antiferromagnetic coupling. This is displayed in Fig. 3.10.

In what follows, we want to simplify the picture and use more generic couplings to obtain models which should capture the essentials of the effective model coupling parameters, but which should also be of interest beyond the analysis of graphene nano ribbons and easily scalable to different

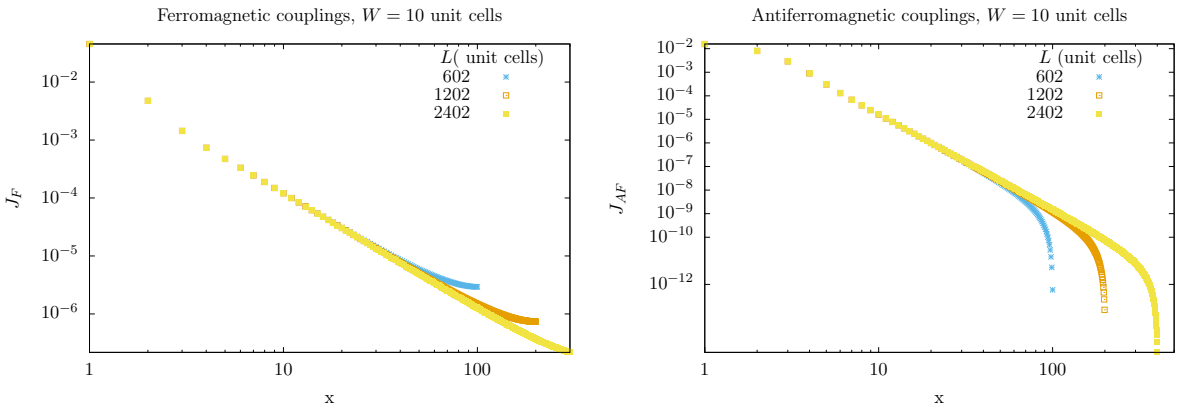

Figure 3.9.: The the coupling types for different ribbon lengths L at width $W = 10$ unit cells. Also here, the exponents of the power-law decay do not scale with the dimension, if finite size behavior (for large distances) is disregarded.

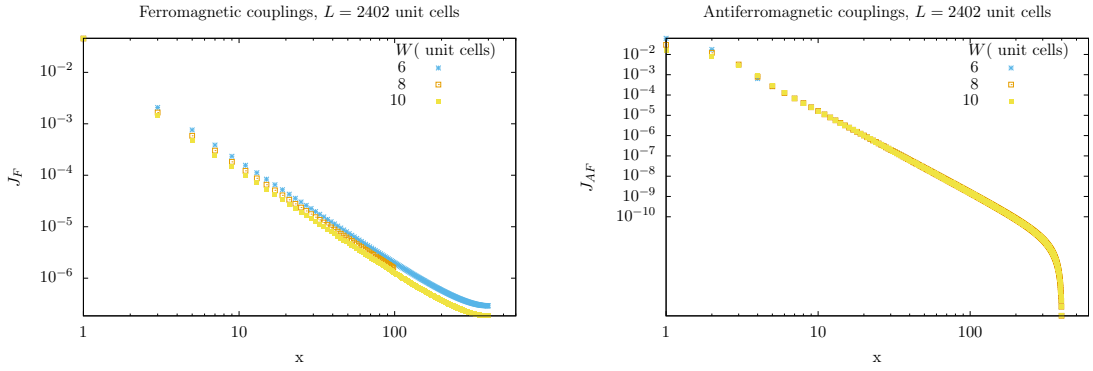

Figure 3.10.: The ferromagnetic and antiferromagnetic couplings, respectively, for different ribbon widths W. It is apparent that the exponent of the power-law behavior does not scale with W.

L. To realize this, in a first step we will approximate the long-range ferromagnetic leg coupling to decay as

$$J^{\mathrm{F}}(r) = J_1^{\mathrm{F}} \cdot \frac{1}{r^2} \ . \tag{3.14}$$

Note that the case $r = 0$ is the site itself and is therefore excluded. The pure numerical result for our GNRs is roughly $J_1^{\mathrm{F}}(r) \propto r^{-\alpha}$ with $\alpha \lesssim 2$, but one must consider that on the way to obtaining α many different approximation steps have been carried out. For example, the second-order influence of the bulk states was neglected here, and we regard the distances in terms of Wannier number instead of geometric distance. Finally, it seems plausible that our systems still show some minor finite-size effects, and the fit exponent is naturally also dependent on the choice of the range that the fit is applied to (e.g. $r \in [3, 200]$). After all, a value $\alpha < 2$ would lead to long-range magnetic order along the zigzag edges at non-vanishing temperature, which would be in contradiction to the exact Mermin-Wagner theorem, cf. Ref. [20]. So since the GNRs are isotropic and effectively one-dimensional, they cannot map onto an effective system of Wannier states with long-range order at $T \neq 0$. Our results, however, are well compatible with the generic exponent $\alpha = 2$, so we will use this in all that follows.

For the antiferromagnetic couplings, a reasonable approximation and generalization is to use the simplified exponent $\tilde{\alpha} = 4$. This is compatible with the fit results in Fig. 3.8 and the interaction is well beyond giving rise to a long-range order. We then have

$$J^{\mathrm{AF}}(r > 0) = J_1^{\mathrm{AF}} \cdot \frac{1}{r^4} \text{ and the constant } J^{\mathrm{AF}}(r = 0) = J_0^{\mathrm{AF}} \tag{3.15}$$

In addition to that, we have to determine the short range coupling constants in a useful and generic way.

For $U = t = 1$ and a ribbon width of $W = 10$, we get $J_0^{\mathrm{AF}}/J_1^{\mathrm{F}} \approx 0.43$ from a comparison of the true nearest-neighbor results from the effective model. However, if we first did the fit according to Fig. 3.8 and then extrapolated the values for $J^{\mathrm{F}}(r = 1)$ and $J^{\mathrm{AF}}(r = 1)$ from the axis intercept in the log-log plot, then we would get $J^{\mathrm{AF}}/J^{\mathrm{F}} \approx 21.8$, orders of magnitude higher. This is due to the stark deviation of the short-range behavior from the fit to the long-range tail, where the ferromagnetic couplings to close neighbors are enhanced compared to the fit result, while the antiferromagnetic couplings for small r are suppressed compared to the power-law behavior. The main reason for the latter effect is simply geometrical: For short distances along the ribbon, the true geometric distance between Wannier sites iA and jB is not given by r_{ij}, but by a trigonometric relation involving the ribbon width, which changes the values especially for wide ribbons.

In order to find a good effective description for long zigzag nanoribbons in terms of spin ladders, on the one hand we must choose a realistic, but also sufficiently generic exponent for the long-range decay, so that large system sizes can be analyzed and also yield a result of general interest. On the other hand, for the short-range behavior we would like to implement values that describe the GNRs in a realistic way.

r	$J^{\mathrm{F}}(r)$	$J^{\mathrm{AF}}(r)$
0	-	0.0196417
1	0.0453914	0.0155852
2	0.0047475	0.0079814
3	0.0014386	0.0028894
4	0.0007365	0.0008942

Table 3.1.: Values of the spin exchange couplings for lateral distances $r \leq 4$, as obtained for the effective spin ladder model for $W = 10$ nanoribbon. These constants are used for the Hamiltonian H_1. For $r > 4$, the couplings are obtained from the algebraic fits in Eqs. (3.14) and (3.15) with $J_1^{\mathrm{F}} = 0.01009$ and $J_1^{\mathrm{AF}} = 0.21972$.

Therefore we will look at two different models: The first one should be as realistic as possible, and as a representative example the width is chosen to be $W = 10$ unit cells and the original Hubbard parameters $U = t = 1$. For the coupling values to close neighbors, namely with $r \leq 4$, we will then use the outcome of the effective model, compare Tab. 3.1, while for the "tail" of the interaction ($r > 4$) the couplings are taken from the power-law decays Eq. (3.14) and Eq. (3.15), respectively. The factors for this also stem from the fits, giving for the leg couplings $J_1^{\mathrm{F}} = 0.01009(14)$ and for the rung coupling $J_1^{\mathrm{AF}} = 0.21972(391)$. So the Hamiltonian writes

$$H_1 = -\sum_{i,j,\ i\neq j} J^{\mathrm{F}}(r_{ij})\,(\boldsymbol{S}_{i1}\cdot\boldsymbol{S}_{j1} + \boldsymbol{S}_{i2}\cdot\boldsymbol{S}_{j2}) + \sum_{ij} J^{\mathrm{AF}}(r_{ij})\,\boldsymbol{S}_{i1}\cdot\boldsymbol{S}_{i2} \tag{3.16}$$

where $\boldsymbol{S}_{i1/2}$ are the Heisenberg spin operators, and r_{ij} is the distance between sites i and j, measured in number of Wannier states. The two legs of the ladder are represented by indices 1 and 2, respectively.

In the second model, we will look at an even further simplified model Hamiltonian, which is obtained by truncating the antiferromagnetic coupling beyond its nearest-neighbor term and using a $1/r^2$ decay for all ferromagnetic couplings $r \geq 1$. This leads us to an more genuine spin model with Hamiltonian

$$H_2 = -J_{\mathrm{F}}\sum_{i,j}\frac{1}{r_{ij}^2}\,(\boldsymbol{S}_{i,1}\cdot\boldsymbol{S}_{j,1} + \boldsymbol{S}_{i,2}\cdot\boldsymbol{S}_{j,2}) + J_{\mathrm{AF}}\sum_{i}\boldsymbol{S}_{i,1}\cdot\boldsymbol{S}_{i,2}. \tag{3.17}$$

In the limit of $J_{\mathrm{AF}} = 0$, this model corresponds to two decoupled spin chains with a ferromagnetic $1/r^2$ exchange interaction. In the thermodynamic limit, this is described by the ferromagnetic Haldane-Shastry model, for which an exact solution has been derived for its thermodynamic properties (compare Refs. [35–37] and Sec. 3.5).

To unify the different ladders, all models are scaled in such a way that the strongest leg coupling, i.e., the coupling to the nearest neighbor along the leg, has the value $J^{\mathrm{F}}(r = 1) = -1.0$. However, in order to systematically study the physics of the Hamiltonian H_1 with the above form of the couplings, it turns out instructive to tune the relative strength of the inter-leg to intra-leg

couplings. For this purpose, we introduce a dimensionless quantity λ, which uniformly rescales all the inter-layer couplings as

$$J^{\mathrm{AF}}(r) \to \lambda\, J^{\mathrm{AF}}(r). \tag{3.18}$$

Hence, for $\lambda = 1$ we recover the original model, while for large λ we (artificially) enhance all the antiferromagnetic inter-leg couplings with respect to the ferromagnetic intra-leg couplings. We can alternatively express the relative strength of the rescaled antiferromagnetic couplings in terms of the dimensionless parameter

$$g = \frac{\lambda\, J^{\mathrm{AF}}\,(r=0)}{J^{\mathrm{F}}(r=1)} \tag{3.19}$$

between the strongest antiferromagnetic and ferromagnetic coupling constants. For the second model H_2, the parameter g is given explicitly by $g = \frac{J_{\mathrm{AF}}}{J_F}$.

3.3.2. Comparison to Exact Diagonalization

To test the validity of the quantum Monte Carlo results, we compare them to the findings with exact diagonalization [a] for the Hamiltonian H_2 of the generic model, with $J_{AF} = 0.43$. The uniform susceptibility is given by Eq. (3.10):

$$\chi_{\mathrm{uni}} = \frac{1}{k_B T \cdot 2L} \sum_{i,j} \frac{1}{Z} \cdot \mathrm{Tr}\left(e^{-\beta H} S_i^z S_j^z\right) \tag{3.20}$$

Following [46] and [77], the leg susceptibility is calculated via

$$\begin{aligned} \chi_{\mathrm{leg}} &= \sum_{ij} \int_0^\beta d\tau \,\langle \boldsymbol{S}_i(\tau) \cdot \boldsymbol{S}_j(0)\rangle = \int_0^\beta d\tau\, \frac{1}{Z} \mathrm{Tr}\left(e^{-\beta H} \cdot (\boldsymbol{S}_i(\tau) \cdot \boldsymbol{S}_j(0))\right) \\ &= \int_0^\beta d\tau\, \frac{1}{\mathrm{Tr}\left(e^{-\beta H}\right)} \mathrm{Tr}\left(e^{-(\beta-\tau)H} \cdot \boldsymbol{S}_i e^{-\tau H} \cdot \boldsymbol{S}_j(0)\right) \end{aligned} \tag{3.21}$$

where the integration is carried out numerically[b].

For the uniform susceptibility, we find good accordance for both system sizes $L = 3,\ 4$. The leg susceptibility is numerically much more demanding due to the integration and can only be carried out for $L = 3$. The results are also equal as expected.

[a] Caution: For comparison to ED, we locally changed the stochastic series expansion to accept a maximal coupling distance $J(x_{max}) = J(L/2)$, so that due to the periodic boundary conditions this one coupling counts twice. The same is true for the exact diagonalization code, of course. Otherwise we could only have nearest-neighbor couplings even for $L = 8$. [b] We use the Mathematica 10 function "NIntegrate"

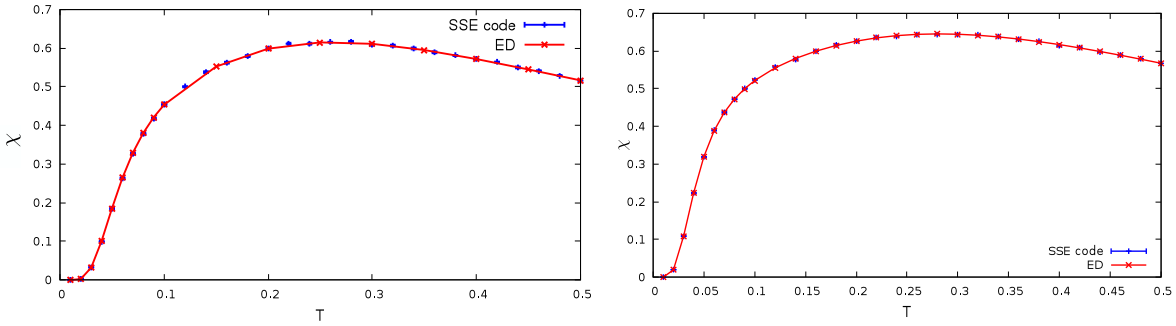

Figure 3.11.: The uniform susceptibility (Eq.(3.20)) for system sizes $L = 3$ (left) and $L = 4$ (right) for Hamiltonian H_2 for exact diagonalization and the SSE code. We used 10^6 runs, and a bin length of 1000. For the SSE results, the error bars are smaller than symbol size.

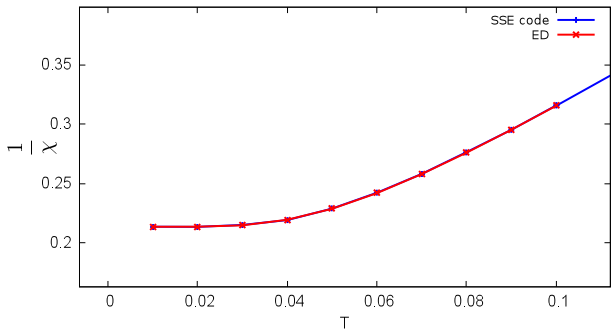

Figure 3.12.: The leg susceptibility for H_2 and $L = 3$, comparing SSE results to exact diagonalization.

3.3.3. Finite Size effects and Ewald summation

In the following, the impact of finite size effects on the results shall be looked at in more detail. As suggested in Ref.[78], we compare the pure leg susceptibility to the exact expression for different lattice sizes. As we will see later (compare Fig.3.30 left), for a pure chain even a calculation with the rather large number of $L = 10^5$ lattice sizes suffers from severe finite size effects for very small temperatures.

To improve the accuracy without having to use more computing capacity, we will use a concept called "Ewald summation"[79], which virtually sums up interactions to all copies of the finite chain that are connected via periodic boundary conditions:

$$J_{ij} \to \sum_{n=-\infty}^{\infty} \frac{1}{(j_{ij} - nL)^2} = \frac{\pi^2}{L^2} \frac{1}{\sin^2\left(\frac{\pi j}{L}\right)} \tag{3.22}$$

For the derivation of the closed expression for the sum, compare App. A.2.

On the one hand, usage of the Ewald summation does not much improve the performance in the pure Haldane-Shastry chain, as displayed in Fig. 3.13. On the other hand, it does, however, make a difference for the coupled chains with finite anti-ferromagnetic correlations, compare Fig. 3.14

In the following we will always employ this type of summation, and the effective value for $J^{\mathrm{F}}(1)$ used in the numerics will therefore be a little larger than the analytic one: $J^{\mathrm{F}}_{\mathrm{eff}}(i, i+1) > J^{\mathrm{F}}_{\mathrm{analyt}}(i, i+1) = 1.0$. The Ewald summation helps in reaching higher accuracies, but as one can see in the right plot from Fig. 3.14, even with this summation we will not be able to numerically reach the ground state of the thermodynamic limit in the ordered phase, at least not with a reasonable numerical effort in terms of system length and number of simulation steps.

In most cases in the future we will not aim at reaching the thermodynamic limit by regarding very large system sizes, but instead try and extrapolate the thermodynamic limit behavior with finite-size scaling plots.

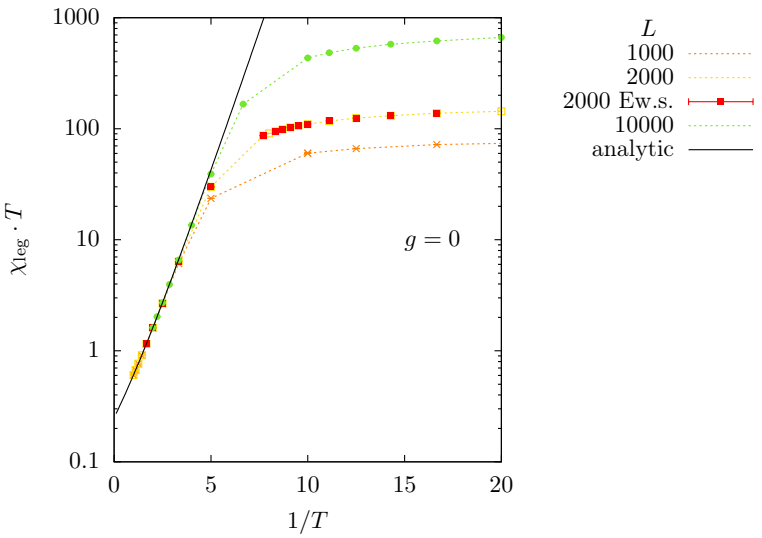

Figure 3.13.: Susceptibility of the ferromagnetic Haldane-Shastry chain for different system sizes with and without Ewald summation. The black line represents the exact result from Bethe ansatz $\chi = \frac{\beta}{2\pi} \int_0^{\pi/2} \exp\left(-2\beta \cdot \frac{1}{4}\left(\nu^2 - \frac{\pi^2}{4}\right)\right) d\nu$ (compare Eq. (16) from Ref.[37]). Numerical integration was performed with Mathematica.

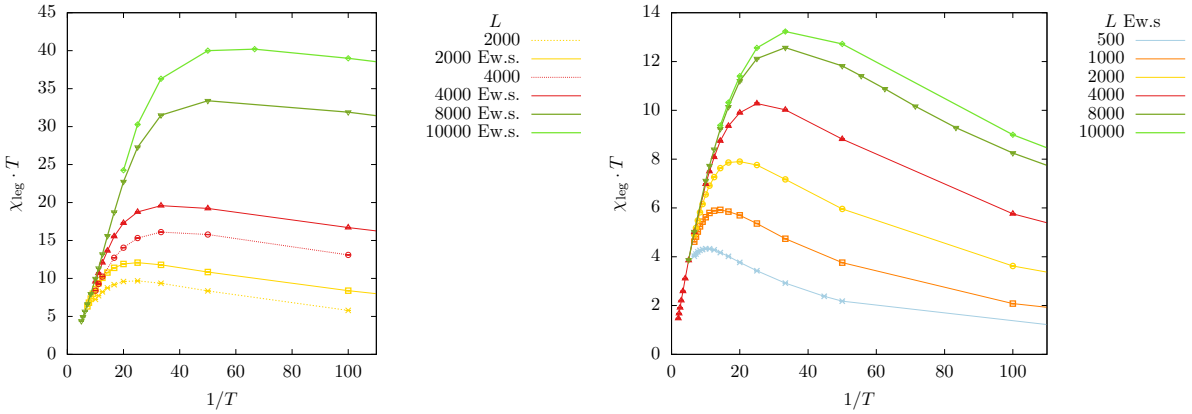

Figure 3.14.: Left: The pure leg susceptibility as a function of inverse temperature for different ribbon lengths exhibits a visible change depending on whether the Ewald summation is used. The coupling strength is $g = 1.94$. Right: Even with the Ewald summation, the results are still not independent of the system size, especially for $L = 2002$ and $L = 4002$ and small temperatures. The plot shows the case $g = 1.96$.

3.3.4. Quantum phase transitions: brief overview

Classical phase transitions are a phenomenon well-known in everyday life: A material changes its properties in a sudden and significant way at some critical parameter, the most prominent example being the change of an aggregate state when reaching the melting or vaporization temperature T_{crit} (at a suiting pressure). But a phase transition can also affect the magnetic properties of a sample, for example in the two-dimensional Ising model (compare e.g. Ref. [80]) with the Hamiltonian $H = J \sum_{\langle i,j \rangle} s_i^z s_j^z$. In the thermodynamic limit at finite temperature, two different phases exist: Above the critical temperature the system is disordered and paramagnetic, while below T_c there is a spontaneous symmetry breaking, and the system is ordered with all spins pointing in one direction, which is called the ferromagnetic phase. The spins are then oriented in z direction, whether they point all up or all down at zero external field is arbitrary, in other words it depends on quantum fluctuations.

A classical phase transition can be assigned an order, where most relevant experimental examples are first and second order phase transitions. Formally, the order of a phase transition is determined using the Ehrenfest theorem[80]: A system undergoes a phase transition of order n, if the nth derivative of the free energy $F(T, V, N_1, ..., N_r) = -k_B T \ln(Z)$, with respect to any of its arguments, exhibits a discontinuity (and all lower order derivatives are continuous). Here, $N_1, ..., N_r$ denote the particle numbers of the different compounds, V is the volume and T the temperature. For example, a melting metal undergoes a phase transition of first order, and if all other parameters are kept constant, then the pressure $-p = \frac{\partial F}{\partial V}$ changes abruptly.

In contrast to these thermal phase transitions, a quantum phase transition (QPT) takes place at $T = 0$ and is driven by a different parameter, for example an interaction strength in the Hamiltonian or an external field. A central feature in the description of quantum phase transitions is the correlation length ξ of the system. One can understand the correlation length e.g. via its inverse $\frac{1}{\xi}$, which can be seen as a measure for how strong the system behaves locally. For example, for the quantum Ising model, Ref. [81] defines an "effective spin", which is the average of the microscopic spins, and this effective spin then has the size ξ. In other words, one has to regard the average in a physical quantity over areas with a volume $V \geq \xi^d$ (in dimension d) to get a meaningful result that is not dominated by random fluctuations (compare Ref. [80] p. 10).

At the quantum critical point, this length scale diverges—typically as $\xi = |g - g_{\text{crit}}|^{-\nu}$ with some critical exponent ν (compare Sec.3.6). The model then looks equal on all physical length scales, and for example in an electron system, the wavefunction is a superposition of quantum entangled configurations fluctuating at all length scales, compare Ref. [81]. Consider as another example the one-dimensional quantum Ising chain with an external transverse field

$$H_{\text{Ising}} = -Jg \sum_i s_i^x - J \sum_{\langle i,j \rangle} s_i^z s_j^z$$

as described e.g. in Ref. [82] (p. 10 ff.): The ground state shows a quantum phase transition at some critical transverse field strength g_{crit}. For $g > g_{\text{crit}}$, the system is then in the ground state of the spin-x operator $|0_x\rangle = |\rightarrow\rangle = \prod_i \frac{1}{\sqrt{2}} (|\uparrow_i\rangle + |\downarrow_i\rangle)$, which constitutes a quantum paramagnetic state, whereas for $g < g_{\text{crit}}$, the system resembles the classical Ising model and has

a spontaneous symmetry breaking between the two eigenstates of the $\hat{S}^z$ operator: $|0_z\rangle = \prod_i |\uparrow_i\rangle$ or $|0_z\rangle = \prod_i |\downarrow_i\rangle$ and a non-vanishing magnetization in z direction $m_z \neq 0$.

Although the quantum critical point, being defined in terms of the ground state wave function, only exists precisely at $T = 0$, one can assess its properties inside the quantum critical region, which constitutes a fan in the phase diagram, extending to non-vanishing temperatures above the quantum critical point. The quantum critical fan of the transverse-field Ising chain is described in Ref. [82]: Both the ferromagnetic and paramagnetic phase have an excitation energy gap $|\Delta|$. In the ferromagnetic phase, the excitations are pairs of domain walls separating an intermediate section with opposite spin orientation from the rest of the chain (c.f. Ref. [83]), and in the quantum paramagnetic phase the lowest excitations are single-particle ones, which are realized by flipping one site from the state $|\rightarrow_i\rangle = \frac{1}{\sqrt{2}}(|\uparrow_i\rangle + |\downarrow_i\rangle)$ to the opposite eigenstate in x direction, namely $|\leftarrow_i\rangle = \frac{1}{\sqrt{2}}(|\uparrow_i\rangle - |\downarrow_i\rangle)$, compare Ref. [82] p.59ff.

Between these two regions lies the quantum-critical fan at temperatures $J \gg T \gg |g - g_{\text{crit}}|$. A sketch depicting the analogous situation for our models is found in Fig. 3.27. To understand the dynamical properties of the critical area, we need to introduce the thermal equilibration time τ_{eq}, which is defined as the time a system needs to return to local thermal equilibrium after a perturbation, compare e.g. Ref. [81]. In the quantum critical region, the system acquires the minimally possible equilibration time:

$$\tau_{\text{eq}}^{\text{qc}} = c_{\text{eq}} \frac{\hbar}{k_B T}$$

with some universal constant c_{eq}. The system in this state can hence also be called a perfect fluid[81]. Due to the diverging correlation length ξ at g_c, the system in the quantum critical region experiences thermal fluctuations at smaller length scales than it would "notice" the different coupling strength $g \neq g_c$, compare Ref. [81]. This effect is more prominent at large temperatures, causing the fan to widen for higher T. Inside the fan, the system behaves equally as for $g = g_c$. Quantum and thermal effects are then of the same order of magnitude and cannot clearly be disentangled. No effective classical model exists to describe the unique behavior of the system in this region, but instead it is mainly dominated by the influence of the critical point. To describe the properties of the QPT in a more quantitative way, we will assess its critical exponents in Sec. 3.6

3.4. Results for the model close to original GNRs

3.4.1. Spin ladders with realistic couplings

We will start the quantitative analysis for Hamiltonian H_1 with $\lambda = 1$, which is the model that represents a realistic nanoribbon with $U = t = 1$ and width $W = 10$, and we first regard the ferromagnetic order parameter (compare Eq. (3.9))

$$m_{\text{leg}} = \frac{1}{L}\sqrt{\sum_{i,j}\left\langle s_{iA}^z s_{jA}^z \right\rangle} = \frac{1}{3L}\sqrt{\sum_{i,j}\langle \boldsymbol{S}_{iA} \cdot \boldsymbol{S}_{jA}\rangle},$$

Due to the overall $SU(2)$ symmetry of the system, it is possible to reduce the whole magnetic order to the diagonal z basis (up to a factor $1/3$), which we can measure directly. Fig. 3.15 shows the result for different ribbons lengths as a function of temperature. For larger L the order parameter declines faster, and for the lengths used here we neither reach any saturation of this process, nor is there any finite temperature below which the reduction of order with growing length was smaller or even absent. Therefore, we conclude that the critical temperature is $T_{\text{crit}} = 0$ with no long-range ferromagnetic order at any finite temperature as for the freestanding Heisenberg chain.

To further investigate the stability of order in the low temperature limit, the leg susceptibility is used. This quantity is given by $\chi_{\text{leg}} = \int_0^\beta d\tau \left\langle \boldsymbol{S}_i(\tau) \cdot \boldsymbol{S}_j(0) \right\rangle$, and for its calculation by means of Monte-Carlo simulation—as explained in Sec. 3.1.3—the following expression holds:

$$\int_0^\beta \langle M_L(\tau) M_L(0) \rangle \, d\tau = \left\langle \frac{\beta}{n(n+1)} \left(\sum_{p=0}^{n-1} M_L(p) \right) \left(\sum_{p=0}^{n-1} M_L(p) \right) + \frac{\beta}{(n+1)^2} \left(\sum_{p=0}^{n} M_L(p) M_L(p) \right) \right\rangle \tag{3.23}$$

where p names the Monte-Carlo configuration in the different steps. The total number of steps is n.

If there was a phase transition to a phase with long-range ferromagnetic order along one leg, the single leg susceptibility should diverge at the corresponding critical temperature $T_{\text{crit}} > 0$ (compare e.g. Ref.[82]). Consequently, plotting the inverse leg susceptibility, as done in Fig. 3.15 on the right, should give the critical temperature as root. Since the longer system sizes show smaller values of $1/\chi_{\text{leg}}$ and the overall results are extremely close to zero already around $T = 0.1$, one might be tempted to find a critical temperature of roughly $T = 0.1$ or even $T = 0.2$ here, just by a linear fit to the low-temperature behavior. However, a very similar situation arises when we repeat the above plot for the freestanding Haldane-Shastry chain, compare Fig. 3.16.

For the free chain it has been proven analytically that the critical temperature is $T_{\text{crit}} = 0$, using Bethe ansatz calculations (Ref. [37]). So we must conclude that linear extrapolation of the inverse leg susceptibility is not a suitable method to find the critical temperature of a system, at least for system sizes available to our SSE calculations. Firstly, the values are especially vulnerable to finite-size effects near the divergence at T_{crit} and secondly, the inverse does not behave linearly in the critical region.

Finally, we test the uniform susceptibility Eq. (3.10). As stated above, it has a finite value $\chi_{\text{uni}}(T \to 0) \neq 0$ if the system is in a spin gapless phase. Fig. 3.17 displays such a plot for different ribbons lengths. While the concave down-bending for small temperatures is a finite size effect that decreases for larger L, it becomes obvious that in the thermodynamic limit $\chi_{\text{uni}}(T \to 0) \sim 0.11 > 0$ and hence the system does not have a spin excitation gap.

From these results we conclude that for a realistic nanoribbon with $M \gtrsim 8$ unit cells the edge magnetic moments are in a gapless, weakly ordered phase. In the thermodynamic limit, however, and at the critical point $T = 0$, we expect a ferromagnetic polarization within each leg,

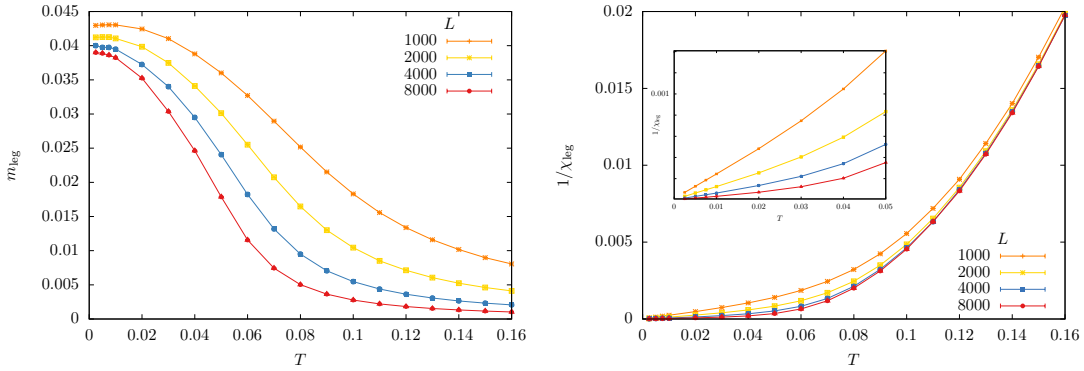

Figure 3.15.: Left: The ferromagnetic order in Model 1 with $\lambda = 1$ (corresponding to $M = 10$ unit cells and $U = t = 1$) decreases with increasing temperature. The longer the ribbon length, the earlier this decrease occurs, and we cannot reach any saturation. Right: The inverse leg susceptibility for the same ribbon decreases to very small values as $T \to 0$. However, as one can see in the inset, the descrease is not lineare close for very small temperatures, and $1/\chi_{\mathrm{leg}}$ does not reach exactly 0 for any finite temperature.

with opposite direction for the two legs. For wider nanoribbons, the antiferromagnetic inter-leg couplings of the effective ladder model will be further reduced as compared to the ferromagnetic intra-leg couplings, so that even more clearly the effective spin model resides within the gapless regime. For wide zigzag nanoribbons, the quantum disordered region is reached only upon artificially enhancing the inter-leg coupling beyond a critical coupling value. This will be the topic of the next section.

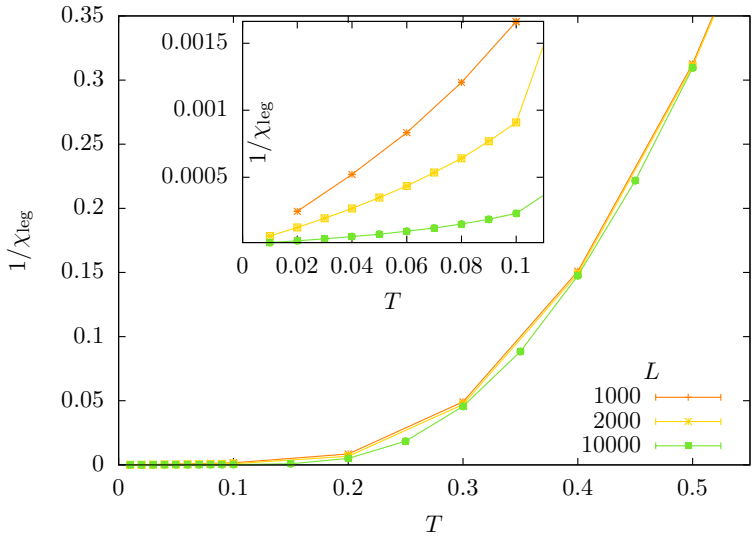

Figure 3.16.: The inverse leg susceptibility for the ferromagnetic Haldane-Shastry chain seemingly vanishes for a finite $T_{\mathrm{crit}} > 0$. This must be a finite size effect, since it would be in contradiction to analytic results (e.g. Ref.[37]).

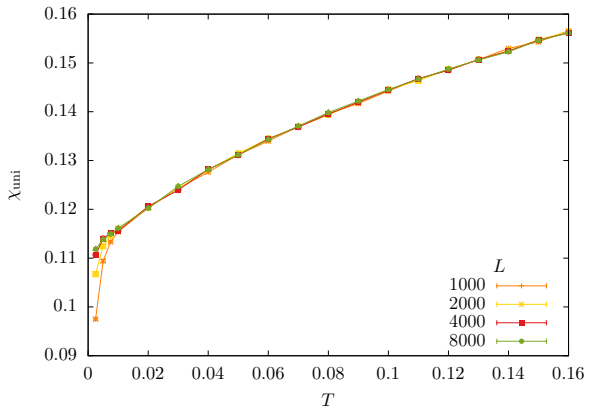

Figure 3.17.: The uniform susceptibility of a system from Model 1 for $\lambda = 1$ tends to a non-vanishing values for $T \to 0$. The down-bending for small systems is a finite size effect, which will vanish as $L \to \infty$.

3.4.2. Quantum phase transition for large λ

We have already defined above the scaling parameter λ (Eq. (3.18)), which rescales all the antiferromagnetic couplings, and we shall test here the transition to a strong-interleg-coupling regime. It seems plausible that the weak ferromagnetic order from the $\lambda = 1$ phase is destroyed at higher antiferromagnetic coupling strengths. Figure 3.18 displays the uniform susceptibility (compare Eq. (3.10)) for a ribbon length of $L = 8000$ spins and for different scaling factors λ. There is a qualitative change in the graphs: For $\lambda < 3.45$ the curve extrapolates to a finite y-axis intercept, $\chi_{\mathrm{uni}}(T \to 0) > 0$ (up to a down-bending due to finite-size effects), whereas for $\lambda \gtrsim 3.45$ the curve is convex and reaches $\chi_{\mathrm{uni}} = 0$ for a non-vanishing temperature. This stark difference in the behavior resulting from a relatively small change in the parameter λ is an indication for a quantum phase transition in the thermodynamic limit. Furthermore, when looking at constant coupling values and different system lengths, we see a qualitatively different thermodynamic limit between the two expected phases, compare Fig. 3.19.

Another quantity that shows a significant qualitative change at a small variation of J_{AF} in the estimated critical range is the single-leg susceptibility Eq. (3.11). χ_{leg} is a measure for the fluctuations in the magnetic moment along one leg, where the results for either leg are equal in our model. This quantity is not per se diagonal with respect to our Hamiltonian, but the Kubo integral can be determined as described in Sec. 3.1.3 (last paragraph). We make use of the $SU(2)$ symmetry of the system, which allows us to calculate the magnetizations in the S^z basis. In Fig. 3.20 it is visible that the leg susceptibility diverges as $T \to 0$ in the weak coupling phase. This is in accordance with the picture of a critical temperature $T_{\mathrm{crit}} = 0$ for the long-range order along the legs. However, the fundamentally different behavior for $\lambda \gtrsim 3.5$ is discernible: In the strong-coupling phase, the single leg susceptibility remains strictly finite as the temperature vanishes. Naturally, genuine divergence cannot be achieved in a system of finite length, and in the weak-coupling phase the graphs are therefore especially affected by finite-size effects. But an analysis of the development upon increasing the system size for constant values of λ in the two different phases (compare Fig.3.21) supports the above conclusions: For λ in the weak-coupling phase, there is a significant increase of divergence at growing system sizes, whereas for large enough λ to be in the rung singlet phase, a saturation at finite χ_{leg} is reached.

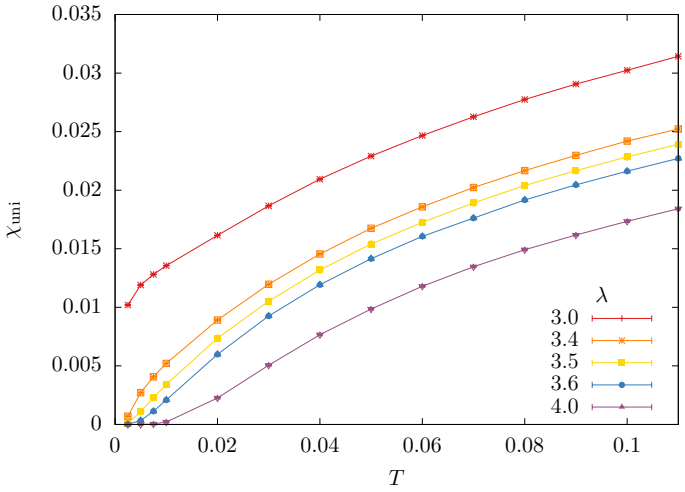

Figure 3.18.: The uniform susceptibility of Model 1 for different values of the parameter λ, enhancing the antiferromagnetic couplings as $J^{\mathrm{AF}} \to \lambda J^{\mathrm{AF}}$. The system length is $L = 8000$.

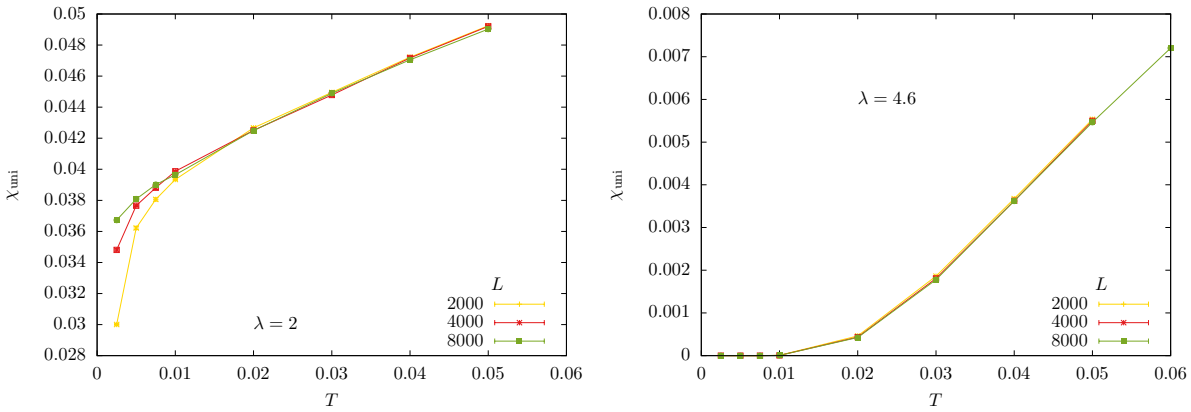

Figure 3.19.: The uniform susceptibility of Model 1 in the weakly ordered phase $\lambda = 2$ (left) and in the spin singlet phase $\lambda = 4.6$ (right) exhibit a qualitatively different change when the system length is varied.

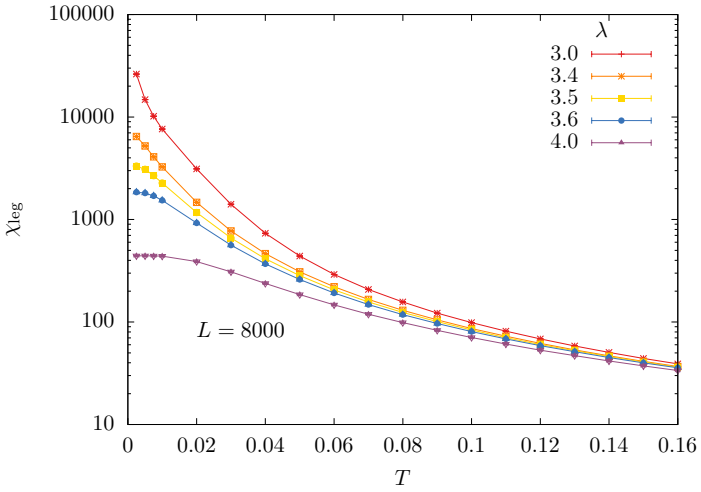

Figure 3.20.: The single leg susceptibility for Model 1 as a function of temperature for different coupling parameters λ at $L = 8000$

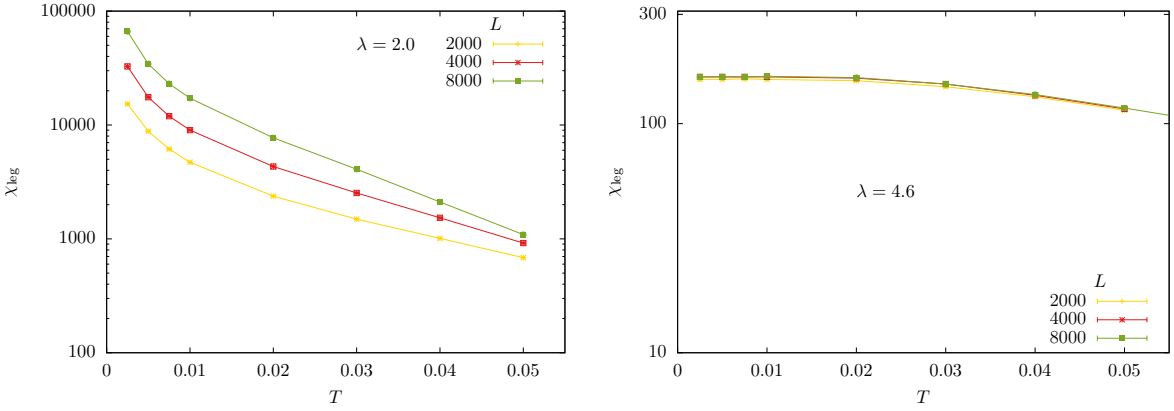

Figure 3.21.: The dependence of χ_{leg} on the temperature for different system lengths, comparing $\lambda = 2$ (left) and for $\lambda = 4.6$ (right), respectively. Please mind the different scales of the y-axes.

Finally, we should directly regard the spin correlations inside the legs of the ladder system. For this purpose, we introduce the quantity

$$C\left(r_{ij}\right) = \left\langle s^z_{i\mu} s^z_{j\mu} \right\rangle , \tag{3.24}$$

where $\mu \in \{A, B\}$ give equal results. We now regard a mapping

$$r \to \zeta = \frac{L}{\pi} \sin\left(\frac{\pi}{L} r\right) \ ,$$

under which the correlation function transforms covariantly (compare Ref. [84]) at the critical point. This maps the correlation function on the infinite one-dimensional system to the same quantity measured on a ring, i.e. with periodic boundary conditions. Originally, such conformal mappings were invented to map an infinite two-dimensional system on a cylinder geometry. It can however also be used for one-dimensional systems[84] if the second dimension is interpreted as the inverse temperature $1/T$. The quantity $\langle s^z_0 s^z_r \rangle (\zeta)$ for different rung couplings—as shown in Fig.3.22—also reveals a change in behavior close to the phase transition: While for weaker rung couplings the correlation decays slower than a power law, it becomes linear in a double logarithmic scale for

$$\lambda_{\text{crit}} \approx 3.45 \ ,$$

and it decays faster than a power law for yet stronger leg couplings. Near the critical point, the correlation function shows a power law behavior

$$C\left(\zeta\right) \propto \zeta^{-1/2} \tag{3.25}$$

Such an algebraic scaling behavior of the finite-system's correlation function in terms of the conformal distance is characteristic for the decay of the correlation function at a quantum critical point, with an emerging conformal invariance in $1+1$ dimensional quantum systems. For comparison, regard again the pure short-ranged transverse-field quantum Ising chain $H_{\text{Ising}} = -Jg \sum_i s^x_i - J \sum_{\langle i,j \rangle} s^z_i s^z_j$ as described e.g. in Ref. [82] (p. 10 ff.): For $g \gg 1$, the system is then in the ground state of the spin-x operator $|0_x\rangle = \prod_i \frac{1}{\sqrt{2}} \left(|\uparrow_i\rangle + |\downarrow_i\rangle\right)$, and the correlation between two sites decays exponentially: $\left\langle 0_x \left| s^z_i s^z_j \right| 0_x \right\rangle \propto e^{-r_{ij}/\xi}$ with the correlation length ξ, which at $r \to \infty$ fulfills $\xi \to 0$, so that two different states are completely uncorrelated in that limit.

In the opposite limit $g \ll 1$, the system is ordered. and the correlation function converges to a constant value: $\lim_{r_{ij} \to \infty} \left\langle 0_z \left| s^z_i s^z_j \right| 0_z \right\rangle = N_0^2$ with the spontaneous magnetization N_0. Between these two phases, there is a quantum phase transition where ξ diverges, and right at criticality $g = g_c$, the long-range correlation function exhibits a pure power-law decay. This corresponds to our case Eq. (3.25), only with the conformal distance ζ instead of the direct distance r.

Finally we aim at determining a correlation length ξ for the disordered spin-singlet phase, as the spin correlations for long distances must decay exponentially in the disordered regime. However, due to the long-range interaction of the model, i.e., the fact that the couplings decay only with x^{-2}, these long-range correlations are assumed to prevail even in the disordered regime,

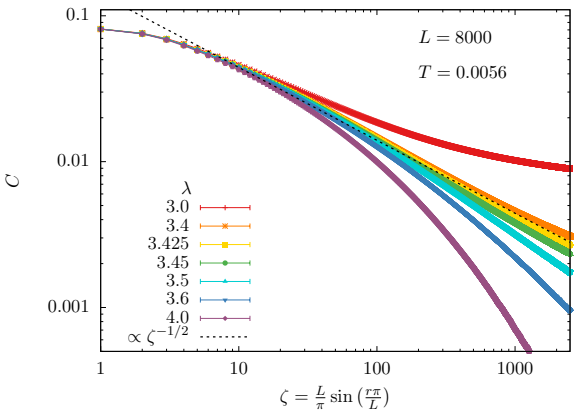

Figure 3.22.: The spin-spin correlation function $C(r) = \langle s_0^z s_r^z \rangle$ as a function of the conformal distance for different scaling parameters λ for fixed small temperature and large system size. The dashed line represents algebraic decay with exponent $-\frac{1}{2}$.

independent of the exponential decay. We expect the correlations $\mathcal{C}(r) = \langle s_i^z s_{i+r}^z \rangle$ described in terms of the conformal length to follow the function

$$\mathcal{C}(r) = \frac{c}{r^2} \cdot \left(1 + \exp\left(-\frac{r}{\xi}\right)\right) \tag{3.26}$$

with the correlation length ξ of the exponentially decaying portion. In Fig. 3.23 one sees a corresponding fit for a long ribbon at small temperature and $\lambda = 6$. Even with such a large value of λ, however, the fit turns out to be cumbersome, because we somewhat arbitrarily have to determine where the long-range part begins, and moreover the correlations become extremely small and therefore affected by numerical uncertainties for very large distances. After all, this gives a rough estimate for the correlation length to be

$$\xi \approx 770 \text{ unit cells}$$

Such a quantum phase transition as we found here is a change between two different phases—usually an ordered and a disordered one—at $T = 0$, depending on a different scaling parameter than the temperature. In our case that driving scaling parameter is the factor λ, with which the antiferromagnetic couplings are multiplied. Quantum phase transitions feature many interesting properties, especially multiple scaling exponents that describe the behavior of corresponding quantities near criticality. For more details on this, compare Sec.3.6.1. In the following chapter, we will go over to an even more abstract and generic model, for which we will then also analyze the quantum critical point in more detail and access its critical exponents.

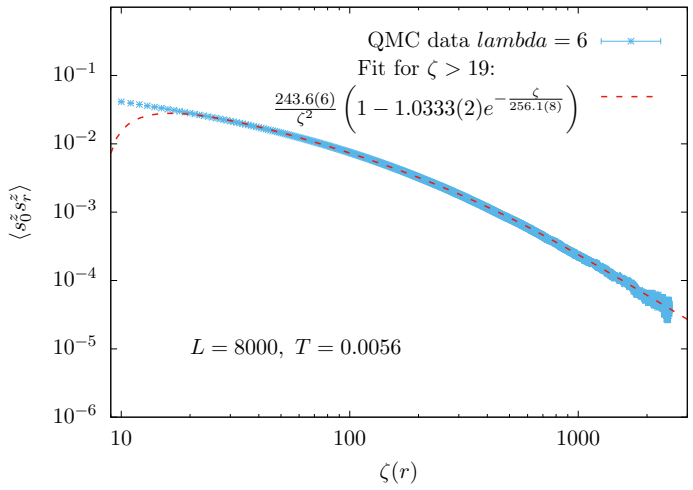

Figure 3.23.: A fit of the spin correlation to Eq. (3.26) for a system with H_1 and $\lambda = 6$ gives an estimate for the correlation length. The fit gives a $\chi^2/\text{ndof} \approx 56$.

3.4.3. Very narrow ribbons

Explicit Monte-Carlo simulations on the lattice for an extremely narrow ribbon $W = 2$ have found a ground state in the disordered singlet phase, compare Ref.[12]. For those models it was not possible to look at broad ribbons, because such a simulation on the ribbon is numerically very costly. However, simulations at slightly larger widths support the idea that a phase transition to the ordered ground state as a function of ribbon width takes place.

Starting on the other hand from the rather broad ribbons $W = 10$ with the ordered ground state in our effective model, we try to assess the situation for smaller W. However, the effective spin model is certainly not an ideal approximation for $W < 8$, because the small parameter of the final perturbation theory for the antiferromagnetic couplings becomes larger with decreasing width, until the prerequisite

$$\frac{t^*}{U\Gamma^{xxxx}} \ll 1$$

is no longer strictly fulfilled. The case $W = 6$ with $J^{\mathrm{AF}}(0) \sim 0.1$ is a borderline case, where the effective model might not be as accurate as possible, but can still be used in a reasonable way. The cases $W = 6$ and $W = 8$ are embedded in the Hamiltonian H_1 in the same way as for $W = 10$; the couplings for $r \leq 4$ are given in Tab.(3.2) . Please bear in mind that these values are each multiplied with a lattice specific constant to guarantee $J^{\mathrm{F}}(1) = 1$ in both cases again.

From the fittings, the prefactors for the ferromagnetic case are $J^{\mathrm{F}} = 0.01580$ for $W = 6$, and $J^{\mathrm{F}} = 0.0141302$ for $W = 8$, respectively. The antiferromagnetic long-range interactions start from $J^{\mathrm{AF}} = 0.21239$ for $W = 6$, and $J^{\mathrm{AF}} = 0.217806$ for $W = 8$.

$r\,(W=6)$	$J^{\mathrm{F}}(r)$	$J^{\mathrm{AF}}(r)$
0	-	0.0970285
1	−0.0458957	0.0624986
2	−0.0054591	0.0175084
3	−0.0020787	0.0028995
4	−0.0011801	0.0006433

$r\,(W=8)$	$J^{\mathrm{F}}(r)$	$J^{AF}(r)$
0	-	0.0403467
1	−0.0454998	0.0295818
2	−0.0049477	0.0120777
3	−0.0016538	0.0032023
4	−0.0009013	0.0007934

Table 3.2.: The short-range couplings (before scaling) for the two ribbons 6×2402 unit cells (left) and 8×2402 uni cells (right), respectively.

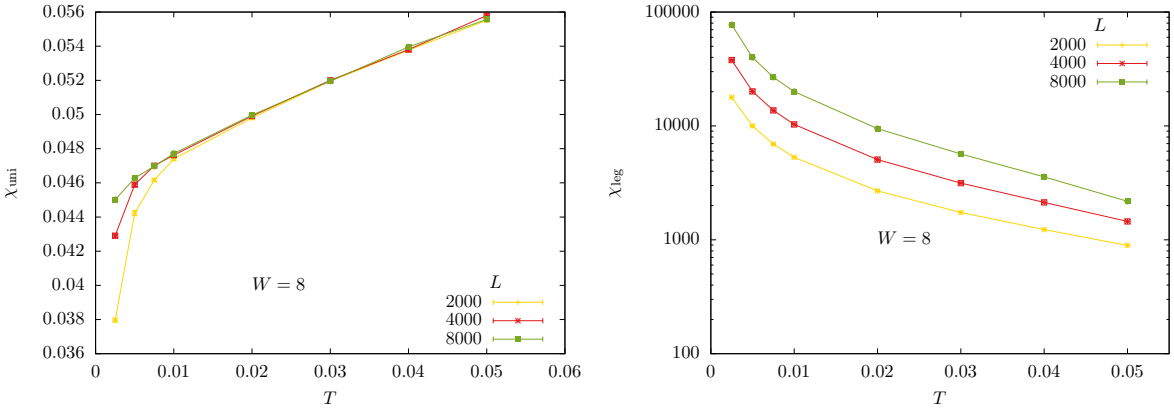

Figure 3.24.: Uniform and chiral susceptibility for different lengths at the rather narrow ribbon $W = 8$.

For the width $W = 8$ at the natural parameter $\lambda = 1$, one is apparently still in the ferromagnetic weak ordered phase, as the development of both susceptibilities with different L display in Fig.3.24.

However, for the narrow ribbons $W = 6$ we clearly find the ground state to be the disordered rung-singlet state, with even more pronounced features than for the "artificial" $W = 10$ and $\lambda = 4$. As presented in Fig.3.25, the leg susceptibility is fully saturated, and the uniform susceptibility nearly vanishes already at $T = 0.02$.

For a system that is so deep in the disordered phase, the exponential decay of the correlation function should be pronounced also for medium distances. Figure 3.26 shows a fit of the medium- to long-range spin correlations as a function of the conformal length ζ to the behavior: $\mathcal{C}(\zeta) = \frac{c}{\zeta^2} \cdot \left(1 + ae^{-\zeta/\xi}\right)$. The result for the correlation length from that fit is

$$\xi \approx 84.9 \text{ unit cells},$$

where we have taken into account that roughly three unit cells host one edge electron in the Wannier basis. This is larger than the correlation length $\xi = (15 \pm 4)$ unit cells determined in Ref.[12] for a ribbon with $W = 4$ and $L = 54$, which fits well in the picture of a dominating short-range decay for very narrow ribbons with diverging correlation length as W is increased.

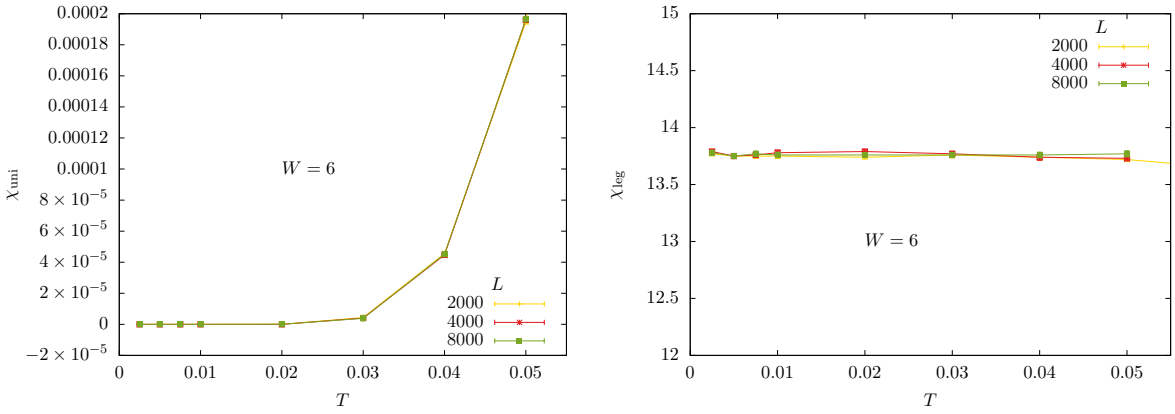

Figure 3.25.: Uniform and chiral susceptibility for different lengths at the narrow ribbon $W = 6$. Note that the y-axis is linear also for the χ_{leg}.

Although the effective model is less precise for $W = 6$, these findings strongly suggest that the ground state of graphene nanoribbons can be tuned from the antiferromagnetic disordered state for very narrow ribbons to the weakly ordered state for $W \geq 10$. This is in accordance with the findings from lattice QMC simulations[12]. It would indeed be ideal to have a method at hand that can calculate both, very narrow and also broad ribbons, to be able to test this promising result.

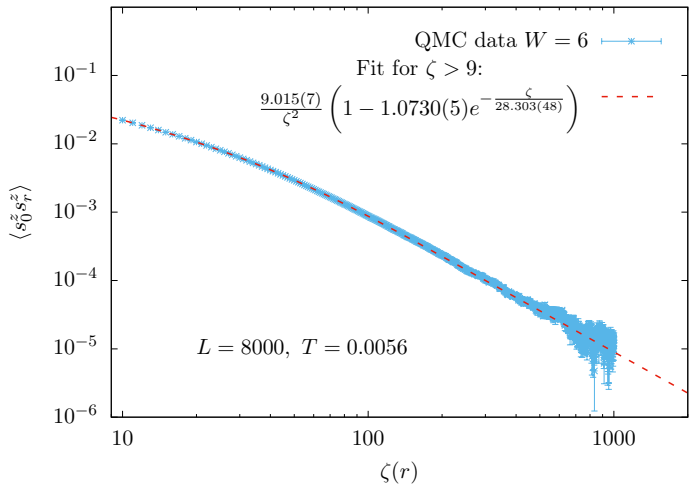

Figure 3.26.: The spin correlations as a function of the conformal length for $W = 6$. The fit gives $\chi^2/\text{ndof} \approx 5$.

3.5. Results for the generic spin ladder model

We will now analyze in more detail the model described by the Hamiltonian from Eq. (3.17):

$$H_2 = -J^{\mathrm{F}} \sum_{i,j} \frac{1}{r_{ij}^2} \left(\boldsymbol{S}_{i,1} \cdot \boldsymbol{S}_{j,1} + \boldsymbol{S}_{i,2} \cdot \boldsymbol{S}_{j,2}\right) + J^{\mathrm{AF}} \sum_i \boldsymbol{S}_{i,1} \cdot \boldsymbol{S}_{i,2} \ ,$$

which represents a set of two ferromagnetic chains with long-range interaction, coupled by a direct antiferromagnetic rung coupling. We have again fixed $J^{\mathrm{F}} = 1.0$, and the free scaling parameter driving the phase transition here is

$$g = \frac{J^{\mathrm{AF}}}{J^F}$$

Qualitative differences between gapped and gapless phase One of the easiest and most prominent models with long-range interaction in a spin system is the Haldane-Shastry chain[35, 36], a single spin-1/2 chain with long-range couplings $J \propto 1/r^2$. This model is exactly solvable and does not have a spin excitation gap neither in the anti-ferromagnetic[35, 36] nor in the ferromagnetic [37] case. For a negative, ferromagnetic coupling, this model exhibits a long-range order only at the critical temperature $T = 0$, while for any non-vanishing temperature long-range order is forbidden by the Mermin-Wagner theorem[20]. Consequently, the susceptibility diverges[37, 85] at the critical temperature $T = 0$. We have briefly tested this in Fig.3.13 and found the results confirmed, though with a limited accuracy in the region of very small T.

In contrast to this, in a conventional short-range Heisenberg ladder (as discussed in Sec. 3.2) with ferromagnetic leg coupling, long-range order at $T = 0$ is destroyed by an arbitrary small

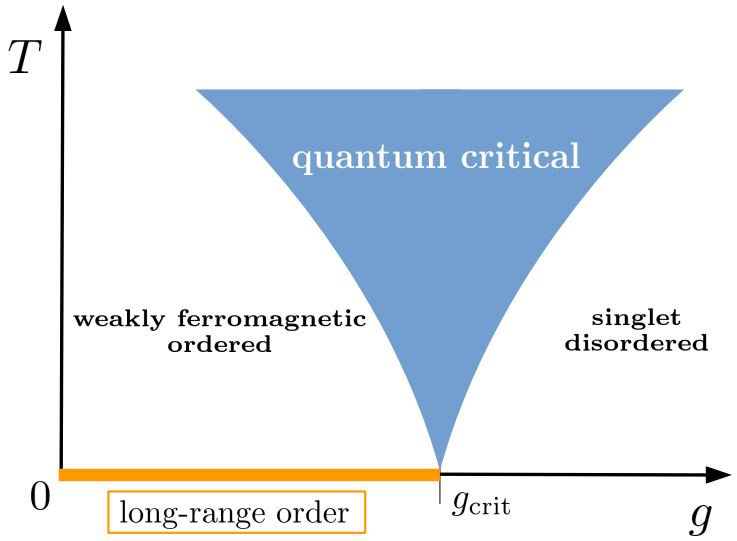

Figure 3.27.: There is a phase transition between a weakly ordered leg ferromagnetic phase for small g and a disordered rung-singlet phase for large g, and hence large rung couplings. The long-range ferromagnetic order only occurs for $T = 0$, in agreement with the Mermin-Wagner theorem.

antiferromagnetic rung coupling and the system is in a rung-singlet state for any $J^{\mathrm{AF}} > 0$. The ladder then does have a spin excitation gap, i.e., the energy of the first excited state lies at a finite non-vanishing value above the ground-state energy for any momentum k, so that $\Delta = \min\left(E_1\left(k\right)\right) - E_0$. In the disordered rung-singlet phase, the susceptibility goes to zero in the ground state and thermodynamic limit.

Fig. 3.27 presents a sketch of the phase diagram of our spin-ladder models at low temperature and shows the quantum critical fan as described in Sec. 3.3.4

Uniform susceptibility In analogy to the more realistic model regarded in Sec. 3.4.2, at stronger rung coupling also this simplified model has a quantum phase transition from the gapless weakly ordered phase to a gapped rung-singlet phase. This is undermined by the behavior of the uniform susceptibility[73] Eq. (3.10) $\chi_{\mathrm{uni}}\left(T\right) = \frac{1}{T} \cdot L \left\langle m^2 \right\rangle$ as shown in Fig.3.28 for different values of the antiferromagnetic coupling. The down-bending of the graph near $T \to 0$ for small J^{AF} is again a finite size effect. In Fig.3.29, we compare the behavior for increasing lengths for different system sizes.

While for $g = 1.94$ and $g = 1.95$ the values of χ_{uni} grow with growing system sizes at small temperatures, they tend to saturate for $g = 1.96$ and $g = 2.0$, larger than the critical coupling. For $g = 1.95$ there is a qualitative change as the system size increases. The apparent convex bending of the graph can in part be attributed to the fact that values smaller than zero (which would be required to continue the concave finite-size bending) cannot be reached and the connecting lines then indicate a wrong course. However, the graph for $g = 1.95$, $L = 1000$ still displays a convex

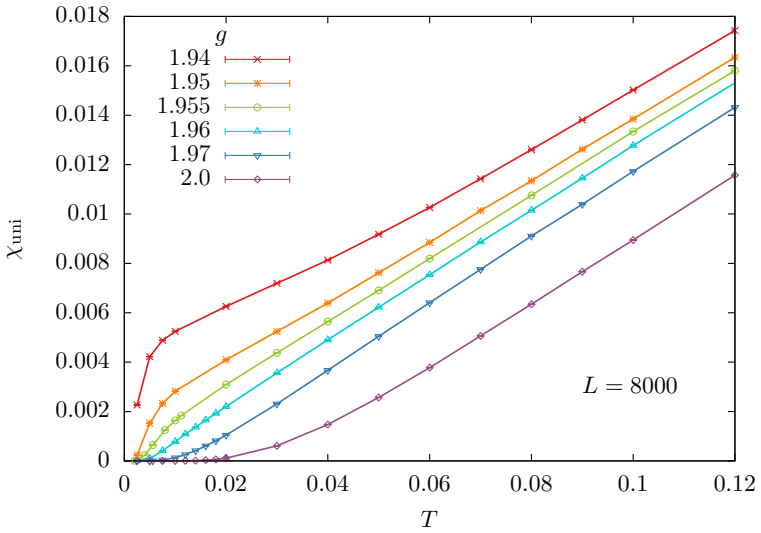

Figure 3.28.: The uniform susceptibilities as a function of temperature for different antiferromagnetic rung coupling strength show qualitatively different characteristics for smaller versus stronger coupling parameter. The concave bending of the $g = 1.94$ and $g = 1.95$ lines for very small temperatures are finite size effects, see Fig. 3.29. The system length is $L = 8002$ sites including Ewald summation (compare Sec. 3.3.3).

bending due to finite size effects, and hence this small system deviates from the termodynamic limit behavior. Nevertheless, we see that the behavior also for much larger L significantly and systematically changes as expected. So it can be concluded that in the thermodynamic limit, the susceptibility for weak rung couplings will show a finite axis intercept. The system is then in a phase without excitation gap. In contrast, at strong coupling values the system has a vanishing $\chi_{\mathrm{uni}}(T \to 0) = 0$, which is not a finite size effect. In analogy to the model with H_1 in Sec. (3.4.2), such a change in the qualitative behavior which occurs at only very small variation of the coupling parameter g indicates a quantum phase transition, and the critical value is found to be

$$1.95 \lesssim g \lesssim 1.96$$

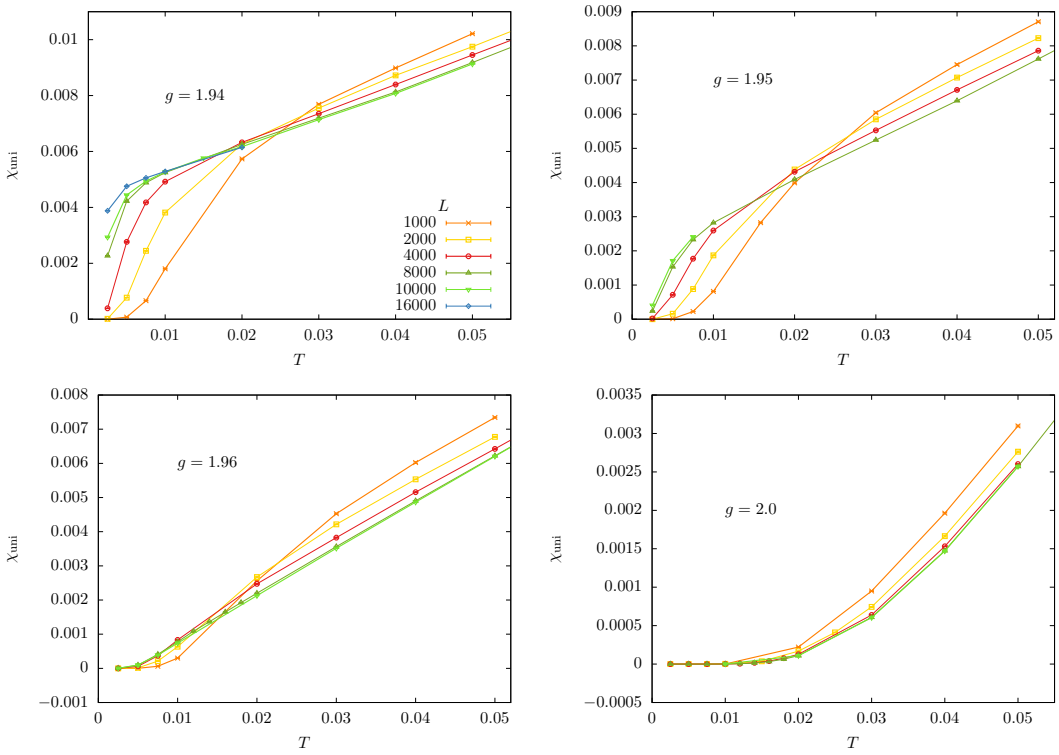

Figure 3.29.: The uniform susceptibility as a function of temperature for different system sizes. The legend applies to all plots, with the line for $L = 16000$ only present in the first plot. Please consider the different ranges of the y-axis. As L increases, the system tends towards the thermodynamic limit behavior.

Single leg susceptibility For a finite rung coupling, the single leg susceptibility, too, displays a qualitative difference between smaller and larger coupling values g (compare Fig. 3.30, left). The leg susceptibilities diverge in the ordered phase, analogous to the situation in the pure chain with long-range interaction, because the ferromagnetic order is not stable and has a critical temperature of $T = 0$. In contrast, χ_{leg} has finite axis intercepts in the rung-singlet phase. This quantity undermines that the critical coupling strength is $1.95 < g_{\text{crit}} < 1.96$. As we will confirm later, the point $T = 0.025$, $g = 1.95$ is affected by finite-size effects, and the line should in fact continue to be convex for $T \to 0$ instead of showing a tendency to saturate. All in all, this quantity is less affected by finite-size effects than the uniform susceptibility Fig. 3.28, but it is also worth to compare different system lengths.

The qualitative differences are well seen when regarding the different L, as shown in Fig.3.31. The total values for $\chi_{\text{leg}}\,(T \to 0)$ still depend on the system size, and naturally true divergence in the gapless phase cannot be realized in a finite system. However, one sees the clearly different behavior in the two phases: In the ordered phase, the divergence at $T \to 0$ becomes more pronounced for larger system sizes, while in the disordered phase the values for χ_{leg} decrease with increasing system size.

To assess the precision of our calculation, the behavior of the susceptibility can be compared to known analytical findings in the case $g = 0$. From the above-mentioned ferromagnetic Haldane-Shastry model[37, 86] it is known (compare Eq. (16) in Ref.[37]) that the chain susceptibility diverges exponentially as the temperature goes to zero. The expression can be calculated exactly using Bethe ansatz, and it has been found that:

$$\begin{aligned} \chi\,(T \to 0) &= \frac{1}{4}\frac{\beta}{\sqrt{\beta\,|J|\,\pi/2}}\exp\left(\beta\,|J|\,\frac{\pi^2}{8}\right) \\ \to \chi &= \frac{c}{\sqrt{T}}\exp\left(\frac{a}{T}\right) \\ \Rightarrow \ln\left(\chi\sqrt{T}\right)\cdot T &= \ln(c)\cdot T + a \end{aligned} \tag{3.27}$$

Therefore, plotting $\ln\left(\chi\sqrt{T}\right) T$ as a function of T for the pure Haldane-Shastry chain (i.e. $g = 0$) should give a linear graph with the slope $\ln(c) = \ln\left(\sqrt{\frac{1}{8\pi}}\right) \approx -1.61$ and the axis intercept $a = \frac{\pi^2}{8} \approx 1.23$. Fig. 3.30 (right) shows the results for a corresponding QMC simulation along with a fit to Eq. (3.27) using only the high-temperature data points. The errors of the fit parameters are slightly too small to meet the Bethe ansatz result, but the values fit with a reasonable precision. For $T < 0.2$, however, the simulation results severely deviate from the analytically confirmed behavior, which we attribute to finite size effects. The corresponding data points have not been used for the fit process. For the pure chain even with very large L it is hence not possible to reach the ground state behavior with a reasonable computational effort. Luckily, as already outlined in Sec. 3.3.3, the finite size effects are in fact a lot less problematic for the coupled chains, at least in the range $g \sim \mathcal{O}(1)$ that we are interested in for the quantum phase transition. However, we still do not aim at reproducing the ground-state behavior in the thermodynamic limit. Instead, in the next chapter we will try and assess the critical exponents of said quantum phase transitions by analyzing the finite-size scaling behavior of the interesting quantities.

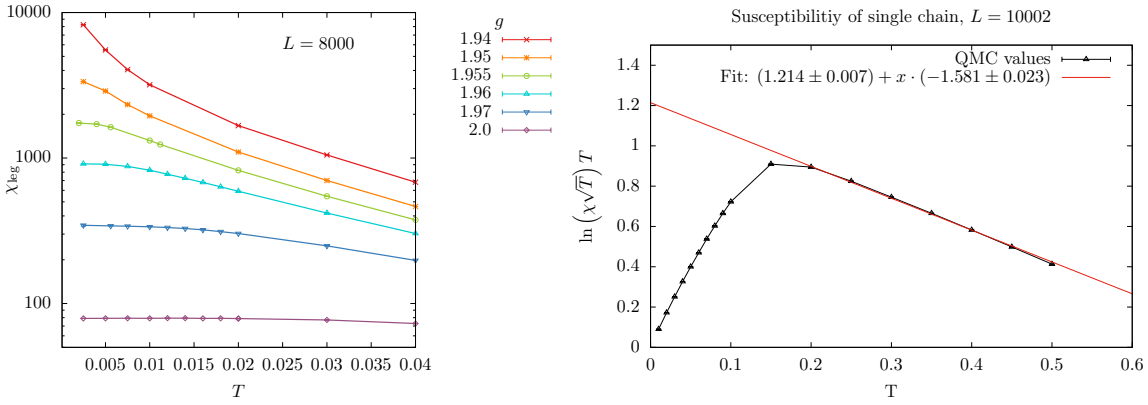

Figure 3.30.: Left hand side: The susceptibility of a single leg for coupled chains with $L = 8002$ and different rung coupling strengths as a function of temperature. Right hand side: Susceptibility of a pure chain for $L = 10002$, not including Ewald summation. The red line is a fit to the analytic result Eq. (3.27) (not including points with $T < 0.2$).

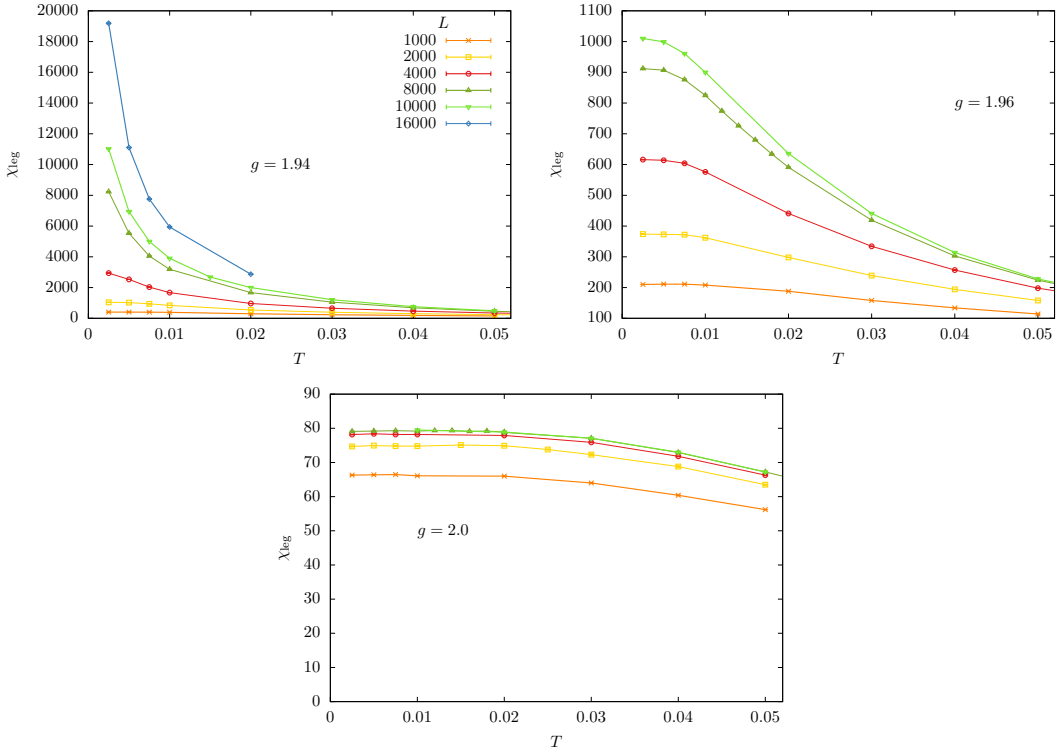

Figure 3.31.: The leg susceptibility for a leg coupling below (left), slightly above (middle), and well above (right) the critical value g_{crit}. One should mind the different ranges for the y axes. The legend holds for all plots.

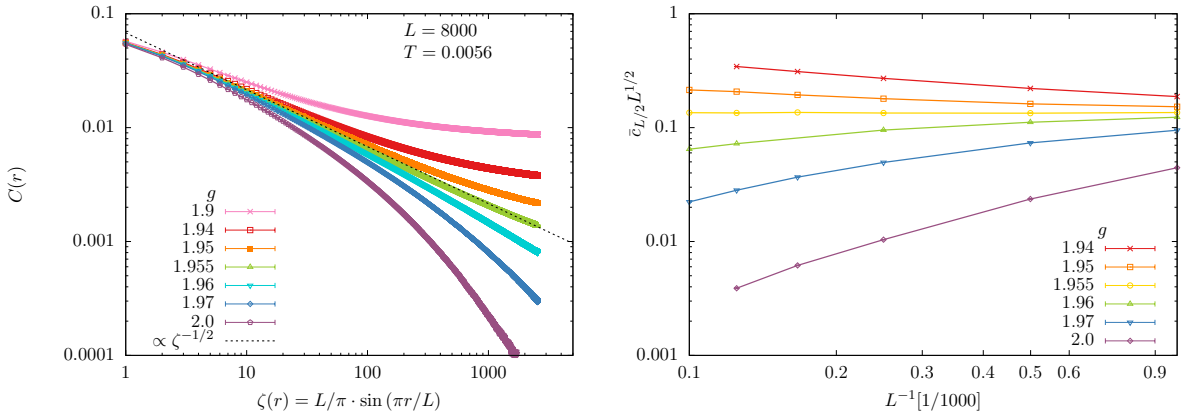

Figure 3.32.: Left: The correlation function $C(r) = \langle S_0^z S_r^z \rangle$ as a function of the conformal distance ζ shows approximately a power law decay for $g = 1.955$. Right: When scaled accordingly, he long-distance correlation $c_{L/2}(L/2)$ becomes flat at criticality.

Behavior of the correlation function Before going over to the finite-size scaling analysis, we look again at the correlation function along the legs, which constitutes a more direct measure of the actual spin configurations, as compared to the susceptibilities. As presented in Fig. 3.32, we find again a qualitative change in the curvature, and the critical value

$$g_{\text{crit}} \approx 1.955$$

is confirmed. At this coupling strength, the long-distance spin correlations follow an algebraic decay with $C(\zeta) \propto \zeta^{-1/2}$ indicative of a quantum critical point.

To better exclude fluctuation effects and short-range behavior, we also measured the spin correlation to the most distant sites along the ladder $c_{L/2} = \overline{\left\langle S_0^z S_{L/2}^z \right\rangle}$, where the over-line denotes the average over l_C lattice sites. We choose $l_C = 0.01L$. If the equal-time correlation function at criticality decays with distance with a power law with exponent z, then

$$G(r) \propto \frac{1}{r^z} \qquad \Rightarrow c_{L/2} \propto \left(\frac{L}{2}\right)^{-z} \qquad \text{for } g = g_{\text{crit}}, \quad r \gg 1,$$

This quantity as a function of system size for different rung couplings behaves in accordance with the above results: It follows a power-law decay close to the critical point, for stronger couplings it decays faster than that. The exponent z is called the dynamical critical exponent, it is related to correlations in the temporal direction, and mean-field calculations find $z_{\text{MF}} = 1/2$ (Ref. [87]). For a more detailed explanation, compare Secs. 3.6.1, 3.6.2. When scaling the y axis with $z = 1/2$, a flat linear behavior is displayed at criticality, compare Fig. 3.32, right. The slow algebraic decay at criticality is different from the asymptotic $1/r^2$ decay in the large-g region. The latter one originates from the explicit ferromagnetic couplings decaying as $1/r^2$.

3.6. Quantum critical properties

3.6.1. Scaling and critical exponents

It is important to show that the above determined quantum phase transition is not a finite size effect. In a worst case scenario, the exactly known Haldane-Shastry phase might already be destroyed for an infinitely small inter-leg coupling—as it is the case for the short-ranged Heisenberg ladder—and all remaining order could be just a result of the limited system length. To disprove this presumption, we analyze the scaling of the ferromagnetic and staggered order parameters as well as the susceptibilities as functions of system length.

The finite size scaling method aims at determining the bulk properties of a system, i.e., the properties in the limit of infinitely large systems, from the quantities that can be calculated in finite systems of different lengths L. The relations used to find the critical exponents can be derived for example with methods from renormalization group[80, 88] (compare also Sec.3.6.2). Second-order phase transitions only show their true critical exponents and singularities in the thermodynamic limit. With simulation methods such as quantum Monte Carlo, one is naturally limited to systems of finite extend $L_1, L_2,$ ... in all dimensions.

Whether this makes a difference in the results depends on the ratio of L compared to the correlation length ξ of the system: The genuine thermodynamic limit behavior is only simulated if $L \gg \xi$. For systems with short-range interactions, the correlation length is often defined via the exponential decay of the equal-time order parameter correlation function $\propto \exp(-r/\xi)$. In our case, we can refer to the connection between ξ and the spin gap Δ: When reaching the critical coupling strength from above, the characteristic energy scale vanishes[82] as

$$\Delta \propto \xi^{-z}$$

with the dynamical critical exponent z (compare Sec. 3.6.4). Upon reaching criticality—be it near quantum critical or a classical critical point—the correlation length diverges. In the Ising model[66] and many related systems, ξ diverges with a power law, and the critical exponent ν is defined as the scaling of the correlation length near criticality[80], so in our case

$$\xi \propto |g - g_{\mathrm{crit}}|^{-\nu} \tag{3.28}$$

Due to this divergence, for simulations near criticality we will mostly encounter the case $\frac{L}{\xi} < 1$ and we will not be able to measure the correct thermodynamic limit behavior directly. Instead, the scaling behavior will be altered by the influence of the system length L, as the findings in Sec. 3.3.3 confirm. In detail, the susceptibility is multiplied with a scaling function that depends on the ratio L/ξ. To derive the genuine behavior in the thermodynamic limit, one can resort to the so called finite size scaling and compare the results for different finite system sizes L_i. The following short derivation has been taken from Refs. [66] and [89]. As an example, we regard the susceptibility χ per spin at zero temperature. In the infinite system near the critical point, this quantity should scale as

$$\chi \propto \xi^{\gamma/\nu} \ , \tag{3.29}$$

but due to the limited system size, this is altered to

$$\chi = \xi^{\gamma/\nu} \cdot \chi_0 \left(\frac{L}{\xi} \right)$$

with some scaling function χ_0, which is not known precisely, but which must fulfill $\chi_0(x) = \text{const.}$ for $x \gg 1$. We define another dimensionless auxiliary function $\bar{\chi}(x) = x^{-\gamma} \cdot \chi_0(x^\nu)$, and with Eq. (3.28) the following can be derived:

$$\begin{aligned} \chi &= L^{\gamma/\nu} \cdot \bar{\chi} \left(L^{1/\nu} |g - g_{\text{crit}}| \right) \\ &= L^{\gamma/\nu} \cdot \left(L^{1/\nu} |g - g_{\text{crit}}| \right)^{-\gamma} \cdot \chi_0 \left(\left(L^{1/\nu} |g - g_{\text{crit}}| \right)^{\nu} \right) \\ &= |g - g_{\text{crit}}|^{-\gamma} \cdot \chi_0 \left(L |g - g_{\text{crit}}|^{\nu} \right) \\ &= \xi^{\gamma/\nu} \cdot \chi_0 \left(\frac{L}{\xi} \right) \end{aligned} \tag{3.30}$$

Eq. (3.30) is the crucial equation to describe the scaling in finite systems near the critical point and to derive the critical exponents from QMC results at $T = 0$. Analogous expressions can be found for the magnetic order m and the structure factor S.

In addition to this scaling with length and coupling parameter, away from $T = 0$ we also must consider the scaling with temperature. At $T > 0$, Eq. 3.30 then generalizes to

$$\chi = L^{\gamma/\nu} \bar{\chi} \left(L^{1/\nu} |g - g_{\text{crit}}|, \; TL^z \right) \tag{3.31}$$

To extract information about the scaling from simulations at finite temperatures and lengths, it is then useful to scale the inverse temperature according to $\frac{1}{T} \propto L^z$ with the dynamical critical exponent z.

Concerning the exponents, the dependence of the scaling function on T and $\delta g = |g - g_{\text{crit}}|$ also applies in the same way to other measurable observables, while the exponent of the prefactor is unique. For example, the magnetization scales as

$$m_{\text{leg}} = L^{-\beta/\nu} \cdot \bar{m}_{\text{leg}} \left(L^{1/\nu} |g - g_{\text{crit}}|, TL^z \right).$$

The key goals of this chapter will be to determine the critical coupling strength to a better accuracy and to find the scaling exponents that describe the behavior of magnetic order and susceptibility at the quantum phase transition. We will also compare our findings to known field theoretical results for long-range lattice models,.

3.6.2. Known field-theoretical results

The following subsection is in part taken from our publication, Ref. [76].

We will first review the results from some recent RG studies that investigate the quantum critical properties of one-dimensional quantum system with long-ranged interaction and an $O(3)$

symmetry, namely Refs. [87, 90–92]. Ref. [90] looks at the $n = 1$ case that describes the quantum Ising model, while the others consider more generally an $O(n)$ interaction. Our case is $n = 3$, due to the three dimensional Heisenberg spins in our ladder models. In Appendix B of Ref. [90], relations of the critical exponents are derived, valid for a general ϕ^4 model with long-range interactions in the spatial direction.

We will see in what follows that these results—when inserting the appropriate values for the number of field-theory-components and for the decay of the spatial coupling—correspond well to the numerical findings for our model. The ϕ^4 theory is a continuum description of classical and quantum lattice models, which is valid near critical points where the correlation length is larger than the lattice spacing. It describes the second-order phase transition depending on an order field $\boldsymbol{\phi}$, whose expectation value changes from non-zero to zero at the phase transition, compare Ref. [93]. In magnetic chain and ladder models, this order field is commonly the magnetization $\boldsymbol{M} = \frac{1}{N}\sum_i \langle \boldsymbol{S}_i \rangle$, which is a scalar in the Ising model and a three component vector in the Heisenberg model. The crucial quantity in the considerations is then the Landau-Ginzburg energy functional. It describes the dependence of the free energy as a functional of the order parameter (field). It turns out that an expansion up to fourth order in ϕ is usually sufficient to describe the relevant quantities; this is called the ϕ^4 model. To solve this model, the authors of Ref. [90] utilize the Renormalization Group approach, a largely analytic technique integrating out short-range degrees of freedom by successive rescaling (compare e.g. Refs. [80, 94]).

Also for the long-range case of the quantum mechanical Heisenberg model, a ϕ^4 theory can be formulated and is widely equivalent to the analogous approximation of the quantum transverse field Ising model assessed in Ref. [90]. An ε expansion is then applied up to and including the two-loop diagrams, and momentum-shell RG is used for the evaluation of these diagrams.

For a quantum system in $1 + 1$ dimensions with a spatially long-ranged interaction that decays proportional to $1/r^{1+\sigma}$ with the spatial distance r, the long-ranged nature of the interactions is important in order to stabilize a non-trivial transition (compare e.g. Ref.[82]). We are especially interested here in the case $\sigma = 1$, $n = 3$. For $2/3 < \sigma < 2$, the critical exponents at the quantum phase transition differ from the mean-field values due to the effects of quantum fluctuations. With the above mentioned ϕ^4 theory, they have been approximately obtained[87, 90] as expansions in $\epsilon = 3\sigma/2 - d$, where d denotes the spatial dimension. In detail, within this expansion, Ref. [87] obtains from a one-loop calculation the result

$$\nu = \frac{1}{\sigma} + \frac{n+2}{n+8}\epsilon + \mathcal{O}\left(\epsilon^2\right) \tag{3.32}$$

for the critical exponent ν, which characterizes the divergence of the correlation length. Another recent work[90]reports $1/\nu = \sigma - \epsilon/3 + \mathcal{O}\left(\epsilon^2\right)$ for the special case of $n = 1$. This is in accord with the above result Eq. (3.32) for $\sigma = 1$, the case of interest here, but differs from it in the general case (cf. Ref. [90] for further discussion). From Eq. (3.32), we thus obtain an estimate of $\nu \approx 1.227$ for $\sigma = 1$ and $n = 3$. Ref. [90] furthermore reports a two-loop order result for the dynamical critical exponent z for $\sigma = 1$, $d < 2$ in the $O(n)$ case,

$$z = \frac{1}{2} + \frac{(n+2)\left(12 - \pi^2\right)}{16(n+8)^2}\tilde{\epsilon}^2 + \mathcal{O}\left(\tilde{\epsilon}^3\right), \tag{3.33}$$

where $\tilde{\epsilon} = 2 - d$, based on earlier RG calculations[95]. For the case of interest here, $d = 1$ and $n = 3$, this provides an estimate of $z \approx 0.505$. This value is also consistent with the RG results in Ref. [92]. It may be worthwhile to point out that within mean-field theory, a value of $z_{\mathrm{MF}} = \sigma/2 < 1$ results for $\sigma < 2$, already reflecting the fact that due to the long-ranged nature of the spatial interactions, correlations in the temporal direction are weaker than in the spatial direction (in contrast to a dynamical critical exponent of 1, obtained for many quantum critical spin models with only short-ranged interactions)[87]. For $\sigma = 1$, this gives a mean-field value of $z_{\mathrm{MF}} = 1/2$. With respect to the anomalous exponent η that characterizes the spatial decay of the order parameter correlation function $G(r)$ at the quantum critical point, different notations are used in the literature. Here, we follow the standard definition with

$$G(r) \propto 1/r^{d+z-2+\eta}$$

at criticality [82]. According to Refs. [87, 92], the value of η in the relevant region of σ for our study is fixed to $\eta = 2 - \sigma$, so that for $d = \sigma = 1$ we obtain

$$G(r) \propto 1/r^{z}. \tag{3.34}$$

Again, for $d = \sigma = 1$ this form agrees with the findings in Ref. [90] (in their convention, $G(r) \propto 1/r^{d-1+\eta}$ and they obtain the relation $\eta = z$ for $\sigma = 1$ and $n = 1$). Another useful result reported in Refs. [87, 90] for the case $\sigma = 1$ of interest here is the relation

$$\gamma/\nu = 1 \tag{3.35}$$

to the order parameter susceptibility exponent γ, which we can access in our model by the single leg susceptibility χ_{leg}. Combined with the value of $\eta = 2 - \sigma$, this relation follows from the general scaling relation

$$\gamma = \nu(2 - \eta).$$

In the following, we compare these RG results to our QMC estimates of the critical exponents, based on a finite-size scaling analysis of the numerical data.

3.6.3. Numerical results from finite size scaling

Scaling of the leg susceptibility The leg susceptibility matches the function Eq.(3.30): $\chi_{\mathrm{leg}} = L^{\gamma/\nu} \cdot \bar{\chi}\left(|g - g_{\mathrm{crit}}| \cdot L^{1/\nu}, TL^{z}\right)$, so that plots of $\chi_{\mathrm{leg}} L^{-\gamma/\nu}$ versus $(g - g_{\mathrm{crit}})\, L^{1/\nu}$ for different system lengths at inverse temperature $1/T = 2L^{z}$ collapse at the same, yet unknown, function $\bar{\chi}$. Moreover, plots of $\chi_{\mathrm{leg}} L^{-\gamma/\nu}(g)$ for different system sizes all cross at the critical coupling strength g_{crit}.

For the critical exponents that govern the decay of the susceptibility Eq. (3.30), the relation $\gamma/\nu = 1$ from Eq. (3.35) will be presumed as exact. Fig. 3.33 shows the plot of $\chi_{\mathrm{leg}} L^{-\gamma/\nu}(g)$, which should give a unique crossing point at g_{crit}. We can locate the critical coupling strength around $g \approx 1.9536 - 1.9537$.

To state this more precisely and to find the value for $\frac{1}{\nu}$, the collapse of the finite-size scaled susceptibility is used. We fit the scaled values including all results for different $L \geq 2000$ to a

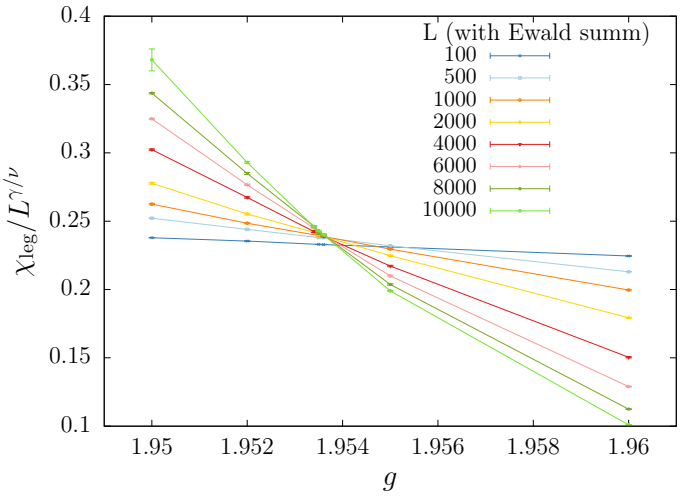

Figure 3.33.: Finite size scaling data for the leg susceptibility in the critical regions of the leg coupling. The inverse temperature is again adapted to system size $\beta = 2\sqrt{L}$. The values for $L = 100$ are subject to severe finite-size effects.

third order polynomial, and for this fit choose the parameters g_c and $\frac{1}{\nu}$ which give the minimal $\frac{\chi^2}{\mathrm{ndof}}$. The errors are determined using a bootstrap analysis. For the details see App. A.3. All together this yields:

$$\frac{1}{\nu} = 0.6841 \pm 0.0079 \tag{3.36}$$

$$\nu = 1.4618 \pm 0.0168 \tag{3.37}$$

$$g_{\mathrm{crit}} = 1.95364 \pm 1.2 \cdot 10^{-5} \tag{3.38}$$

The result for ν is not in good accordance with the findings from field-theory[87], namely:

$$\nu_{\mathrm{RG}} = \frac{1}{\sigma} + \frac{n+2}{n+8}\epsilon + \mathcal{O}\left(\epsilon^2\right) = \frac{27}{22} + \mathcal{O}\left(\epsilon^2\right) \approx 1.227 + \mathcal{O}\left(\epsilon^2\right) \qquad \epsilon = \frac{3\sigma}{2} - d \ ,$$

with the spacial dimension $d = 1$ and the long-range decay $\propto 1/r^{1+\sigma}$, so here also $\sigma = 1$. However, since this result is only in first order in the RG- parameter ϵ, it is probably numerically less precise than our estimate. Both agree at least insofar as the exponent is larger than the pure mean-field result[87] of $\nu_{\mathrm{MF}} = 1$.

Scaling of the structure factor The magnetic order along the leg can be deduced from the ferromagnetic structure factor, defined as:

$$S_{\mathrm{leg}} = \frac{1}{L}\sum_{ij}\left\langle S^z_{i\mu} S^z_{j\mu}\right\rangle \qquad m_{\mathrm{leg}} = \sqrt{\frac{\langle S_{\mathrm{leg}}\rangle}{L}} = \frac{1}{L}\sqrt{\sum_{ij}\left\langle s^z_{i\mu} s^z_{1\mu}\right\rangle} \qquad \text{with } \mu \in \{A, B\} \tag{3.39}$$

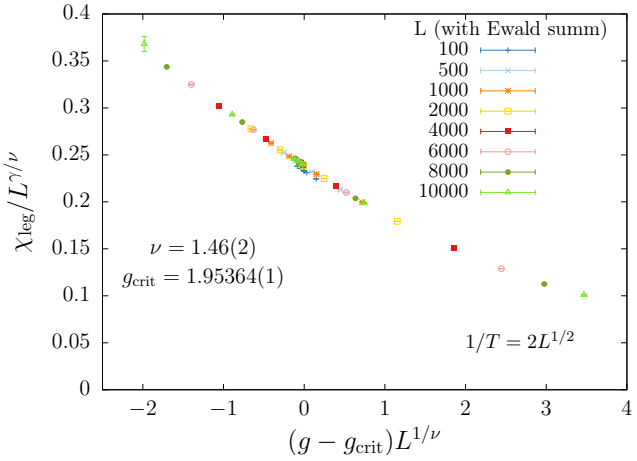

Figure 3.34.: The parameters found in Eqs. (3.36) and (3.38) give indeed a collapse of the plots for different lengths. They have been determined from the data for $L \geq 2000$.

The staggered structure factor includes both legs and is given by

$$S_{\text{Stagg}} = \frac{1}{L}\sum_i \left(\sum_j \left\langle s^z_{iA} s^z_{jA} \right\rangle - \sum_j \left\langle s^z_{iA} s^z_{jB} \right\rangle \right) = \frac{1}{L} \sum_{i,j,\mu'} \varepsilon_{\mu\mu'} \left\langle s^z_{i\mu} s^z_{j\mu'} \right\rangle \tag{3.40}$$

where we have defined the sign factor $\varepsilon_{\mu\mu'} = \begin{cases} 1 & \text{for } \mu = \mu' \\ -1 & \text{for } \mu \neq \mu' \end{cases}$.

It turns out that for any $J^{\text{AF}} > 0$ the two quantities are no longer independent, but for our temperature ranges simply

$$S_{\text{Stagg}} \approx 2 S_{\text{leg}}.$$

At first look this is not obvious, since one could instead assume that the staggered structure factor measured also the antiferromagnetic order in the system and should therefore bear additional information. However, we can easily rewrite the staggered structure factor as $S_{\text{stagg}} = \frac{1}{L}\left\{ \sum_{ij} \left\langle s^z_{iA} s^z_{jA} \right\rangle - \left(\sum_i \left\langle s^z_{iA} \right\rangle\right) \left(\sum_j \left\langle s^z_{jB} \right\rangle \right) \right\}$ to see that it does not actually measure the correlations between single pairs of spins on different legs. Furthermore, both legs are completely equivalent, and therefore will for any temperature and coupling strength on average always have the same difference in number between up and down spin, which will manifest itself after a sufficient number of Monte-Carlo runs: $\langle |\sum_i S^z_{iA}| \rangle = \langle |\sum_i S^z_{iB}| \rangle$. Due to the absence of an external field, the direction is however not specified by the ferromagnetic couplings, so only the absolute values are equal.

On the whole, as soon as $J^{\text{AF}} > 0$, these two configurations will arrange in opposite orientation. Of course, this structure is flawed by thermal fluctuations, but as we perform Monte Carlo runs at very low temperatures and want to gather information about the ground state features by

using finite size scaling, we find ourselves in the region where the opposite orientation massively dominates. There is an abrupt transition when turning on the antiferromagnetic coupling: At low temperatures for $J^{\mathrm{AF}} = 0 \Rightarrow g = 0$, one has two completely uncorrelated chains with $\langle|\sum_i S^z_{iA}|\rangle = \langle|\sum_i S^z_{iB}|\rangle$ and no preference in the mutual orientation; but for infinitely small antiferromagnetic rung coupling, opposite orientation is highly advantageous. We want to stress that this does not mean that all directly opposite rungs would be arranged in a singlet coupling, especially not for small rung couplings. But as the sum of products includes all possible pairs and can be put apart, the result for S_{stagg} will only reflect the mutual orientation of all spins on one rung with respect to the other.

More mathematically, the same effect is seen in the susceptibilities: Let the staggered susceptibility be defined as

$$\chi_{\mathrm{stagg}} = \frac{1}{2L}\sum_{ij}\int_0^{1/T} d\tau \left\langle \left(S^z_{iA} - S^z_{iB}\right)(\tau)\cdot\left(S^z_{iA} - S^z_{iB}\right)(0)\right\rangle = 2\chi_{\mathrm{leg}} - \chi_{\mathrm{uni}}.$$

In the regime of low temperatures regarded $\chi_{\mathrm{leg}} \gg \chi_{\mathrm{uni}}$, and the staggered susceptibility essentially measures the same quantities as χ_{leg}.

From the decay of the spin correlations $\left\langle S^z_{i\mu}S^z_{j\mu}\right\rangle \propto 1/r_{ij}^{z-1+\eta}$ at criticality, it follows that the leg structure factor scales as

$$S_{\mathrm{leg}}\left(g_{\mathrm{crit}}\right) \propto \int_0^L r_{ij}^{1-\eta-z} dr \propto L^{2-\eta-z}$$

The field-theoretical considerations have found $z \approx \frac{1}{2}$ (compare Eq. (3.33)) and $\eta = 1 - \sigma = 1$, so that the considered quantity at criticality should scale $S_{\mathrm{leg}} \sim L^{-1/2}$. In Fig. 3.35, the appropriately scaled staggered structure factor is plotted as a function of inverse ribbon length for different rung coupling strengths, a similar graphical representation as in Fig. 3.32. As the inverse length goes to zero, the qualitative behavior of this quantity changes depending on the coupling strength: While it increases with decreasing system length for couplings weaker than g_{crit}, it decreases for $g > g_{\mathrm{crit}}$ and finally tends to zero for large rung couplings in the thermodynamic limit. Right at the critical rung coupling, the graph is constant; so it is confirmed that

$$S_{\mathrm{stagg}}\left(g_{\mathrm{crit}}\right) = \tilde{c}\cdot L^{1-z} \quad \text{with } z \approx 0.5$$

and constant $\tilde{c} \in \mathbb{R}$. For the magnetic order along one leg follows directly $m_{\mathrm{leg}} \propto L^{-1/4}$ and the correlation function decays as $G\left(g_{\mathrm{crit}}\right) = \left\langle S^z_{i\mu}S^z_{j\mu}\right\rangle \propto r_{ij}^{-0.5}$.

Corresponding to Eq. (3.30) for the susceptibility, the magnetic order near the critical point should follow[96]

$$m_{\mathrm{leg}} = L^{-\beta/\nu}\cdot \bar{m}_{\mathrm{leg}}\left(\left(g - g_{\mathrm{crit}}\right)\cdot L^{1/\nu}, TL^z\right) \tag{3.41}$$

using some scaling function $\bar{m}$. So we can identify the critical exponent

$$\frac{\beta}{\nu} \approx \frac{1}{4} \tag{3.42}$$

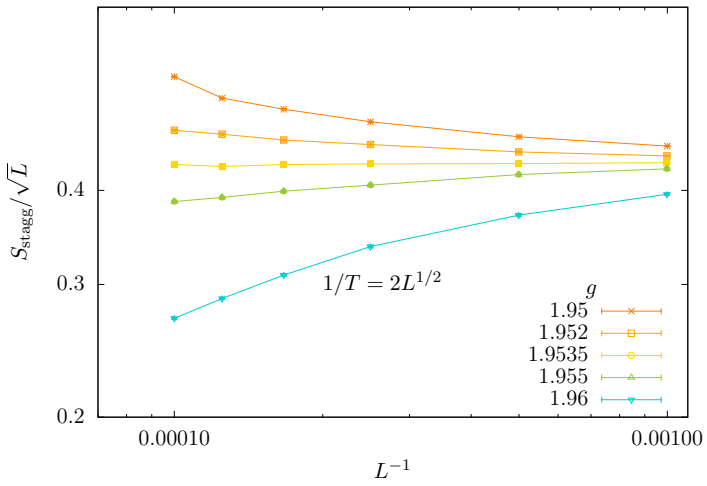

Figure 3.35.: The ferromagnetic structure factor S_{stagg} divided by $\sqrt{L}$ as a function of inverse system length for different rung couplings near the critical strength. Both axes have a logarithmic scale. The inverse temperature is $\beta = 2\sqrt{L}$, and error bars are smaller than symbol size.

To determine these values numerically more precisely, we regard the finite size scaling for the ferromagnetic structure factor, which accordingly scales as

$$S_{\text{leg}} = L^{-2\beta/\nu+1} \cdot \bar{S}\left((g - g_{\text{crit}}) \cdot L^{1/\nu}, TL^{z}\right) \ , \tag{3.43}$$

Concerning the exponent β/ν, we did not find a field theoretical result for comparison. Therefore, we take the result (3.36) as given and then determine the ideal values for g_{crit} and β/ν as the ones that minimize the χ^2/ndof of the corresponding multi- fit.

The same procedure as above (details see App.A.3) gives the following results:

$$g_{\text{crit}} \approx 1.95388 \pm 5.4 \cdot 10^{-4} \tag{3.44}$$

$$-2\frac{\beta}{\nu} + 1 \approx 1.48438 \pm 0.0108$$

$$\frac{\beta}{\nu} \approx 0.24219 \pm 0.0054 \tag{3.45}$$

These values have been inserted to produce a corresponding crossing and collapse plot, compare Fig. 3.36. The two results for the critical coupling strength Eq.(3.38) and Eq.(3.44) are not ideally equal, but they do conform within their error bars. One possible reason for deviations is that the collapse functions $\bar{\chi}$ and $\bar{S}$ are not ideally described by a polynomial of third degree. We believe the result (3.38) to be a bit more precise, because the histogram of the bootstap method for Eq.(3.44) slightly deviates from a normal distribution, compare App.A.3. This also reflects in the larger error for the value of g_{crit} when determined via the spin structure factor.

According to field theory (compare Sec. 3.6.2), the spatial decay of the correlation function is given by $G(r) \propto r^{-z}$, compare Eq. (3.34). From the connection between magnetic order

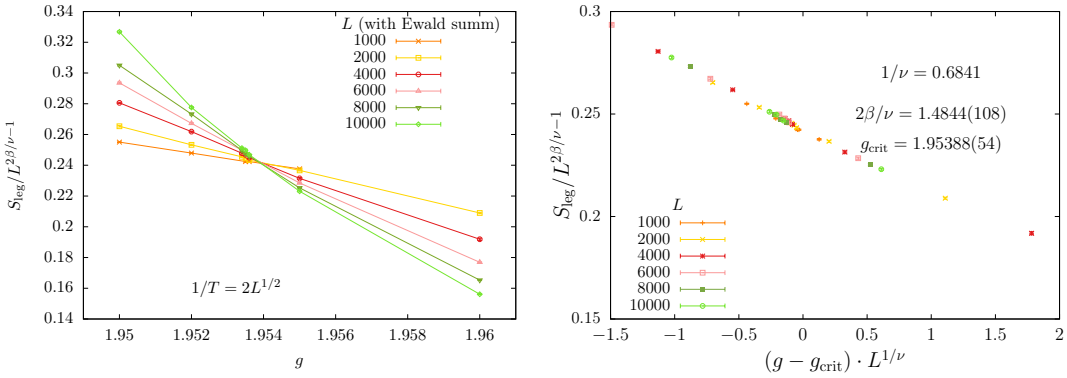

Figure 3.36.: Left: The ferromagnetic structure factor when scaled properly should cross for various system sizes at the critical coupling strength. Right: Another scaling yields a collapse plot, with the above results for g_{crit} and $\frac{\beta}{\nu}$ inserted appropriately.

and ferromagnetic structure factor follows directly a relation between the corresponding critical exponents:

$$m_{\mathrm{leg}} = \frac{1}{L}\sqrt{\sum_{i,j}\left\langle S_i^z S_j^z\right\rangle} \qquad \Rightarrow \frac{\beta}{\nu} = \frac{z}{2} \tag{3.46}$$

From the above mentioned field theoretical publication[90], we have a reference value for the exponent z given by Eq. (3.33), namely for our case

$$z_{\mathrm{RG}} = 0.5 + 0.0055\tilde{\varepsilon}^2 + \mathcal{O}\left(\tilde{\varepsilon}^3\right) \tag{3.47}$$

with the order parameter $\tilde{\varepsilon} = 1$ in our case. This prediction, which shuold be more precise than ν_{RG} because it was calculated to second order, fits well with our numerical result Eq. (3.45).

In contrast to the situation near criticality, when choosing $g = 4.0$, i.e. deep in the disordered phase, the spin correlation decays as the original couplings $\left\langle S_{i\mu}^z S_{j\mu}^z\right\rangle (g \gg g_{\mathrm{crit}}) \propto r_{ij}^{-2}$, which gives then for the spin structure factor

$$\frac{1}{L}\sum_{i,j}\left\langle S_{i\mu}^z S_{j\mu}^z\right\rangle \to \int_1^L \left(\frac{c}{x}\right)^2 dx = -\frac{c}{x}\Big|_1^L = c\left(-1 + \frac{1}{L}\right) = c\cdot(-1+L)$$

Inserting this with an approximation for large L gives $m = \frac{1}{L}\sqrt{\sum_{i,j}\left\langle S_i^z S_j^z\right\rangle} = \frac{1}{L}\sqrt{c\cdot(-1+L)} = \sqrt{c}\sqrt{\frac{1+L}{L^2}} \approx \frac{\sqrt{c}}{\sqrt{L}}$. The direct plot for $T = 0.01$ shown in Fig. 3.37 supports the picture of roughly quadratic decay.

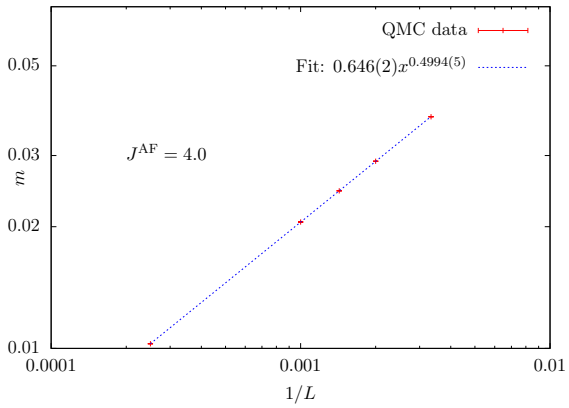

Figure 3.37.: The magnetization of the model H_2 deep in the disordered phase at low temperature $T = 0.01$ as a function of inverse system size.

Scaling of the spin correlations As outlines above (compare Sec. 3.6.2), the correlation function should follow $G(r) \propto r^{-(z+\eta-1)} = r^{-z}$. With our previous numerical result for $\frac{1}{\nu}$ given, it is now possible to determine z more precisely (compare Sec. 3.5). For this, the average correlation $c_{L/2} = \overline{\left\langle S_0^z S_{L/2}^z \right\rangle}$ can provide a collapse plot analogous to Eqs. (3.30) and (3.41). We plot $c_{L/2} \cdot L^{z+\eta-1}$ as a function of $(g - g_{\mathrm{crit}}) \cdot L^{1/\nu}$ for different values of g_{crit} and the exponent, choosing the parameters that give the best fit to a third order polynomial. The errors are determined from a bootstrap analysis with sample size $n = 1000$ and $N = 100$ runs. We get the results

$$g_{\mathrm{crit}} = 1.95363 \pm 1.5 \cdot 10^{-4} \tag{3.48}$$

$$z + \eta = 1.50595 \pm 0.0070 \tag{3.49}$$

For the plots using these exponents compare Fig. 3.38.

Comparison of the two numeric results Eq. (3.49) and Eq. (3.45) shows that the above relation Eq.(3.46) is met within error bars.

3.6.4. Behavior near criticality

Size of the spin gap When the system is in the disordered phase, the uniform susceptibility decreases exponentially, like it does in the Heisenberg ladder. Following Ref. [73] (p.169), the uniform susceptibility of the Heisenberg ladder for low temperatures to leading order behaves as

$$\chi_{\mathrm{uni}}(T) \propto e^{-\Delta/T} \tag{3.50}$$

We therefore extrapolate the spin gap by performing a linear regression of the low temperature behavior (i.e. $T \leq 0.2$) of $-T \cdot \ln(\chi_{\mathrm{uni}})$ as a function of T for coupling strengths g close to, but larger than the critical coupling strength. The spin gap is then found as the axis intercept of this

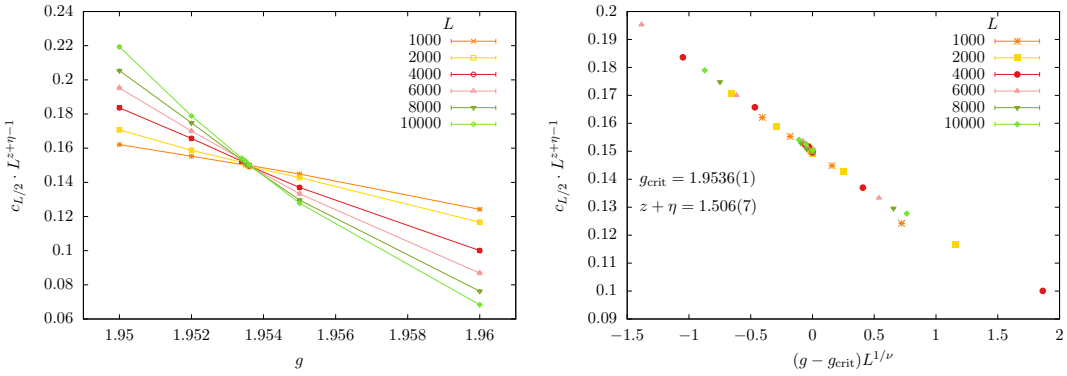

Figure 3.38.: The average spin correlation over half the ribbons length $c_m = \overline{\langle S_0 S_{L/2} \rangle}$ yields a crossing point plot and a collapse point analogous to the quantities in Sec. 3.6.3 and Sec. 3.6.3. The other critical scaling exponent is $1/\nu = 0.6841$.

linear behavior. The opening of a gap in a disordered phase after a quantum phase transition is supposed to follow[82],chapter 1.1

$$\Delta \propto |g - g_{\mathrm{crit}}|^{\nu z} \tag{3.51}$$

with the exponents ν and z as defined in Sec. 3.6.3 and Sec. 3.6.4, respectively. Conventional error propagation gives

$$\nu z = 0.7575 \pm 0.0138 \tag{3.52}$$

Presented in Fig. 3.39 in the small plot are the linear extrapolations for different g, and in the large panel are the results for $\Delta(g)$ together with a fit to Eq. (3.51), where the exponent νz is fixed and only the prefactor left for adaption.

For larger g and very small T some date points are missing, because their QMC results are $\chi_{\mathrm{uni}} = 0.0$, so a meaningful logarithm cannot be calculated.

The results in the main panel represent the requested behavior reasonably well, nearly all within error bars. We believe that the deviation of $\Delta(g = 1.957)$ stems from the fact that finite-size effects are more relevant near the quantum critical point.

Binder ratio The Binder ratio is a dimensionless quantity defined as

$$B_2 = \frac{\left\langle m_{\mathrm{leg}}^4 \right\rangle}{\left\langle m_{\mathrm{leg}}^2 \right\rangle^2} \tag{3.53}$$

and at the critical point it is independent of the system size[73] up to higher order corrections. This follows directly from the scaling relation (3.41) due to the overall equal exponents. Therefore, similar to the cases before, a plot of the Binder ratio for different system sizes will cross at the critical coupling strength. At the critical point $|g - g_{\mathrm{crit}}| = 0$, Eq.(3.31) simplifies even more, and the scaling for finite temperatures[97] is then simply

$$B_2 = \widetilde{B}_2 (TL^z) \ ,$$

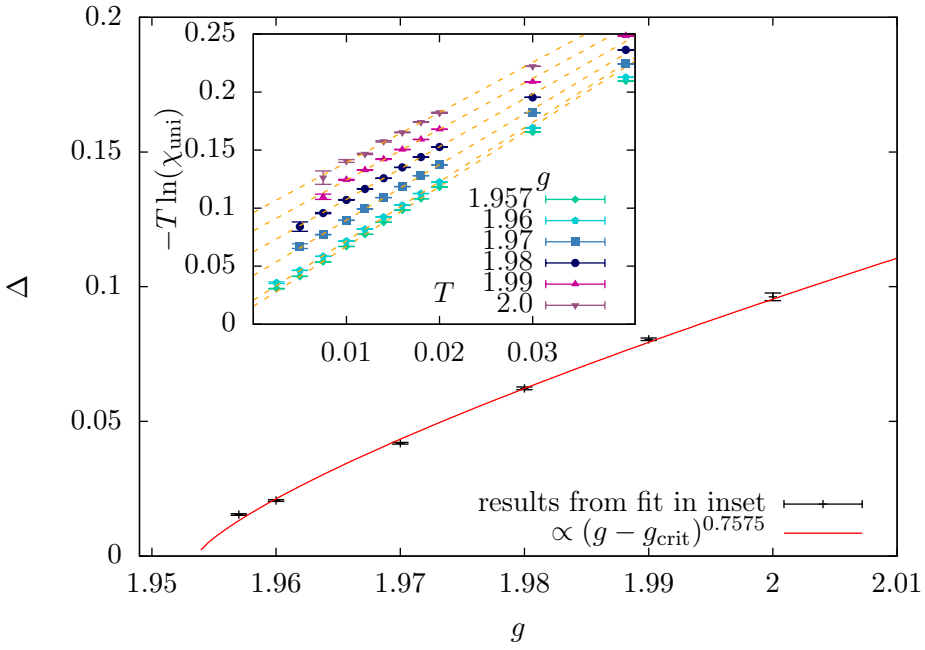

Figure 3.39.: Large plot: The gap as a function of g for Hamiltonian H_2 for $L = 8000$ along with a fit to Eq. (3.51), with νz fixed, using $g_{\text{crit}} = 1.9536$. The values for $\Delta(g)$ have been obtained by linear fits following Eq. (3.50) for $T \leq 0.2$ at different values of g, compare small inset.

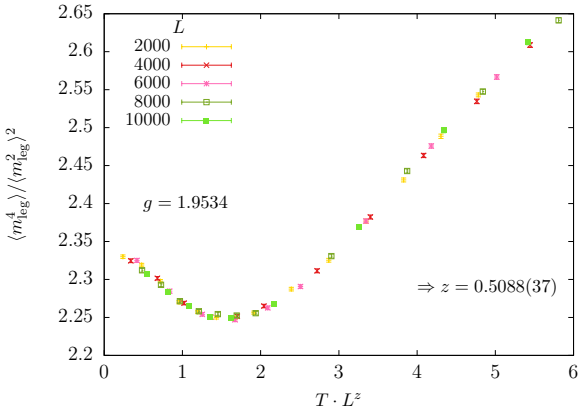

Figure 3.40.: The collapse of the Binder ratio function for various L at the trial value $g_{\mathrm{crit}} = 1.9536$ (received in (3.38)).

So again there will be a collapse of the results for different lengths, provided the parameters are chosen correctly. Such an analysis is independent from the above results for z, and it fits our technique well, because it represents a finite temperature analysis.

Fig. 3.40 displays the result for $g = 1.9536$ from Sec. 3.6.3. The corresponding result for z has been obtained by fitting the low-temperature part of the data set (up to $TL^z \approx 3$) to a third-order polynomial and choosing the parameter that gives a minimal χ^2/ndof. The error can be determined by conventional error propagation here. The fit has the goodness-of-fit parameter $\chi^2/\mathrm{ndof} \approx 1.78$ and agrees with the theoretical result Eq. (3.47) within error bars.

Susceptibility and structure factor Finally, it is also insightful to regard the susceptibility $\chi_{\mathrm{leg}}\left(L, g = g_{\mathrm{crit}}\right)$ and the order parameter $S_{\mathrm{leg}}\left(L, g = g_{\mathrm{crit}}\right)$ as functions of the system length at the critical point, and with the temperature scaled appropriately with system length. Comparison with Eq. (3.31) shows that in this scenario the scaling function $\bar{\chi}\left(|g - g_{\mathrm{crit}}| \cdot L^{1/\nu},\ TL^z\right)$ is constant and the only scaling behavior that is left should be

$$\chi_{\mathrm{leg}}\left(L, g = g_{\mathrm{crit}}, T = 0.5L^{-z}\right) \propto L^{\gamma/\nu}. \tag{3.54}$$

Analogously, we expect $S_{\mathrm{leg}}\left(L, g = g_{\mathrm{crit}}, T = 0.5L^{-z}\right) \propto L^{-2\beta/\nu+1}$ at the critical coupling strength. Fig.3.41 (top) shows the fit for $g = 1.9536$. The actual result for $\frac{\beta}{\nu}$ is in a good accordance with the expectations. The result for $\frac{\gamma}{\nu}$ still fits, but shows a slight deviation beyond the error bars. A reason for this could be that the critical coupling strength is not met exactly.

3.6.5. Meaning for real GNRs

The unweighted mean of all three results Eqs. (3.38), (3.44) and (3.48) with conventional error propagation gives the combined result:

$$g_{\mathrm{crit}}^{combi} = 1.95372 \pm 1.9 \cdot 10^{-4}$$

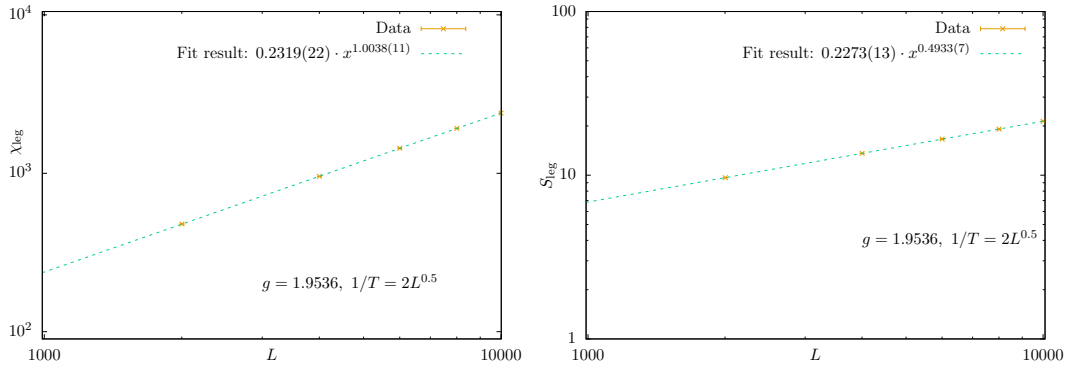

Figure 3.41.: At $g \sim g_{\text{crit}}$ and $1/T = 2\sqrt{L}$, the leg susceptibility is fitted to the power law behavior predicted in Eq. (3.30) (left side) and the ferromagnetic structure factor to Eq. (3.43) (right side), for the critical coupling strength $g = 1.9536$.

In a realistic GNR with a Hubbard model Hamiltonian, such a high ratio of anti-ferromagnetic to ferromagnetic interaction according to our result can only be reached for very narrow ribbons with $W \leq 6$ unit cells, compare Sec.3.4.3. For wide ribbons, a higher anti-ferromagnetic coupling can only be achieved, and the rung singlet phase can only be reached for a small Hubbard interaction compared to the nearest-neighbor hopping: $\frac{U}{t} < 1$. When using the above model at the mostly investigated ribbons width $W = 10$ unit cells and the critical g_{crit}^{combi}, then the phase transition for occurs at

$$U_{\text{crit}}\,(W = 10) \approx \sqrt{\frac{g_{\text{crit}}}{0.43}}^{-1} t = 0.46914t \pm 1.9 \cdot 10^{-4} t$$

Therefore, we conclude that for wide graphene nanoribbons, the ground state in the thermodynamic limit is the ferromagnetic ordered state without a spin gap. The two legs of the effective ladder model can be roughly understood as two antiferromagnetically connected edge-superspins. Naturally, this ferromagnetic order is destroyed at any finite temperature following the Mermin-Wagner theorem[20]. The state does not have a spin gap, and it has been found previously[98] that the low-lying excitations should be single-particle excitations with linear dispersion relation. In contrast to this, it was shown before[31, 99] that chiral graphene nanoribbons with one electron per zigzag segment have exponentially decaying spin couplings along the leg and hence a disordered ground state.

Also, for extremely narrow zigzag GNRs (i.e. $W = 2$) it was shown by explicit QMC calculations[12] on the lattice that the ground state does not have a ferromagnetic order and is dominated by rung singlets across the ribbons extend. There is indication within our model, too, that for narrow ribbons $W \leq 6$ the effective ladder model results in a disordered ground state with exponentially decaying spin correlations and no spin gap. So all in all it seems plausible that there is a phase transition in zigzag graphene nanoribbons depending on the ribbons width that also tunes the strength of the antiferromagnetic rung couplings: While very narrow nanoribbons have a disordered ground state, medium and wide GNRs exhibit long-range ferromagnetically ordered legs at $T = 0$.

3.7. Perturbation theory for weak leg coupling

Finally, we shall look at the model H_2 in the opposite limit of a very large rung coupling $g \to \infty$. To get an estimate for the correct behavior in the disordered phase, first order perturbation theory in the leg couplings is performed, where the unperturbed ground state shall be the state with spin singlets on every rung.

Hence the Hamiltonian is written as

$$H = H_0 - J_\mathrm{F} H_\mathrm{pert} = J_\mathrm{AF} \sum_{i=1}^{N} \boldsymbol{S}_{iA} \cdot \boldsymbol{S}_{iB} - J_\mathrm{F} \sum_{i,j=1}^{N} \frac{1}{r_{ij}^2} \left(\boldsymbol{S}_{iA} \cdot \boldsymbol{S}_{jA} + \boldsymbol{S}_{iB} \cdot \boldsymbol{S}_{jB} \right) \tag{3.55}$$

with the free ground state $|\psi_0\rangle = \sum_i \frac{1}{\sqrt{2}} \left(|\uparrow\rangle_{iA} \otimes |\downarrow\rangle_{iB} - |\downarrow\rangle_{iA} \otimes |\uparrow\rangle_{iB} \right)$.

The perturbed state is then given by

$$|\psi_1 (J_F)\rangle = J_F \sum_n \frac{\langle \psi_n \mid H_\mathrm{pert} \mid \psi_0 \rangle}{E_n^0 - E^0} |\psi_n\rangle$$

Applying the ferromagnetic spin operators to one rung in singlet state gives::

$$\begin{aligned}
&\boldsymbol{S}_{1A} \cdot \boldsymbol{S}_{2A} \frac{1}{\sqrt{2}} \left(|\uparrow\downarrow\rangle_1 - |\downarrow\uparrow\rangle_1 \right) \otimes \frac{1}{\sqrt{2}} \left(|\uparrow\downarrow\rangle_2 - |\downarrow\uparrow\rangle_2 \right) \\
=& \left(\frac{1}{2 \cdot \sqrt{2}} \right)^2 \left\{ \left((1-i) |t_-\rangle_1 + (-1-i) |t_+\rangle_1 + \sqrt{2} |t_0\rangle_1 \right) \otimes \left((1-i) |t_-\rangle_2 + (-1-i) |t_+\rangle_2 + \sqrt{2} |t_0\rangle_2 \right) \right\} \\
=& \frac{1}{8} \Big\{ -2i |t_- t_-\rangle - 2 \left(|t_- t_+\rangle + |t_+ t_-\rangle \right) + \sqrt{2} \cdot (1-i) \left(|t_- t_0\rangle + |t_0 t_-\rangle \right) + 2i |t_+ t_+\rangle + \sqrt{2} \cdot (-1-i) \left(|t_+ t_0\rangle + |t_0 t_+\rangle \right) + 2 |t_0 t_0\rangle \\
=& -\frac{i}{4} |t_- t_-\rangle - \frac{1}{4} \left(|t_- t_+\rangle + |t_+ t_-\rangle \right) + \frac{(1-i)}{4 \cdot \sqrt{2}} \left(|t_- t_0\rangle + |t_0 t_-\rangle \right) + \frac{i}{4} |t_+ t_+\rangle + \frac{(-1-i)}{4 \cdot \sqrt{2}} \left(|t_+ t_0\rangle + |t_0 t_+\rangle \right) + \frac{1}{4} |t_0 t_0\rangle
\end{aligned}$$

with the three triplet states $|t_+\rangle = |\uparrow\uparrow\rangle$, $|t_-\rangle = |\downarrow\downarrow\rangle$, and $|t_0\rangle = \frac{1}{\sqrt{2}} \left(|\uparrow\downarrow\rangle + |\downarrow\uparrow\rangle \right)$. At the opposite leg, we get the exact same result.

For a model system of only four electron sites, with the ground state consisting of two singlets, the energy difference between a state with any two of the triplet states and the singlet state is $2 \cdot \left(E_n^0 - E^0 \right) = 2 J_\mathrm{AF}$. The new state is not normalized, but instead $\langle \psi_t(1,2) \mid \psi_t (1,2) \rangle = \frac{9}{16}$. With this we get:

$$\begin{aligned}
&\sum_n \frac{\langle \psi_n \mid \boldsymbol{S}_{1A} \boldsymbol{S}_{2A} + \boldsymbol{S}_{1B} \boldsymbol{S}_{2B} \mid \psi_0 \rangle}{E_n^0 - E^0} |\psi_n\rangle \\
=& \frac{2}{2 J_\mathrm{AF} \, \frac{9}{16}} \left\{ \frac{i}{4} \cdot \left(- |t_- t_-\rangle + |t_+ t_+\rangle \right) - \frac{1}{4} \left(|t_- t_+\rangle + |t_+ t_-\rangle \right) \right. \\
&\left. + \frac{(1-i)}{4 \cdot \sqrt{2}} \left(|t_- t_0\rangle + |t_0 t_-\rangle \right) + \frac{(-1-i)}{4 \cdot \sqrt{2}} \left(|t_+ t_0\rangle + |t_0 t_+\rangle \right) + \frac{1}{4} |t_0 t_0\rangle \right\} \\
=& \frac{16}{9 \cdot J_\mathrm{AF}} |\psi_t (1,2)\rangle
\end{aligned}$$

where the state with the above calculated sum of triplet states at the positions x_1 and x_2, and singlets at each other position, has been given the name $|\psi_t(1,2)\rangle$. Looking now at a ladder of length N with the Hamiltonian (3.55), the result for the ground state in first order perturbation theory is:

$$|\psi_1(J_F)\rangle = |\psi_s\rangle + \sum_{i,j} \frac{16}{9J^{\mathrm{AF}}} \cdot \frac{J^{\mathrm{F}}}{r_{ij}^2} |\psi_t(i,j)\rangle$$

In the next step, the spin spin correlation shall be calculated using this approximation. For each bond, the spin z operator on the first leg turns a triplet with $m = 0$ into a singlet: $S_A^z |s\rangle = S_A^z \frac{1}{\sqrt{2}} (|\uparrow\downarrow\rangle - |\downarrow\uparrow\rangle) = \frac{1}{2} \cdot \frac{1}{\sqrt{2}} (|\uparrow\downarrow\rangle + |\downarrow\uparrow\rangle) = \frac{1}{2} |t_0\rangle$ and the other way round: $S_A^z |t_0\rangle = \frac{1}{2} |s\rangle$. The triplet states with $m_S = \pm 1$ only get a prefactor $S_A^z |t_\pm\rangle = \pm\frac{1}{2} |t_\pm\rangle$. On the second leg, the results are the same up to a minus sign: $S_B^z |s\rangle = S_B^z \frac{1}{\sqrt{2}} (|\uparrow\downarrow\rangle - |\downarrow\uparrow\rangle) = \frac{1}{2} \cdot \frac{1}{\sqrt{2}} (-|\uparrow\downarrow\rangle - |\downarrow\uparrow\rangle) = -\frac{1}{2} |t_0\rangle$ and $S_B^z |t_0\rangle = -\frac{1}{2} |s\rangle$. Since the triplet and singlet states are always transformed into one another pairwise, these signs cancel out. The expectation value for the spin spin correlation is then given by:

$$\begin{aligned}
&\langle \psi_1(J_F) | S_{nA}^z S_{mA}^z | \psi_1(J_F) \rangle \\
&= \langle \psi_1(J_F) | S_{nB}^z S_{mB}^z | \psi_1(J_F) \rangle \\
&= \langle \psi_s | S_{nA}^z S_{mA}^z | \psi_s \rangle + \\
&\quad \sum_{i,j} \frac{16}{9} \frac{J_{\mathrm{F}}}{J_{\mathrm{AF}}} \frac{1}{|\vec{r}_i - \vec{r}_j|^2} \left(\langle \psi_s | S_{nA}^z S_{mA}^z | \psi_t(i,j) \rangle + \langle \psi_t(i,j) | S_{nA}^z S_{mA}^z | \psi_s \rangle + \langle \psi_t(i,j) | S_{nA}^z S_{mA}^z | \psi_t(i,j) \rangle \right)
\end{aligned} \tag{3.56}$$

$$\begin{aligned}
&= 0 + \sum_{i,j} \frac{16}{9} \frac{J_{\mathrm{F}}}{J_{\mathrm{AF}}} \frac{1}{|\vec{r}_i - \vec{r}_j|^2} \left(\frac{1}{16} + \frac{1}{16} + \frac{i}{4} \left(-\frac{1}{4} + \frac{1}{4} \right) - \frac{1}{4} \left(-\frac{1}{4} - \frac{1}{4} \right) \right) \delta_{ni} \delta_{mj} \\
&= \frac{J_{\mathrm{F}}}{J_{\mathrm{AF}}} \frac{1}{|\vec{r}_n - \vec{r}_m|^2} \cdot \frac{4}{9}
\end{aligned} \tag{3.57}$$

In the mixed expectation values, the only elements that do not vanish are hence

$S_i^z S_j^z |s, ..., t_0(i), ..., t_0(j), s, ...\rangle = \frac{1}{4} |s, s, s, s, ...\rangle$. In the last expectation value the contributions come from $|t_\pm\rangle$ terms. This result only constitutes a good approximation in the disordered phase, with $J_{\mathrm{AF}} \gg J_{\mathrm{F}}$ (so $g \gg 1$). It is consistent with our assumption that for large antiferromagnetic coupling of the spin correlations should decay as $\propto \frac{1}{r^2}$ like the coupling itself (compare Sec.3.5). For $g = 4.0$ the spin spin correlation is fitted to

$$\langle S_0^z S_x^z \rangle = a \cdot \left(x^b + (L - x)^b \right)$$

and the results are plotted in Fig.3.42. The fit coefficients meet expectations with an acceptable accuracy.

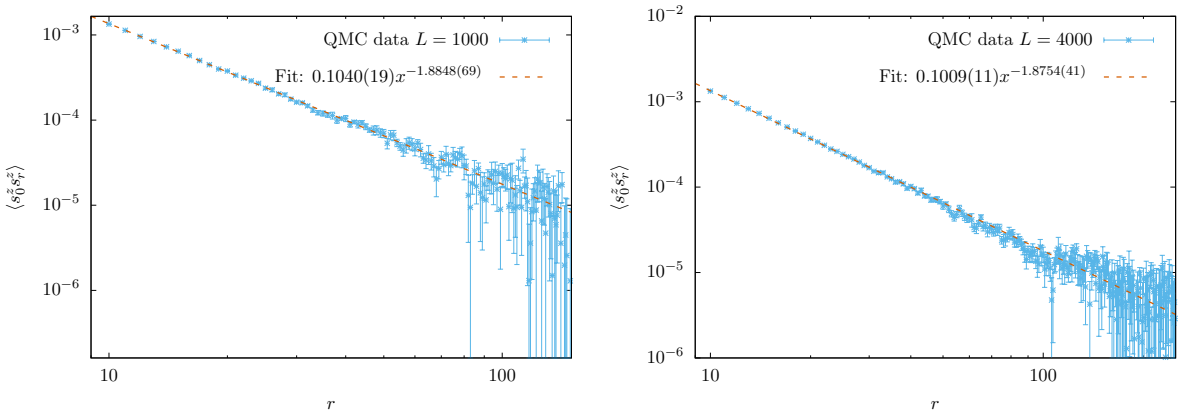

Figure 3.42.: The spin spin correlation in the disordered phase, for $g = 4.0 \gg 1.0$ at $T = 0.01$. Ribbon lengths are $L = 1002$ (left) and $L = 4002$ (right) with Ewald summation, where the first and last 10 sites have not been included in the fit, because they show short-range interaction behavior. The reduces chi squares are $\chi^2/\text{ndof} \approx 0.98$ (left) and $\chi^2/\text{ndof} \approx 1.50$. Numerically, we fit to the function $f(r) = a\left(r^b + (L-r)^b\right)$. The perturbative result Eq. (3.57) gives the factor $a = 1/9 = 0.\bar{1}$ and the exponent $b = -2.0$.

4. Conclusion

Summary

In this work, it was demonstrated that the magnetic interactions of the edge states in zigzag graphene nanoribbons are well approximated by an effective model, which leads to more general, scalable Heisenberg spin ladder models that exhibit a quantum phase transition as a function of interaction strength. We have started from the Hubbard model on the honeycomb lattice and applied a particular effective model, which had previously been used for specially tailored chiral nanoribbons, to plain zigzag ribbons. The first basic step of the underlying rewriting is to use the eigenbasis of the non-interacting Hamiltonian, thereby separating edge and bulk states, and then to treat the bulk states as a perturbation to the edge-state interaction. The implicitly used small parameter is the overlap between localized edge states and delocalized bulk states. In the second step, one introduces a Wannier basis for the edge states, so that each state is essentially singly occupied, and one can therefore go over to a Heisenberg spin model for the edge state interaction. We have demonstrated that for not-too-narrow plain zigzag nanoribbons (i.e. with width $W \gtrsim 8$ unit cells), this model yields good approximations. In accordance with earlier investigations using different methods, a ferromagnetic coupling between edge states on the same ribbon side and an antiferromagnetic interaction between opposite ribbon sites were found. Furthermore, our results displayed a long-range coupling along the ribbon sides that decays as $\sim 1/r^2$, which is different from the findings for chiral nanoribbons. The antiferromagnetic coupling decays as $\sim 1/r^4$ and thereby acts essentially as short-ranged. When varying the ribbon width, the ferromagnetic couplings are only weakly affected, while the direct opposite antiferromagnetic interactions are reduced as $\propto 1/W^3$. It was verified in a thorough analysis that second order correction terms do not alter the result beyond uncertainties of $\sim 5\%$, so they only need to be taken into account if a very high accuracy is required. Nevertheless, the investigation of these second-order terms gives some insight in the involved interaction processes. We have found a density-density interedge coupling that constitutes an analogy to the well-known RKKY interaction, which describes the coupling between magnetic impurities via intermediate conduction electrons. Moreover, we have demonstrated that the special behavior of some of the second-order interactions justifies choosing the portion of the Brillouin zone in which the edge states are found to be $k_{\mathrm{edge}} \in \left[-\frac{\pi}{3}, \frac{\pi}{3}\right]$. We have also briefly regarded the influence of second-nearest neighbor hoppings and found that when included in the perturbation terms, they do not have any significant influence on the coupling terms. Moreover, we have shown that the model can also be applied to a two-dimensional layer of black phosphorus, one example of a variety of further recently synthesized two-dimensional materials. This gives a slightly increased ferromagnetic leg coupling, but drastically reduced antiferromagnetic interactions, when compared to graphene. We did not find a long-range ferromagnetic order at non-vanishing temperatures in phosphorene.

The aim of the second part of this thesis was to generalize the above findings to scalable spin-ladder models and to investigate their properties for long ribbons and small, but finite temperatures by means of quantum Monte Carlo simulations. For this, we have set up two different models: The first model is quite close to the actual results for a narrow GNR, using the four/five concrete nearest-neighbor interaction strengths and a $1/r^2$ and $1/r^4$ decay for the long-distance couplings, respectively. The second model consists essentially of two Haldane-Shastry chains—with ferromagnetic couplings overall decaying as $1/r^2$—coupled by nearest-neighbor antiferromagnetic leg interaction. We introduce the scaling parameters λ and g that tune the ratio of antiferromagnetic to ferromagnetic coupling strength. Then for both models a quantum phase transition is found, which is driven by said scaling parameters:

- For strong leg coupling strengths (and small g or λ, respectively), the system is in a weak leg-ferromagnetic state. At $T = 0$ in the thermodynamic limit, long-range ferromagnetic order exists, and the system can be roughly understood as two antiferromagnetically coupled superspins. Any infinitesimally small temperature naturally destroys this long-range order following the Mermin-Wagner theorem: The magnetization m then vanishes in the thermodynamic limit, and part of the spin-spin correlations decay exponentially with ribbon distance. Even at long distances in the thermodynamic limit, however, the correlation function does not decay faster than $1/r^2$, which is due to the underlying order of the coupling. Furthermore, the full system is gapless allowing for excitations at arbitrarily small energies, and the susceptibility of a single leg diverges as it does for the Haldane-Shastry chain.
- For strong rung coupling strengths (and large scaling parameters), the system is in a disordered, rung singlet state. Deep in this phase, the long-range spin-spin interactions decay nearly as $1/r^2$ with no other correlations beyond the ones induced by the couplings themselves. The full system has a spin excitation gap, corresponding to the energy needed to break up one singlet bond, while the susceptibility of one single leg converges to a constant value with increasing system length.

According to Lieb's theorem, for the Hubbard model on a finite bipartite lattice with equal number of sites per sublattice, the ground state must be an overall spin singlet $\boldsymbol{S}_{\mathrm{ges}} = 0$; both ground state phases are consistent with this. The disordered spin singlet-phase is basically analogous to the well-known Heisenberg ladder with only nearest-neighbor interactions. However, in that system any small antiferromagnetic rung coupling destroys the ferromagnetic order at $T = 0$ and drives the system into the disordered phase. Here, in contrast, the long-range couplings along the legs seem to stabilize the ordered phase, so that only at a definite rung coupling strength the phase transition occurs.

For the generalized model of two coupled Haldane-Shastry chains, this critical coupling strength is $g_{\mathrm{crit}} = J^{\mathrm{AF}}_{\mathrm{crit}}/J^{\mathrm{F}}\,(r=1) \approx 1.95$. We have furthermore investigated the critical exponents of the quantum phase transition. For the dynamical critical exponent z, which governs the interplay between length and temperature dependence of several observables when approaching the thermodynamic limit, we found a value that is in good accordance with known second-order field-theoretical results for ϕ^4-theories with long-range interaction[87, 90]. For the critical exponent ν, describing the divergence of the correlation length, we find a rather significant

deviation from field-theoretical works, which however only offer a result up to first order. We are convinced that our findings are more precise in this respect. Additionally, an estimate for the exponent η, which governs the spatial decay of the correlation function $G(r)$, was determined. The size of the spin gap in the disordered phase is in accordance with a power-law dependence $\Delta \propto |g - g_{\mathrm{crit}}|^{\nu z}$.

Finally, we have made a brief analytic calculation for the situation deep in the disordered phase: Treating the all-singlet state as the ground state and the ferromagnetic couplings by standard perturbation theory gives an algebraic decay of the spin-spin correlations $\propto 1/r^2$, with a prefactor that conforms sufficiently precisely with the numerical findings for $g = 4$.

Concerning the ladder that is closer to the original zigzag ribbons with $W = 10$, the critical rescaling-factor is found to be $\lambda_{\mathrm{crit}} \approx 3.45$. In part, this much higher value can be understood by the fact that in a realistic GNR the ferromagnetic short-range couplings are stronger than the following power-law decay, while the short-range antiferromagnetic couplings are reduced with respect to the long-range tail. As another interesting point, we find indication for a quantum phase transition depending on the ribbon width W. For $W = 6$ at the original couplings (i.e. $\lambda = 1$), we observe a ground state clearly deep in the disordered phase, whereas for $W \geq 8$ the unaltered couplings in the thermodynamic limit are in the ferromagnetic state. While the effective model is not fully precise for ribbon widths $W \leq 6$ —due to the relatively large value of the perturbative $t^*/U\Gamma^{xxxx}$—, this is still a strong hint for such a phase transition. That would be in accordance with quantum Monte Carlo calculations directly on the lattice for extremely narrow ribbons $W = 2$, which find an exponentially decaying correlation in this case, compare Refs. [12, 100].

Outlook

It would be worthwhile to further investigate the possible phase transition depending on width, ideally with a technique that can cover both wide and narrow graphene nanoribbons at equal accuracy. If such a phase transition is indeed confirmed, this would constitute an interesting crossover between a half-metallic state, which could also be useful for applications in the field of spintronics, on the one hand and a pure quantum state on the other hand[100].

In recent years, other two-dimensional materials are more and more getting in the focus of research, too. We have seen that our effective model is easily applicable to phosphorene including only nearest-neighbor hopping. The investigation of this and other two-dimensional materials could be made more precise by including also further away coupling terms, especially in materials that are not fully planar. Concerning graphene, too, one could amplify in further studies the topic of next-nearest neighbor hopping terms when included in the unperturbed Hamiltonian. It might be of interest to develop a scalable ladder model also for these interactions. In addition, one could further increase how realistic the models are by introducing Coulomb repulsion beyond the onsite value, compare Ref. [98].

It is certainly of interest to also look at the spin dynamics of the systems investigated here. The low-energy excited states can be regarded by means of quantum Monte Carlo techniques. One

might gain further insight by analyzing the real-time out-of-equilibrium behavior and the quench dynamics[100] in both the weakly-ordered and the quantum disordered phase. For not-too-long spin chains, this could be done by means of time-dependent DMRG methods[101], or for very small systems also with exact diagonalization.

Acknowledgements

For support with regard to the content First of all, I would like to thank my supervisor Stefan Wessel for all his support, for many ideas and enlightening discussions. Also during your informative lectures on computational and statistical physics, you have taught me much about modern physics.

Also many thanks to Manuel Schmidt, who did most of the supervision during my first year and who came up with the idea for the effective model for edge magnetism. You have sparked my interest in graphene.

Thank you to Dante Kennes, who took much time to explain to me the details of infinite DMRG. The results of this project could unfortunately not become part of this work due to other reasons.

Thanks to Michael Golor for his tips and explanations on the quantum Monte Carlo method. Thanks to Michael Golor, Farideh Hajiheidari and Riccardo Mazzarello for fruitful discussions about graphene and edge magnetism.

Thanks to Niklas Gergs for critical reading of the introduction and conclusion of this thesis.

For funding

This work was supported by the DFG via Research Training Group 1995 "Quantum many-body methods in condensed matter systems".

The IT Center Aachen and JSC Jülich provided access to computing time through JARA-HPC.

For organizational support and for their friendliness I want to thank all colleagues from the Institute for Theoretical Solid State Physics for the great work atmosphere. I will for sure miss working here. Special thanks to Farideh; it was always nice to have you as a room mate and to travel to conferences together.

Thanks to the secretaries Gabi, Julia and Gillian for your assistance with the "red tape", especially concerning the maternity leave.

I am grateful to my parents for all their emotional support as well as for much logistic help. It was a good feeling I could always resort to you.

Thanks to my friends Farideh, Mona, Donatus, Basti and Christoph for your good company. Although we have been diverging spatially, I really do hope we will keep close contact.

Niklas, thank you for tips concerning LaTeX and bibliography management, and for fixing my Gentoo Linux several times. But much more I am grateful to you for all the motivation and inspiration you gave me and for always being there during happy and difficult times. You are my true love.

A. Appendix

A.1. Rewriting the next-nearest neighbor hopping

We want to rewrite Eq. (2.36) in the sublattice polarized edge basis:

$$
\begin{aligned}
&- t' \sum_n \sum_k 2 \sin\left(\frac{k}{2}\right) \Big\{ \frac{1}{2} \xi_{k++}(n,A) \left(e^\dagger_{kA} + e^\dagger_{kB}\right)(e_{kA} + e_{kB}) \\
&+ \frac{1}{2} \xi_{k+-}(n,A) \left(e^\dagger_{kA} + e^\dagger_{kB}\right)(e_{kA} - e_{kB}) + \frac{1}{2} \xi_{k-+}(n,A) \left(e^\dagger_{kA} - e^\dagger_{kB}\right)(e_{kA} + e_{kB}) \\
&+ \frac{1}{2} \xi_{k--}(n,A) \left(e^\dagger_{kA} - e^\dagger_{kB}\right)(e_{kA} - e_{kB}) \Big\} \\
= &- t' \sum_n \sum_k \sin\left(\frac{k}{2}\right) \Big\{ \left(\xi_{k++} + \xi_{k+-} + \xi_{k-+} + \xi_{k--}\right)(n,A)\, e^\dagger_{kA} e_{kA} \\
&+ \left(\xi_{k++} - \xi_{k+-} + \xi_{k-+} - \xi_{k--}\right)(n,A)\, e^\dagger_{kA} e_{kB} \\
&+ \left(\xi_{k++} + \xi_{k+-} - \xi_{k-+} - \xi_{k--}\right)(n,A)\, e^\dagger_{kB} e_{kA} \\
&+ \left(\xi_{k++} - \xi_{k+-} - \xi_{k-+} + \xi_{k--}\right)(n,A)\, e^\dagger_{kB} e_{kB} \Big\}
\end{aligned}
$$

A closer look at the symmetry of the ξs gives:

$$
\begin{aligned}
\sum_n \xi_{k,\nu\mu}(n,S) &= \sum_n \phi^*_{k\nu}(n,S)\, \phi_{k\mu}(n-1,S) + \phi^*_{k\nu}(n,S)\, \phi_{k\mu}(n+1,S) \\
&= \sum_m \phi^*_{k\nu}(m+1,S)\, \phi_{k\mu}(m,S) + \sum_r \phi^*_{k\nu}(r-1,S)\, \phi_{k\mu}(r,S) \\
&= \sum_n \phi_{k\mu}(n,S)\, \phi^*_{k\nu}(n+1,S) + \phi_{k\mu}(n,S)\, \phi^*_{k\nu}(n-1,S) \\
&= \sum_n \xi^*_{k,\nu\mu}(n,S)
\end{aligned}
$$

Since for both sublattices $S = A, B$ the eigenstates of the free Hamiltonian are real (due to the shift in k), the band indices can be switched without changing the value, and one has $\sum_n \xi_{k,+-}(n,S) = \sum_n \xi_{k,-+}(n,S)$

Moreover, the eigenstates themselves have a certain symmetry:

$$
\begin{aligned}
\frac{1}{2}\left(\vec{\phi}_{k+} + \vec{\phi}_{k-}\right) = \vec{\phi}_A \quad &\Leftrightarrow \quad \phi_{k+}(n,B) = -\phi_{k-}(n,B) \quad \forall n \\
\frac{1}{2}\left(\vec{\phi}_{k+} - \vec{\phi}_{k-}\right) = \vec{\phi}_B \quad &\Leftrightarrow \quad \phi_{k+}(n,A) = \phi_{k-}(n,A) \quad \forall n
\end{aligned}
$$

And with this we get for both sublattices: $\sum_n \xi_{k,++}(n,S) = \sum_n \xi_{k,--}(n,S)$
Inserting these two properties, we get for the second addend on sublattice A:

$$... = -t' \sum_n \sum_k \sin\left(\frac{k}{2}\right) \left\{ 2\left[\xi_{k++} + \xi_{k+-}\right](n,A) \cdot e^\dagger_{kA} e_{kA} + 2\left[\xi_{k,++} - \xi_{k+-}\right](n,A) \cdot e^\dagger_{kB} e_{kB} \right\}$$

A.2. Closed expression for the Ewald summation

Following Fukui and Todo[62], we can rewrite the Ewald summation to

$$\begin{aligned}
\sin\left(\frac{\pi j}{L}\right) &= \left(\frac{\pi j}{L}\right)\left(1-\frac{j}{L}\right)\left(1+\frac{j}{L}\right)\left(\frac{2-j/L}{2}\right)\left(\frac{2+j/L}{2}\right)\left(\frac{3-j/L}{3}\right)\left(\frac{3+j/L}{3}\right)\cdot ... \\
\ln\left(\sin\left(\frac{\pi j}{L}\right)\right) &= \ln\left(\frac{\pi j}{L}\right) + \ln(L-j) - \ln(L) + \ln(L+j) - \ln(L) + \ln(2L-j) - \ln(L) + ... \\
\frac{d^2}{dj^2}\ln\left(\sin\left(\frac{\pi j}{L}\right)\right) &= \frac{d}{dj}\left\{\frac{L}{\pi j}\frac{\pi}{L} - \frac{1}{L-j} + \frac{1}{L+j} - \frac{1}{2L-j} + \frac{1}{2L+j} - \frac{1}{3L-j} + \frac{1}{3L+j} + ...\right\} \\
\frac{d}{dj}\frac{\cos\left(\frac{\pi j}{L}\right)}{\sin\left(\frac{\pi j}{L}\right)}\frac{\pi}{L} &= \frac{d}{dj}\left\{\frac{1}{j} + \frac{1}{j-L} + \frac{1}{j+L} + \frac{1}{j-2L} + \frac{1}{j+2L} + \frac{1}{j-3L} + \frac{1}{j+3L} + ...\right\} \\
&\\
&\frac{\pi}{L}\left(\frac{-\sin\left(\frac{\pi j}{L}\right)\frac{\pi}{L}}{\sin\left(\frac{\pi j}{L}\right)} - \frac{\cos\left(\frac{\pi j}{L}\right)}{\sin^2\left(\frac{\pi j}{L}\right)}\cos\left(\frac{\pi j}{L}\right)\frac{\pi}{L}\right) \\
&= -\frac{1}{j^2} - \frac{1}{(j-L)^2} - \frac{1}{(j+L)^2} - \frac{1}{(j-2L)^2} - \frac{1}{(j+2L)^2} - \frac{1}{(j-3L)^2} - \frac{1}{(j+3L)^2} + ... \\
\frac{\pi^2}{L^2}\frac{-\sin^2\left(\frac{\pi j}{L}\right) - \cos^2\left(\frac{\pi j}{L}\right)}{\sin^2\left(\frac{\pi j}{L}\right)} &= -\sum_{n=-\infty}^{\infty}\frac{1}{(j-nL)^2} \\
\frac{\pi^2}{L^2}\frac{1}{\sin^2\left(\frac{\pi j}{L}\right)} &= \sum_{n=-\infty}^{\infty}\frac{1}{(j-nL)^2}
\end{aligned} \tag{A.1}$$

The derivation is largely inspired by a proof Euler gave for the so called Basel problem[102]

$$\sum_{n=1}^{\infty}\frac{1}{n^2} = \frac{\pi^2}{6}$$

A.3. Two-step fitting procedure for the critical exponents

In the first part, we determine the presumed collapse plot for different values of J_{AF}^{crit} in the critical area with steps of 10^{-5} and $\frac{1}{\nu}$ with steps of 10^{-3}. For each combination of values in the grid a fit is carried out, fitting a third-order polynomial function to the set containing the appropriately scaled values of all lengths $L \in \{2000, 4000, 6000, 8000, 10000\}$. Now the χ^2/ndof of this fit is analyzed, and we assume that the best fit is the one with the smallest error and also corresponds to the best choice of parameters to make the plots collapse. In Fig. A.1 one can see a contour plot of $\ln\left(\chi^2/\mathrm{ndof}\right)$ as a function of J_{AF}^{crit} and $1/\nu$. It is visible that the minimal

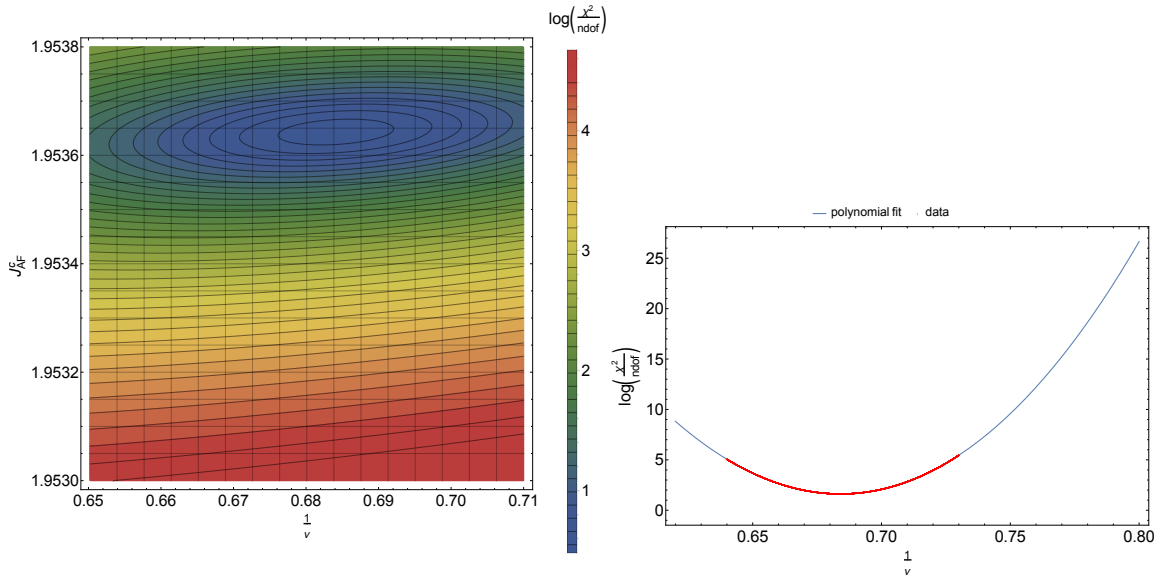

Figure A.1.: Left side: The contour plot shows $\ln\left(\frac{\chi^2}{\text{ndof}}\right)$ from a fit of a polynomial function to the collapsed finite-size plots of the leg susceptibilities. Right side: In the second step, the values along the line with minimal $\frac{\chi^2}{\text{ndof}}$ are fitted against another third-degree polynomial.

values can be found roughly along a diagonal line, so it seems best to sample along this line in a second step. We look for the minimal values at constant J^c_{AF} and apply a linear extrapolation.

In the second part, the χ^2/ndof of the fit along this one-dimensional parameter set is again sampled with a better accuracy, namely $\Delta\frac{1}{\nu} = 10^{-5}$. Then the one-dimensional function of χ^2/ndof-values undergoes a second fit to another third degree polynomial function to find its minimum. From the fit parameters, the ideal choice for $\frac{1}{\nu}$ is calculated, and the corresponding J^c_{AF} determined. Finally, we carry out a bootstrap analysis of the procedure with $N = 100$ steps to get an estimate for the error on both values. For this, we take into account again a somewhat coarser grid around the presumed minimum, and for each randomly chosen set of values we determine the critical parameters that give the minimal χ^2/ndof. Figure A.2 presents the histograms of both distribution; they are sufficiently close to a normla distribution.

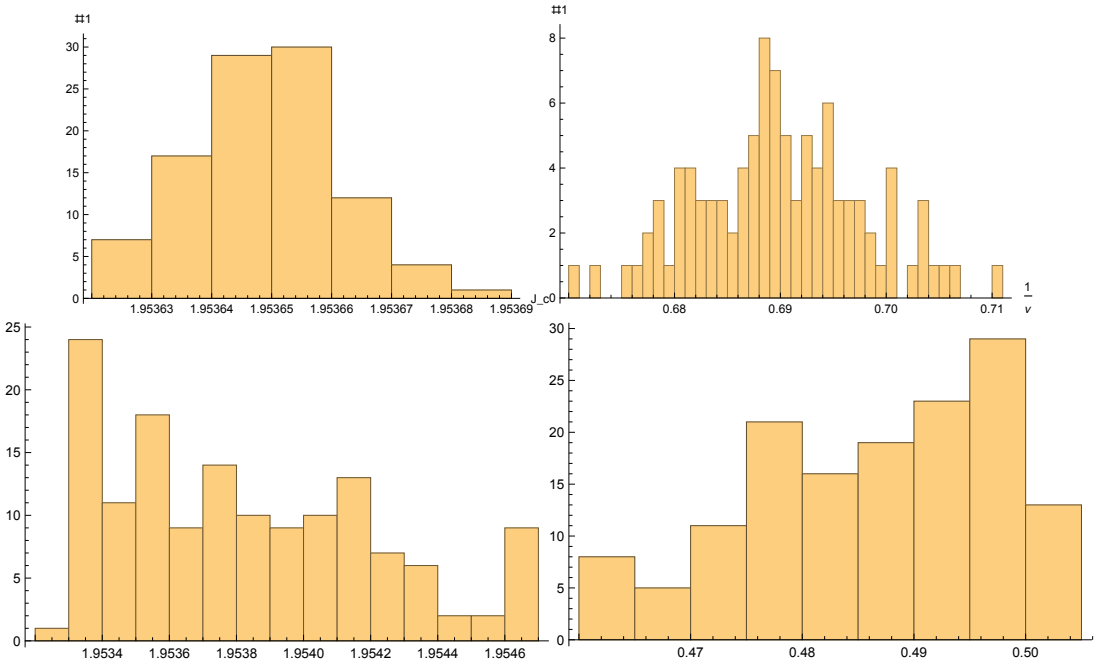

Figure A.2.: Top: The values of a bootstrap analysis of the susceptibility collaps plots for $J_{\text{crit}}^{\text{AF}}$ and $\frac{1}{\nu}$ give a normal distribution in the limit $N \to \infty$. We have chosen $N = 100$. Bottom: The values of the bootstrap analysis follow a skewed distribution for the spin structure factor along one leg, with $N = 150$.

Bibliography

[1] K. Novoselov, A. Geim, S. Morozov, D. Jiang, Y. Zhang, S. Dubonos, I. Grigorieva, and A. Firsov, Science **306**, 666 (2004).

[2] K. Novoselov, D. Jiang, F. Schedin, T. Booth, V. Khotkevich, S. Morozov, and A. Geim, PNAS **102**, 10451 (2005).

[3] P. Wallace, Physical Review **71**, 622 (1947).

[4] E. Fradkin, Phys. Rev. B **33**, 3263 (1986).

[5] F. Haldane, Phys. Rev. Lett. **61**, 2015 (1988).

[6] M. Fujita, K. Wakabayashi, K. Nakada, and K. Kusakabe, J. Phys. Soc. Jpn. **65**, 1920 (1996).

[7] K. Nakada, M. Fujita, G. Dresselhaus, and M. S. Dresselhaus, Phys. Rev. B **54**, 17954 (1996).

[8] K. Wakabayashi, M. Sigrist, and M. Fujita, J. Phys. Soc. Jpn. **67**, 2089 (1998).

[9] A. C. Neto, F. Guinea, N. Peres, K. Novoselov, and A. Geim, Rev. Mod. Phys. **81**, 109 (2009).

[10] A. Geim and K. Novoselov, Nat. Mater. **6**, 183 (2007).

[11] C. Tao *et al.*, Nat. Phys. **7**, 616 (2011).

[12] H. Feldner, Z. Y. Meng, T. C. Lang, F. F. Assaad, S. Wessel, and A. Honecker, Phys. Rev. Lett. **106**, 226401 (2011).

[13] Y.-W. Son, M. L. Cohen, and S. G. Louie, nature Letters **444**, 347 (2006).

[14] O. V. Yazyev and M. Katsnelson, Phys. Rev. Lett. **100**, 047209 (2008).

[15] W. Hei, R. W. Kawakami, M. Gmitra, and J. Fabian, nature nanotechnology **9**, 794 (2014).

[16] O. V. Yazyev, Rep. Prog. Phys. **73**, 056501 (2010).

[17] G. Burkard, H.-A. Engel, and D. Loss, arXiv: cond-mat/0004182v2 (2000).

[18] G. Burkard, Physik Journal **13**, 35 (2014).

[19] M. Golor, C. Koop, T. C. Lang, S. Wessel, and M. J. Schmidt, Phys. Rev. Lett. **111**, 085504 (2013).

[20] N. D. Mermin and H. Wagner, Phys. Rev. Lett. **17**, 1133 (1966).

[21] P. Cui *et al.*, Phys. Rev. Lett. **116** (2016).

[22] M. Wimmer, İ. Adagideli, S. Berber, D. Tománek, and K. Richter, Phys. Rev. Lett. **100**, 177207 (2008).

[23] X.-D. Tan, C. Koop, X.-P. Liao, and L. Sun, J. Phys.: Condens. Matter **28**, 435601 (2016).

[24] G. Z. Magda *et al.*, nature Letter **514**, 608 (2014).

[25] T. Makarova *et al.*, Sci. Rep. 5 **5**, 13382 (2015).

[26] P. Ruffieux *et al.*, nature Letter **531**, 489 (2016).

[27] H. Lee, Y.-W. Son, N.-J. Park, S. Han, and J. Yo, Phys. Rev. B **73**, 174431 (2005).

[28] W. Zhang, F. Hajiheidari, Y. Li, and R. Mazzarello, Nat. Sci. Rep. **6**, 29009 (2016).

[29] R. Drost, A. Uppstu, F. Schulz, S. K. Hämäläinen, M. Ervasti, A. Harju, and P. Liljeroth, Nano Lett. **14**, 1528 (2014).

[30] M. J. Schmidt and D. Loss, Phys. Rev. B **82**, 085422 (2010).

[31] M. J. Schmidt, M. Golor, T. C. Lang, and S. Wessel, Phys. Rev. B **87**, 245431 (2013).

[32] H. Karimi and I. Affleck, Phys. Rev. B **86**, 115446 (2012).

[33] A. W. Sandvik, Journal of Physics A: Mathematical and General **25**, 3667 (1992).

[34] A. W. Sandvik and J. Kurkijärvi, Phys. Rev. B **43**, 5950 (1991).

[35] F. Haldane, Phys. Rev. Lett. **60**, 635 (1988).

[36] B. S. Shastry, Phys. Rev. Lett. **60**, 639 (1988).

[37] F. Haldane, Phys. Rev. Lett. **66**, 1529 (1991).

[38] C. Koop and M. J. Schmidt, Phys. Rev. B **92**, 125416 (2015).

[39] A. C. Koop, *Correlations at Graphene Edges*, Master's thesis, Institute for Theoretical Solid State Physics, RWTH Aachen (2013).

[40] D. J. Luitz, F. F. Assaad, and M. J. Schmidt, Phys. Rev. B **83**, 195432 (2011).

[41] M. Ruderman and C. Kittel, Physical Review **96** (1954).

[42] T. Kasuya, Prog. Theor. Phys **16**, 45 (1956).

[43] K. Yosida, Physical Review **106**, 893 (1957).

[44] M. Sherafati and S. Satpathy, Phys. Rev. B **83**, 165425 (2011).

[45] S. Saremi, Phys. Rev. B **76**, 184430 (2007).

[46] G. Yang, S. Xu, W. Zhang, T. Ma, and C. Wu, Phys. Rev. B **94**, 075106 (2016).

[47] A. Rudenko, S. Yuan, and M. Katsnelson, Phys. Rev. B **92**, 085419 (2015).

[48] A. Rudenko and M. Katsnelson, Phys. Rev. B **89**, 201408 (2014).

[49] H. O. Churchill and P. Jarillo-Herrero, nature nanotechnology, news and views , 370 (2014).

[50] L. Li, Y. Yu, G. J. Ye, Q. Ge, X. Ou, H. Wu, D. Feng, X. H. Chen, and Y. Zhang, nature nanotechnology , 372 (2014).

[51] J. Viana-Gomes, V. M. Pereira, and N. Peres, Phys. Rev. B **80**, 245436 (2009).

[52] A. Castellanos-Gomez, L. Vicarelli, E. Prada, J. O. Island, K. Narasimha-Acharya, S. I. Blanter, D. J. Groenendijk, M. Buscema, G. A. Steele, J. Alvarez, H. W. Zandbergen, J. Palacios, and H. S. van der Zant, 2D Materials (2014).

[53] S. Wessel, "Lecture notes in computational physics," (2012).

[54] R. G. Melko, "Stochastic series expansion quantum Monte Carlo," in *Strongly Correlated Systems: Numerical Methods*, edited by A. Avella and F. Mancini (Springer, Berlin, Heidelberg, 2013) pp. 185–206.

[55] S. Wessel, in *Emergent Phenomena on Correlated Matter*, Schriften des Forschungszentrums Jülich, Reihe Modeling and Simulation, edited by E. Pavarini, E. Koch, and U. Schollwöck (Forschungszentrum Jülich GmbH, Institute for Advanced Simulation, German Research School for Simulation Sciences GmbH, 2013).

[56] M. Suzuki, Prog. Theor. Phys **56**, 1454 (1976).

[57] H. Trotter, Proc. Amer. Math. Soc. **10**, 545 (1959).

[58] A. Sandvik, AIP Conf. Proc. **135**, 135 (2010).

[59] M. Troyer, H. Tsunetsugu, and D. Würtz, Phys. Rev. B **50**, 13515 (1994).

[60] A. W. Sandvik, Phys. Rev. E **68**, 056701 (2003).

[61] S. Todo and H. Suwa, arXiv:1310.6615v1 (2013).

[62] K. Fukui and S. Todo, Journal of Computational Physics **220**, 2629 (2009).

[63] A. Dorneich and M. Troyer, Phys. Rev. E **64** (2001).

[64] H. Evertz, Adv. Phys. **52**, 1 (2003).

[65] A. Sandvik, J. Phys. A: Math.Gen **25**, 3667 (1992).

[66] M. Newman and G. Barkema, *Monte Carlo Methods in Statstical Physics* (Clarendon Press, Oxford University Press, 1999).

[67] A. I. McIntosh, arXiv: 1606.00497v1 (2016).

[68] M. Greven, R. J. Birgeneau, and U.-J. Wiese, Phys. Rev. Lett. **77**, 1865 (1996).

[69] M. Roji and S. Miyashita, J. Phys. Soc. Jpn. **65**, 883 (1996).

[70] A. Fledderjohann, *Ground state properties of antiferromagnetic spin-1/2 Heisenberg systems in external fields*, habilitation, Bergische Universität Wuppertal (2014).

[71] F. Haldane, Phys. Rev. Lett. **50**, 1153 (1983).

[72] T. Vekua, G. Japardize, and H.-J. Mikeska, Phys. Rev. B **67**, 064419 (2003).

[73] A. W. Sandvik, arXiv: 1101.3281v1 (2011).

[74] S. Larochelle and M. Greven, Phys. Rev. B **69**, 092408 (2004).

[75] A. Kolezhuk and H.-J. Mikeska, Phys. Rev. B **53**, R8848 (1996).

[76] C. Koop and S. Wessel, Phys. Rev. B **96**, 165114 (2017).

[77] L. Wang, Y.-H. Liu, J. Imriška, P. N. Ma, and M. Troyer, Phys. Rev. X **5**, 031007 (2015).

[78] O. Vassiliev, I. Rojdestvenski, and M. Cottam, Physica A **294**, 139 (2001).

[79] K. Fukui and S. Todo, Jour. Comp. Phys. **228**, 2629 (2009).

[80] S. Wessel, "Lecture notes in advanced statistical physics," (2015).

[81] S. Sachdev and B. Keimer, Physics Today **64**, 29 (2011).

[82] S. Sachdev, *Quantum Phase Transitions* (Cambridge University Press, 2011).

[83] R. Coldea *et al.*, Science **327**, 177 (2010).

[84] R. A. Römer and B. Sutherland, arXiv **9303004v1** (1993).

[85] H. Nakano and M. Takahashi, Phys. Rev. B **50**, 10331 (1994).

[86] H. Nakano and M. Takahashi, J. Phys. Soc. Jpn. **63**, 926 (1994).

[87] A. Dutta and J. Bhattacharjee, Phys. Rev. B **64**, 184106 (2001).

[88] *Introduction to Monte Carlo Methods* (Third international summer school "Computational Science", Oldenburg, arXiv0905.1602.v3, 2011).

[89] J. L. Cardy, in *Finite-Size scaling*, Current Physics- Sources and Comments, edited by J. L. Cardy (North-Holland, Elsevier Science Publishing Company Inc., 1988) Chap. 1, pp. 1–7.

[90] M. F. Maghrebi, Z.-X. Gong, M. Foss-Feig, and A. V. Gorshkov, Phys. Rev. B **93**, 125128 (2016).

[91] A. Dutta, Phys. Rev. B **65**, 224427 (2002).

[92] N. Defenu, A. Trombettoni, and S. Ruffo, arXiv 1704.00528v1 (2017).

[93] H. Kleinert and V. Schulte-Frohlinde, *Critical Properties of ϕ^4-Theories* (Freie Universität Berlin, 2001).

[94] M. Vojta, "Thermal and quantum phase transitions," (2015).

[95] S. Pankov, S. Florens, A. Georges, G. Kotliar, and S. Sachdev, Phys. Rev. B **69**, 054426 (2004).

[96] J. Um and S.-I. Lee, Jour. of the Korean Phys. Soc. **50**, 285 (2007).

[97] S. Hesselmann and S. Wessel, Phys. Rev. B **93**, 155157 (2016).

[98] Z. Shi and I. Affleck, Phys. Rev. B **95**, 195420 (2017).

[99] M. Golor, T. C. Lang, and S. Wessel, Phys. Rev. B **87**, 155441 (2013).

[100] M. Golor, S. Wessel, and M. J. Schmidt, Phys. Rev. Lett. **112**, 046601 (2014).

[101] M. P. Zaletel, R. S. Mong, C. Karrasch, J. E. Moore, and F. Pollmann, Phys. Rev. B **91**, 165112 (2015).

[102] B. B. Sullivan, "The Basel Problem: Numerous Proofs," (2013).